UNIVERSITY OF CALIFORNIA, SAN DIEGO

Dynamic modeling and analysis of gyroscopic multibody systems and flexible robots

A dissertation submitted in partial satisfaction of the
requirements for the degree Doctor of Philosophy

in

Engineering Sciences (Mechanical Engineering)

by

Oscar Rios

Committee in charge:

Professor Hidenori Murakami, Chair
Professor Matthew H. Alford
Professor Gilberto Mosqueda
Professor Eugene R. Pawlak
Professor Michael T. Tolley

2017

The dissertation of Oscar Rios is approved, and is acceptable in quality and form for publication on microfilm and electronically:

_____

_____

_____

_____

_____

Chair

University of California, San Diego

2017

TABLE OF CONTENTS

LIST OF FIGURES

LIST OF TABLES

ACKNOWLEDGEMENTS

I first and foremost would like to thank my advisor, Professor Hidenori Murakami. Since the first day I walked in to his office as an undergraduate student, he has taken me under his wing. Without his mentoring and guidance, none of this would have been possible. Thank you for taking a chance on me and for all the great years of research. I would also like to thank my committee members, Matthew H. Alford, Gilberto Mosqueda, Eugene R. Pawlak, and Michael T. Tolley for their suggestions and advice on the projects. Furthermore, I would like to thank Thomas J. Impelluso for his support and help all the way from Bergen, Norway.

I would further like to thank the other members of the lab, Ardavan Amini and Takeyuki Ono. The help they provided throughout my years in graduate school was vital for the completion of this dissertation. Thank you guys for not only being great lab mates, but also great friends.

Lastly, I would like to thank my family, especially my parents, Rutilio and Enedelia, my sister Melissa, and my girlfriend Aditi for their support throughout my education. You have all been the greatest source of motivation and inspiration. Thank you for everything.

Chapter 2, in part, is published as "A Theoretical and Numerical Study of the Dzhanibekov and Tennis Racket Phenomena." Journal of Applied Mechanics. This work was coauthored by H. Murakami, and T.J. Impelluso. The dissertation author is the second author of this work.

Chapter 2, in part, is published as "A Theoretical and Numerical Study of the Dzhanibekov and Tennis Racket Phenomena." Proceedings of the ASME 2015

International Mechanical Engineering Congress & Exposition. Paper: IMECE2015-52374. ASME, New York. This work was coauthored by H. Murakami, T. Ono, and T.J. Impelluso. The dissertation author is the second author of this work.

Chapter 3, in part, is published as "A Mathematical Model for a Gyroscopic Ocean-Wave Energy Converter." Proceedings of the ASME 2013 International Mechanical Engineering Congress & Exposition. Paper: IMECE2013-62834. ASME, New York. This work was coauthored by H. Murakami. The dissertation author is the second author of this work.

Chapter 3, in part, is published as "A Mathematical Model with Preliminary Experiments of a Gyroscopic Ocean Wave Energy Converter." Proceedings of the ASME 2015 International Mechanical Engineering Congress & Exposition. Paper: IMECE2015-51163. ASME, New York. This work was coauthored by H. Murakami, and A. Amini. The dissertation author is the second author of this work.

Chapter 3, in part, is published as "A Mathematical Model of an Active Gyroscopic Roll Stabilizer Using the Moving Frame Method." Proceedings of the ASME 2015 International Mechanical Engineering Congress & Exposition. Paper: IMECE2015-51157. ASME, New York. This work was coauthored by H. Murakami. The dissertation author is the first author of this work.

Chapter 4, in part, is published as "Development of Active Mechanical Models for Flexible Robots to Duplicate the Motion of Inch Worms and Snakes." Proceedings of the ASME 2016 International Mechanical Engineering Congress & Exposition. Paper: IMECE2016-65550. ASME, New York. This work was coauthored by H. Murakami, and T. Ono. The dissertation author is the first author of this work.

VITA

2017 Ph.D. Mechanical Engineering

University of California, San Diego, La Jolla, CA

Dissertation: Dynamic modeling and analysis of gyroscopic multibody systems and flexible robots

Advisor: Professor Hidenori Murakami

2014 M.S. Mechanical Engineering

University of California, San Diego, La Jolla, CA

2012 B.S. Mechanical Engineering

University of California, San Diego, La Jolla, CA

PUBLICATIONS

Murakami H. & Rios O. 2013. "A Mathematical Model for a Gyroscopic Ocean-Wave Energy Converter." Proceedings of the ASME 2013 International Mechanical Engineering Congress & Exposition. Paper: IMECE2013-62834. ASME, New York.

Murakami H., Rios O., Amini A. 2015. "A Mathematical Model with Preliminary Experiments of a Gyroscopic Ocean Wave Energy Converter." Proceedings of the ASME 2015 International Mechanical Engineering Congress & Exposition. Paper: IMECE2015-51163. ASME, New York.

Rios O. & Murakami H. 2015. "A Mathematical Model of an Active Gyroscopic Roll Stabilizer Using the Moving Frame Method." Proceedings of the ASME 2015 International Mechanical Engineering Congress & Exposition. Paper: IMECE2015-51157. ASME, New York.

Murakami H., Rios O. & Impelluso T.J. 2015. "A Theoretical and Numerical Study of the Dzhanibekov and Tennis Racket Phenomena." Proceedings of the ASME 2015 International Mechanical Engineering Congress & Exposition. Paper: IMECE2015-52374. ASME, New York.

Murakami H., Rios O. & Impelluso, T.J. 2016. "A Theoretical and Numerical Study of the Dzhanibekov and Tennis Racket Phenomena." Journal of Applied Mechanics.

Rios O., Ono T., Murakami H., Impelluso T.J. 2016. "An Analytical and Geometrical Study of the Dzhanibekov and Tennis Racket Phenomena." Proceedings of the ASME 2016 International Mechanical Engineering Congress & Exposition. Paper: IMECE2016-65570. ASME, New York.

Rios O., Ono T. & Murakami H. 2016. "Development of Active Mechanical Models for Flexible Robots to Duplicate the Motion of Inch Worms and Snakes." Proceedings of the ASME 2016 International Mechanical Engineering Congress & Exposition. Paper: IMECE2016-65550. ASME, New York.

Rios, O., Murakami, H., Amini, A., 2016, "A Mathematical Model of a Gyroscopic Ocean Wave Energy Converter (GOWEC)," *Journal of Energy Resources Technology*. Submitted.

Rios, O., Ono, T., Murakami, H., 2017 "Development of Active Mechanical Models for Flexible and Soft Robots," *Journal of Computational and Nonlinear Dynamics.* Submitted.

Murakami H., Rios O., Ono T., 2017. "Development of a Nonlinear, C1-Beam Finite-Element Code for Actuator Design of Slender Flexible Robots." Proceedings of the ASME 2017 International Mechanical Engineering Congress & Exposition. Submitted.

Rios O., Murakami H., Amini A. 2017. "Modeling and Experimentation of a Ribbed Caudal Fin for Aquatic Robots." Proceedings of the ASME 2017 International Mechanical Engineering Congress & Exposition. Submitted.

ABSTRACT OF THE DISSERTATION

Dynamic modeling and analysis of gyroscopic multibody systems and flexible robots

by

Oscar Rios

Doctor of Philosophy in Engineering Sciences (Mechanical Engineering)

University of California, San Diego, 2017

Professor Hidenori Murakami, Chair

The dissertation presents dynamic modeling and analysis of single rigid bodies, gyroscopic multi-body systems, and flexible robotics through the use of the moving frame method. Before analyzing the projects at hand, a brief introduction to the moving frame method will be presented. To properly model the gyroscopic systems and flexible robots, it is first necessary to establish the kinematical description of freely rotating bodies. To demonstrate the validity and efficacy of the method, it is applied to solve the mystery of

the Dzhanibekov and tennis racket phenomena. It is known that a rotation about the intermediate principal moment of inertia axis becomes unstable, leading many to incorrectly conclude a violation of the conservation of angular momentum. Using the moving frame method, the torque-free Euler equations are clearly obtained and a complete explanation, including a geometric, analytic, and numerical solution is presented along with 3D animations to demonstrate that the conservation of angular momentum is truly preserved.

As an application of the moving frame method to rigid-multibody systems, analysis of two offshore gyroscopic structures will be performed. First, a gyroscopic ocean wave energy converter (GOWEC) is analyzed. The GOWEC is a fully enclosed ocean wave energy device that converts the rocking or pitching motion induced by the ocean waves into electricity. In this dissertation, the mathematical model of the energy converter is derived and the ideal conditions for maximum power output are identified. Second, as a natural extension of the GOWEC, the application of gyroscopes as a means of stabilization is examined. The active gyroscopic ship stabilizer uses the gyroscopic principles to cancel the rolling motion induced by the ocean waves. Of specific interest is the application of active gyroscopic roll stabilizers in ships to further aid in the safe transport of passengers and transfer of equipment onto platforms and offshore wind farm structures. The main parameters of the gyroscopic stabilizer are characterized and their effect on the ship is analyzed.

Lastly, modeling and analysis of flexible robots with internal actuation is presented. Two mechanical models for flexible or soft robots are derived: (i) a discrete multi-link model consisting of rigid links with elastic torsional springs at actuating joints. and (ii) a

continuous beam model with distributed internal actuation. As an application of the continuous beam model, an inchworm with multiple actuation curvature fields is presented. With the flexible mechanical models, it is possible to know the internal actuation necessary for soft robots to reproduce desired shapes and resulting maneuvers. Furthermore, the nonlinear finite element equations along with active $C^{(1)}$-beam elements are developed and used to create a finite element code

CHAPTER 1: INTRODUCTION

In the field of dynamics, Leonhard Euler extended Isaac Newton's work on particles and applied it to rigid bodies, developing the translational and rotational equations of motion. Of interest in this dissertation is the use of the moving frame method in analyzing rigid and flexible bodies. The moving frame method with differential forms was first pioneered by Elie Joseph Cartan in relativity [1] and then was applied to classical physics by Flanders [2] and Frankel [3]. Hidenori Murakami [4,5] applied it to rigid-body dynamics to ease the kinematic and kinetic computations utilizing the special orthogonal group SO(3) and the special Euclidean group SE(3). The moving frame method with Frankel's compact notation [3] provides an efficient approach to dynamics and will be utilized throughout this dissertation to analyze several projects.

1.1 The Dzhanibekov and Tennis Racket Phenomena

In 1985, Vladimir Dzhanibekov, a Russian astronaut, conducted experiments in the space station concerning the rotation of a rigid body with three distinct principal moment of inertia values. As can be seen in the Dzhanibekov and tennis racket phenomena, rotations about the largest and smallest principal moments of inertia remain stable [6,7]. However, as presented by Dzhanibekov, the rotation of a rigid body (dictionary, wing nut, box) about the principal intermediate moment of inertia causes the initial spin axis to rotate. Similar experiments have been conducted on earth with a tennis racket and table tennis paddle, both of which produced similar results to Dzhanibekov's experiments [6].

The equations governing rotational motion of a rigid body are referred to as Euler's equations, named after Leohnard Euler whom developed rigid body dynamics. As a special

case of interest in this work, he also investigated the torque-free rotation of a rigid body. Both the Dzhanibekov and the tennis racket phenomena can be governed by the torque-free Euler equations. The moving frame method will be used to show a clear derivation of the equations that govern this seemingly non-trivial behavior of the tennis racket and Dzhanibekov experiments and to demonstrate that the conservation of momentum is truly preserved.

This phenomenon happens when there are three distinct principal moments of inertia values. A successful analysis may have applications in the rotation of floating bodies as well as the safe deployment of a satellite's solar panels since the principal axes of the satellite system changes during deployment. Thus, it is important to solve this problem with a complete analysis that consolidates previous contributions.

1.2 Gyroscopic Multibody Systems

The kinematics of multibody systems through the use of the moving frame method begins by attaching a Cartesian coordinate system to each rigid-body. For a system comprised of jointed bodies, as is the case in the projects described in Chapter 3, a graph tree can be obtained that visually shows the progression of how the bodies are connected to one another. The kinematic connection between the jointed rigid bodies is effectively performed by using 4×4 homogeneous transformation matrices which will be defined throughout as relative frame connection matrices. To facilitate the kinematic progression from one rigid body to another, the coordinate vector-basis is explicitly written, as Cartan did when discussing manifolds. The moving frame and its application to multibody systems is demonstrated in this dissertation by analyzing two gyroscopic structures and devices

As a first application, a gyroscopic ocean wave energy converter will be analyzed to further aid the development of renewable energy technology. Global attempts to increase generation of clean and reproducible natural energy have contributed considerable progress in solar, wind, biomass, and geothermal energy generation. To meet the goal set by Renewable Portfolio Standards (RPS) in the U.S., it is advisable to tap into the least explored ocean-wave energy. The advantages of ocean-wave energy generation are twofold. First, the energy per unit area is 20 to 30 times larger compared to solar energy and five to ten times larger compared to wind energy. Second, it is easier to predict waves than wind. Additionally, ocean-wave energy generation meets the challenges of protecting marine resources [6]. From the design point of view, ocean-wave power generators must survive even under large waves due to hurricanes and tsunamis.

There are many existing ocean wave energy converters. Unlike solar or wind energy, ocean wave energy is still in its infancy and does not yet have a standard design that everyone can agree upon. There are various methods and devices used to capture ocean wave energy. Point absorbers, such as *PowerBuoy,* can harness vertical or heaving motion into electricity while attenuators like *Pelamis* use the induced movement of its joints from the incoming waves. Unlike many of the existing converters, the gyroscopic ocean wave energy converter is able to harness the rocking motion of the ocean waves [7,8].

Various inventions have been patented that use the basic gyroscopic principles to harness energy from the ocean. The basic gyroscopic converter consists of a rotor, a gimbal, and a buoy or outer gimbal. As the rotor spins at a high angular velocity and the outer gimbal or buoy is excited by an incoming wave, a gyroscopic moment is created on the inner gimbal, causing it to rotate. This rotation is then transmitted through a gearbox to an

electric generator, creating electricity. However, the theoretical modeling of gyroscopic ocean wave energy converters is still in its infancy compared to other converters [9,10]. The objective of this project is thus to produce a detailed mathematical model of the system. Through the use of the moving frame method, a systematic approach will be developed to obtain the equations of motion that will aid in optimizing the power output.

As a second application, the active gyroscopic roll stabilizer will be analyzed. The rolling and pitching of ships and boats induced by the ocean waves results in undesirable motion. In an effort to increase the stability of the deck/platform and human comfort and safety, various add-on stability systems have been developed. Of interest in the research presented are internal active systems, specifically the active gyroscopic stabilizer. The research presented regarding the gyroscopic roll stabilizer is focused on developing a detailed mathematical analysis of a marine vessel installed with active gyroscopic roll stabilizer(s). Through the use of the moving frame method, a novel approach has been developed to derive a mathematical model and analyze the effect of the system parameters. The moving frame method allows for a systematic derivation, despite the increase in complexity of the system as the number of stabilizers is increased.

Apart from analyzing single and multi-rigid body systems, the moving frame method can be further applied to deformable flexible bodies as summarized in the next section, with hope that it will aid the development of flexible and soft robots

1.3 Flexible Bodies

The development of various methods of actuation and sensors has enabled engineers to construct elastically deformable soft robots. In many of these soft robots, it is desirable to actuate by taking full advantage of the elastic restoring deformation during

locomotion. To aid with the these tasks, engineers can greatly benefit from a mechanical model of an elastically deformable body. In Chapter 4, the mechanical models for slender, flexible robots are developed to quantitatively describe the internal actuation needed to duplicate the target mimicking motions of creatures. Two models are developed and presented: (i) a multi-body model consisting of discrete, jointed cylindrical segments with torsional springs, and (ii) a continuous beam model with internal actuation. Furthermore, active C^1-beam elements are developed within a computational scheme for a nonlinear planar FE code. As an application of the FE code developed, the locomotion of an inchworm is simulated.

1.4 References

[1] Cartan, E., 1986, *On Manifolds with an Affine Connection and the Theory of General Relativity*, translated by A. Magnon and A. Ashtekar, Napoli, Italy, Bibliopolis.

[2] Soechting, J.F. and Flanders, M., 1992. Moving in three-dimensional space: frames of reference, vectors, and coordinate systems. *Annual review of neuroscience*, *15*(1), pp.167-191.

[3] Frankel, T., 2011. *The geometry of physics: an introduction*. Cambridge University Press.

[4] Murakami, H., 2015, "A Moving Frame Method for Multi-Body Dynamics Using SE(3)," *Proceedings of the ASME 2015 International Mechanical Engineering Congress & Exposition*, paper IMECE2015-51192, 19 pages, ASME, New York.

[5] Murakami, H., 2015, "A Moving Frame Method for Multi-Body Dynamics Using SE(3)," *Proceedings of the ASME 2015 International Mechanical Engineering Congress & Exposition*, paper IMECE2015-51192, 19 pages, ASME, New York.

[6] H.T.Harvey & Associates, 2008, *Developing Wave Energy in Coastal California, Potential Socio-Economic and Environmental Effects*, report prepared for California Energy 9 Copyright © 2013 by ASME Commission and California Ocean Protection Council, CEC-500-20008-083.

[7] "Home". 2016. *Ocean Power Technologies*.http://www.oceanpowertechnologies.com/.

[8] "Pelamis, World'S First Commercial Wave Energy Project, Agucadoura". 2016.

[9] Goldin, A., 2004, "*Autonomous Gyroscopic Ocean-Wave Powered Generator: Invention of a New Energy Conversion Technology,"*www.siemensfoundation. org/en/competition/2004-winners/aaron_goldin.htm.

[10] Kanki, H, Arii, S., Fukui, K., and Tsukuo, K., 2007, "Ocean experiment of wave-power generation system by gyro effect," *Proceedings for the 2007 Japan Society of Mechanical Engineers Conference*, Suita, Japan, abstract 0511, 2 pages (in Japanese).

CHAPTER 2: THE DZHANIBEKOV AND TENNIS RACKET PHENOMENA

2.1 Introduction

In the 18th century, Leonhard Euler (1707-1783) developed rigid-body dynamics and to this day the equation of rotational motion of a rigid body is referred to as *Euler's equation*. As a simplification relevant to this paper, he also derived the equations that describe the dynamics of rigid bodies in torque-free motion [1,2].

Both the Dzhanibekov phenomenon and the tennis racket phenomenon occur during torque-free rotation of a rigid-body as formulated by Euler. More specifically, this phenomenon happens when there are three distinct principal moments of inertia. A successful analysis may have applications in the safe deployment of a satellite's solar panels since the principal axes of the satellite system changes during deployment. Thus, it is important to solve this problem with a complete analysis that consolidates previous contributions. First, however, it is necessary to define the Newton and the Euler equations of motion for a single rigid body.

2.1.1 Equations of Motion of a Rigid Body

To locate points within a rigid body of mass *m*, a body-attached principal coordinate system $\{s_1 \quad s_2 \quad s_3\}$ is introduced with its origin at the body's *center of mass*, point C, in Euclidean 3-space, $\mathbb{R}^3$. We define the unit vector $\mathbf{e}_i(t)$ tangent to the s_i -coordinate axis, $i = 1, 2, 3$, and from them form a vector basis $\mathbf{e}(t) \equiv (\mathbf{e}_1(t) \quad \mathbf{e}_2(t) \quad \mathbf{e}_3(t))$.

To define position vectors of the rigid-body, a fixed inertial coordinate system $\{x_1 \quad x_2 \quad x_3\}$ with the origin at point O is also introduced, as shown in Fig. 1. The unit coordinate vector along the x_i-coordinate axis is denoted by $\mathbf{e}_i^{\,I}$. The vector basis for the

inertial coordinate system is defined as: $\mathbf{e}^I \equiv \left(\mathbf{e}_1^{\ I} \quad \mathbf{e}_2^{\ I} \quad \mathbf{e}_3^{\ I}\right)$. For analytical simplicity, we select the inertial coordinate system to be the body-attached coordinate system at time *t*=0: $\mathbf{e}^I = \mathbf{e}(0)$.

Furthermore, with regard to both coordinate systems, and following Refs. [3] and [4], we write the vector basis explicitly to represent vectors. We do this to identify the coordinate system that supports the vector components. To facilitate this, we adopt Frankel's compact notation [5], where the vector basis $\mathbf{e}(t) \equiv \left(\mathbf{e}_1(t) \quad \mathbf{e}_2(t) \quad \mathbf{e}_3(t)\right)$ is expressed by a 1×3 row matrix, and the vector components are expressed by a 3×1 column matrix [6].

Also, the body attached coordinates will be defined so that the mass moment of inertia with the s_i-axis becomes J_{iC} and the inequality $J_{1C} > J_{2C} > J_{3C} > 0$ is satisfied. In addition, we reemphasize that x_i is reserved to designate the inertial coordinate system, while s_i is reserved for the body-attached coordinate system.

2.1.2 Newton's Equation of Motion of the Center of Mass

In Fig. 1, the position vector of the center of mass, C, of the body-attached frame is expressed using the inertial frame as:

$$\mathbf{r}_C(t) = \mathbf{e}^I \; x_C(t) \equiv \left(\mathbf{e}_1^{\ I} \quad \mathbf{e}_2^{\ I} \quad \mathbf{e}_3^{\ I}\right) \begin{pmatrix} x_{1C}(t) \\ x_{2C}(t) \\ x_{3C}(t) \end{pmatrix}. \tag{1}$$

We take the time differentiation, denoted by a superposed dot, of Eq. (1) to obtain the velocity of the center of mass:

$$\mathbf{v}_C(t) = \dot{\mathbf{r}}_C(t) = \mathbf{e}^I \, \dot{x}_C(t) \equiv \begin{pmatrix} \mathbf{e}_1^I & \mathbf{e}_2^I & \mathbf{e}_3^I \end{pmatrix} \begin{pmatrix} \dot{x}_{1C}(t) \\ \dot{x}_{2C}(t) \\ \dot{x}_{3C}(t) \end{pmatrix}. \tag{2}$$

Let the total mass of the body be denoted by *m*. *Newton's equation* of a rigid body subjected to the gravitational force in the $-\mathbf{e}_3^I$ direction is written in vector form as:

$$m\,\dot{\mathbf{v}}_C(t) = -mg\,\mathbf{e}_3^I, \tag{3a}$$

and in components

$$\mathbf{e}^I \, m \begin{pmatrix} \ddot{x}_{1C}(t) \\ \ddot{x}_{2C}(t) \\ \ddot{x}_{3C}(t) \end{pmatrix} = \mathbf{e}^I m \begin{pmatrix} 0 \\ 0 \\ -g \end{pmatrix}. \tag{3b}$$

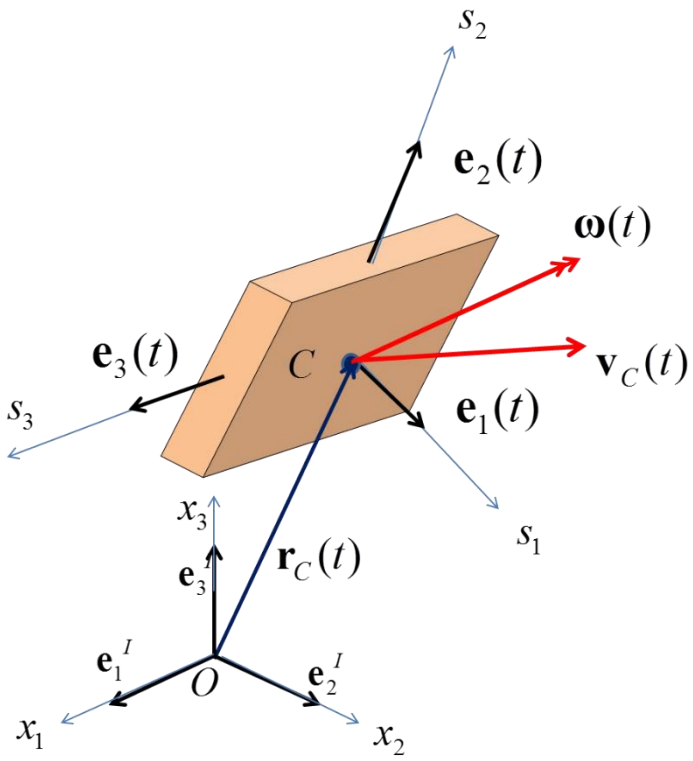

Figure 2-1: A body-attached principal-coordinate system $\{s_1 \quad s_2 \quad s_3\}$ and an inertial coordinate system $\{x_1 \quad x_2 \quad x_3\}$

For the Dzhanibekov experiments in a space station, $g = 0$, while for the tennis racket experiments performed on the ground, g = 9.81m/s^2.

2.1.3 Euler's Equation for Torque Free Motion

The current body-attached vector-basis or frame, $\mathbf{e}(t)$, is obtained from the inertial frame $\mathbf{e}^I = \mathbf{e}(0)$ by rotating it by $R(t)$, a 3×3 rotation matrix with determinant one.

$$\mathbf{e}(t) = \mathbf{e}^I R(t). \tag{4}$$

As with all rotation matrices, which form a Lie group of the special orthogonal group, SO(3), the inverse is the transpose, denoted with the superscript 'T';

$$\mathbf{e}^I = \mathbf{e}(t)\,(R(t))^T. \tag{5}$$

We take the time derivative of Eq. (4) and use Eq. (5) to obtain:

$$\dot{\mathbf{e}}(t) = \mathbf{e}^I \dot{R}(t) = \mathbf{e}(t)\,(R(t))^T \dot{R}(t). \tag{6}$$

Using the definition of the inverse matrix, $(R(t))^T R(t) = I_d$, where I_d is the 3×3 identity matrix, the last matrix product, $(R(t))^T \dot{R}(t)$, is readily shown to be a 3×3 skew symmetric matrix. Observing a one-to-one correspondence between 3×3 skew symmetric matrices and three vector components, we define the skew symmetric *angular velocity matrix* $\overleftrightarrow{\omega(t)}$ [6]:

$$\dot{\mathbf{e}}(t) = \mathbf{e}(t)\,\overleftrightarrow{\omega(t)}, \tag{7a}$$

where

$$\overleftrightarrow{\omega(t)} \equiv (R(t))^T \dot{R}(t) \equiv \begin{bmatrix} 0 & -\omega_3(t) & \omega_2(t) \\ \omega_3(t) & 0 & -\omega_1(t) \\ -\omega_2(t) & \omega_1(t) & 0 \end{bmatrix}. \tag{7b}$$

The corresponding *angular velocity vector* $\boldsymbol{\omega}(t)$ in $\mathbb{R}^3$ becomes

$$\boldsymbol{\omega}(t) = \mathbf{e}(t)\,\omega(t) \equiv \begin{pmatrix} \mathbf{e}_1(t) & \mathbf{e}_2(t) & \mathbf{e}_3(t) \end{pmatrix} \begin{pmatrix} \omega_1(t) \\ \omega_2(t) \\ \omega_3(t) \end{pmatrix}. \tag{8}$$

Equations (7b) and (8) express a one-to-one correspondence between the skew symmetric matrices in the Lie algebra of *SO*(3), denoted by *so*(3), and vectors in $\mathbb{R}^3$.

Let the *angular momentum vector* about the center of mass be denoted by $\mathbf{H}_C(t)$:

$$\mathbf{H}_C(t) = \mathbf{e}(t)\,H_C(t) \equiv \mathbf{e}(t) \begin{pmatrix} H_{1C}(t) \\ H_{2C}(t) \\ H_{3C}(t) \end{pmatrix}. \tag{9a}$$

Its components, $H_C(t)$, with respect to the body attached frame is expressed by the product between the *principal moment of inertia matrix* J_C and the components of the angular velocity vector as:

$$H_C(t) = J_C\,\omega(t) \equiv \begin{bmatrix} J_{1C} & 0 & 0 \\ 0 & J_{2C} & 0 \\ 0 & 0 & J_{3C} \end{bmatrix} \begin{pmatrix} \omega_1(t) \\ \omega_2(t) \\ \omega_3(t) \end{pmatrix}. \tag{9b}$$

Euler's equation of rotational motion of a rigid body without external torque is expressed in vector form as:

$$\dot{\mathbf{H}}_C(t) = \mathbf{0}. \tag{10}$$

Using the pivotal equation of the moving frame method, Eq. (7a), the time derivative of the angular velocity vector is computed as:

$$\dot{\mathbf{H}}_C(t) \equiv \frac{d}{dt}\left(\mathbf{e}(t)\,H_C(t)\right) = \dot{\mathbf{e}}(t)\,H_C(t) + \mathbf{e}(t)\,\dot{H}_C(t) = \mathbf{e}(t)\left\{\dot{H}_C(t) + \overleftrightarrow{\omega(t)}\,H_C(t)\right\}.$$

Thus, Euler's equation with respect to the body attached frame, using Eq. (9b), becomes:

$$\mathbf{e}(t)\left\{\dot{H}_C(t)+\overleftrightarrow{\omega(t)}H_C(t)\right\}=\mathbf{0}, \tag{11a}$$

and using Eq. (9b):

$$\mathbf{e}(t)\left\{J_C\dot{\omega}(t)+\overleftrightarrow{\omega(t)}J_C\omega(t)\right\}=\mathbf{0}. \tag{11b}$$

We note that $\mathbf{e}(t)\overleftrightarrow{\omega(t)}H_C(t)=\boldsymbol{\omega}(t)\times\mathbf{H}_C(t)$, justifying this new notation that avoids the complexity of the cross product. Also, if the moving frame $\mathbf{e}(t)$ is not written explicitly, as Eq. (11a), the term which corresponds to $\mathbf{e}(t)\dot{H}_C(t)$ must be expressed by introducing an objective time-differential operator that works only on the vector components with respect to the body-attached vector basis, $\mathbf{e}(t)$. Representative symbols used for $\mathbf{e}(t)\dot{H}_C(t)$ are $\delta\mathbf{H}_C(t)/\delta t$, $d'\mathbf{H}_C(t)/dt$, and $\left(\dot{\mathbf{H}}_C(t)\right)_{s-cood}$ [7-10].

Returning to Eq. (11a), to find the components expression, we substitute Eqs. (7b) and (9b) into Eq.(11):

$$\begin{pmatrix}\dot{H}_{1C}(t)\\ \dot{H}_{2C}(t)\\ \dot{H}_{3C}(t)\end{pmatrix}+\begin{bmatrix}0 & -\omega_3(t) & \omega_2(t)\\ \omega_3(t) & 0 & -\omega_1(t)\\ -\omega_2(t) & \omega_1(t) & 0\end{bmatrix}\begin{pmatrix}H_{1C}(t)\\ H_{2C}(t)\\ H_{3C}(t)\end{pmatrix}=\begin{pmatrix}0\\0\\0\end{pmatrix}, \tag{12a}$$

$$\begin{bmatrix}J_{1C} & 0 & 0\\ 0 & J_{2C} & 0\\ 0 & 0 & J_{3C}\end{bmatrix}\begin{pmatrix}\dot{\omega}_1(t)\\ \dot{\omega}_2(t)\\ \dot{\omega}_3(t)\end{pmatrix}+\begin{bmatrix}0 & -\omega_3(t) & \omega_2(t)\\ \omega_3(t) & 0 & -\omega_1(t)\\ -\omega_2(t) & \omega_1(t) & 0\end{bmatrix}\begin{bmatrix}J_{1C} & 0 & 0\\ 0 & J_{2C} & 0\\ 0 & 0 & J_{3C}\end{bmatrix}\begin{pmatrix}\omega_1(t)\\ \omega_2(t)\\ \omega_3(t)\end{pmatrix}=\begin{pmatrix}0\\0\\0\end{pmatrix}. \tag{12b}$$

Equation (12b) yields Euler's equation for a torque free motion:

$$\mathbf{e}_1(t):\quad J_{1C}\dot{\omega}_1(t)-(J_{2C}-J_{3C})\omega_2(t)\,\omega_3(t)=0, \tag{13a}$$

$$\mathbf{e}_2(t):\quad J_{2C}\dot{\omega}_2(t)-(J_{3C}-J_{1C})\omega_3(t)\,\omega_1(t)=0, \tag{13b}$$

$$\mathbf{e}_3(t): \quad J_{3C}\dot{\omega}_3(t) - (J_{1C} - J_{2C})\omega_1(t)\,\omega_2(t) = 0\,. \tag{13c}$$

The rotational motion of a body in the Dzhanibekov and the tennis racket phenomena are described by Eqs. (13a-c). We now present available analytical and geometrical analyses of the equations that are relevant to the physical interpretation of the phenomena.

2.1.4 Euler's Analytical Solution of Torque-Free Rotations

In 1765, Euler [1,2] postulated and confirmed that four quantities concerning a body's motion are conserved: the kinetic energy and the three components of angular momentum vector expressed with respect to a fixed inertial coordinate system. We now derive these conserved quantities from Eq. (10) and (11). We begin with kinetic energy.

Let the rotational kinetic energy be defined by K_{rot}:

$$K_{rot}(t) = \frac{1}{2}\boldsymbol{\omega}(t)\cdot\mathbf{H}_C(t) = \frac{1}{2}(\omega(t))^T\left(J_C\omega(t)\right). \tag{14a}$$

We take the time derivative of Eq. (14) using $J_C = (J_C)^T$:

$$\dot{K}_{rot}(t) = \frac{1}{2}\left\{(\dot{\omega}(t))^T\,(J_C)^T\,\omega(t) + (\omega(t))^T\,J_C\dot{\omega}(t)\right\} = (\omega(t))^T\left(J_C\dot{\omega}(t)\right).$$

Then we apply Eq. (11b) in situations without external torque to obtain

$$\dot{K}_{rot}(t) = -(\omega(t))^T\,\overleftrightarrow{\omega(t)}J_C\omega(t)\,. \tag{14b}$$

Finally, we obtain the *conservation of the rotational energy*:

$$\dot{K}_{rot}(t) = 0\,, \tag{15}$$

by noting the vanishing right-hand side. We note this either by performing the multiplications of the right hand side of Eq. (14b) or observing the equivalency of the right-hand-side to the scalar triple product: $-\boldsymbol{\omega}(t)\cdot\{\boldsymbol{\omega}(t)\times\mathbf{H}_C(t)\}$.

We combine Eqs. (14) and (15) using the initial rotational kinetic energy, $K_{rot}(0)$, to express the conservation of rotational kinetic energy. The resulting equation then expresses an ellipsoid with respect to the ω_1, ω_2, ω_3 -axes:

$$J_{1C}(\omega_1(t))^2 + J_{2C}(\omega_2(t))^2 + J_{3C}(\omega_3(t))^2 = 2K_{rot}(0)\,, \tag{16a}$$

and an ellipsoid with respect to the H_{1C}, H_{2C}, H_{3C}-axes [11]:

$$(H_{1C}(t))^2 / J_{1C} + (H_{2C}(t))^2 / J_{2C} + (H_{3C}(t))^2 / J_{3C} = 2K_{rot}(0)\,. \tag{16b}$$

Both ellipsoids are referred to as *energy ellipsoids* or *inertia ellipsoids*.

Euler's second set of conserved quantities—the components of angular momentum with an inertial coordinate frame—are found from Eq. (10)

$$\mathbf{H}_C(t) = \mathbf{H}_C(0)\,. \tag{17}$$

We express Eq. (17) with the inertial coordinate frame as:

$$\mathbf{H}_C(t) = \mathbf{e}^I H_C^{\ I}(t) = \mathbf{e}^I H_C^{\ I}(0)\,. \tag{18}$$

The following issue is of significance with regard to the phenomena under study. When the body rotates, $\dot{\mathbf{e}}(t) \neq \mathbf{0}$, the conservation of angular momentum, Eq. (17), does not enforce that the components of the angular momentum vector decomposed with the body-attached moving frame $\mathbf{e}(t)$ remain constant. They can change according to Eq. (12a), while still satisfying Eqs. (10) and (17).

Euler also noted that the magnitude or norm $\|\mathbf{H}_C(t)\|$ of the angular momentum vector remains the magnitude at $t = 0$ from Eqs. (10) or (17),:

$$(J_{1C}\omega_1(t))^2 + (J_{2C}\omega_2(t))^2 + (J_{3C}\omega_3(t))^2 = \|\mathbf{H}_C(0)\|^2\,. \tag{19a}$$

$$(H_{1C}(t))^2 + (H_{2C}(t))^2 + (H_{3C}(t))^2 = \|\mathbf{H}_C(0)\|^2, \tag{19b}$$

Geometrically, for a constant-length, angular-momentum vector, Eq. (19a) with respect to the ω_1, ω_2, ω_3-axes forms an ellipsoid, while Eq. (19b) with respect to the H_{1C}, H_{2C}, H_{3C}-axes forms a sphere. They are referred to as the *angular momentum ellipsoid* and the *angular momentum sphere*, respectively [15].

Using Eqs. (16a) and (19a), Euler in 1758 [1,2] obtained an analytical solution for $\omega(t)$ of Eqs. (13a-c). His solution was later rewritten by using Jacobi's elliptic functions, which were introduced by Carl Jacobi (1804-1851) in 1829. Wittenburg in 1977 concisely presented Euler's solution using Jacobi's elliptic functions in his monograph [12, 13].

Euler observed from his equations that three steady-state solutions referred to as *permanent rotation states* exist:

$$\omega_1(t) = \hat{\omega}_0, \ \omega_2(t) = \omega_3(t) = 0, \tag{20a}$$

$$\omega_1(t) = 0, \ \omega_2(t) = \hat{\omega}_0, \ \omega_3(t) = 0, \tag{20b}$$

$$\omega_1(t) = \omega_2(t) = 0, \ \omega_3(t) = \hat{\omega}_0, \tag{20c}$$

where $\hat{\omega}_0$ is a constant.

In certain cases, when a dominant angular velocity is applied about one principal axis to induce a state of permanent rotation, the initial angular velocity deviates slightly from the state of permanent rotation. In other words, in addition to the dominant component about the principal axis, the initial angular velocity includes small angular-velocity components about other axes. To account for the slight perturbation of initial conditions, the stability of the angular velocity components near the permanent rotation states must be

examined. We commence this study by first revisiting an existing geometrical interpretation.

2.1.5 Poinsot's Geometrical Presentation of Euler's Solution: Polhodes

Louis Poinsot (1777-1859) added a geometrical interpretation to Euler's analytical solution of a torque-free motion [14]. He postulated that the angular velocity vector must lie on both the constant energy ellipsoid, Eq. (16a), and the constant angular momentum ellipsoid, Eq. (19a). Therefore, the trajectory of the angular velocity vector with respect to the body-attached coordinate frame must lie on a path at the intersections of the two ellipsoids. Each intersection, plotted on the *energy ellipsoid* represents the trajectory of the angular velocity vector, as illustrated in Fig. 2. For a given initial kinetic energy, $K_{rot}(0)$, by changing the magnitude of the initial angular momentum vector, $\|\mathbf{H}_C(0)\|$, *i.e*, the size of the angular momentum ellipsoid, various intersections are obtained. These intersections are collectively referred to as *polhodes* by Poinsot [14].

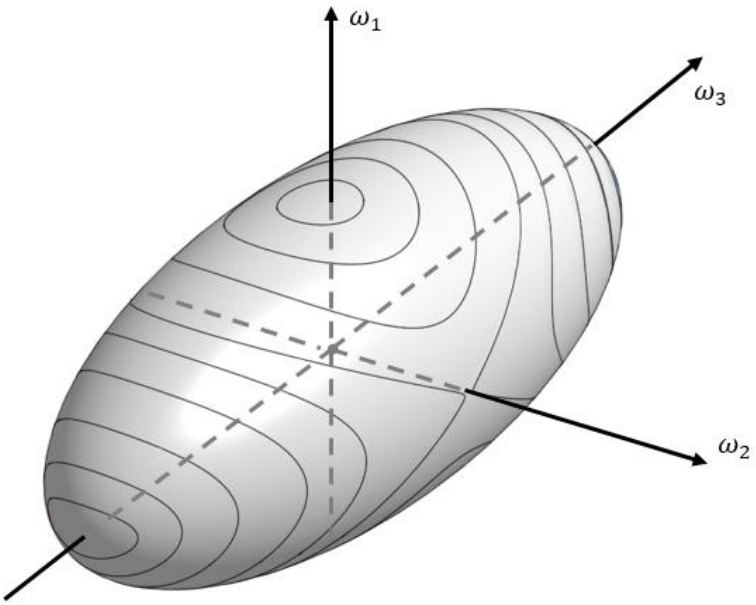

Figure 2-2: Polhodes on a constant rotational energy ellipsoid

Polhodes are closed curves except at the end points of three principal axes of the energy ellipsoid. The end points of the minor axis of the ellipsoid represents the permanent rotation with the s_1-axis, corresponding to the maximum moment inertia, J_1. The end points of the major axis represent the permanent rotation with respect to the s_3-axis, corresponding to the minimum moment of inertia, J_3. These end points of the minor and major axes of the energy ellipse are *centers*, which are surrounded by elliptic trajectories, as shown in Fig. 2. Closed elliptic trajectories of the angular velocity components indicate that the perturbed rotation will not leave the permanent rotation state. The rotational response manifests the permanent rotation state for small perturbations of initial conditions.

In distinction with the previous two cases, the end points of the intermediate axis, corresponding to the permanent rotation about the s_2-axis with the intermediate moment

of inertia, J_2, are *saddle point*s or *hyperbolic fixed point*s, which are passed through by *separatrices*. Near each saddle point, the trajectories are hyperbolas indicating that perturbed rotations are unstable [9-14]. Following the hyperbolic paths, the perturbed rotation deviates significantly from the permanent rotation state.

Poinsot also explained the body rotation with respect to the inertial coordinate system with the origin at the center of mass, point C. He plotted the angular momentum vector, $\mathbf{H}_C$, in the inertial coordinate space, where $\mathbf{H}_C$ remains constant, due to Eq. (17). Then, at the tip of the angular momentum vector, he defined a plane normal to the vector referred to as the *invariable plane*. The loci of the tip of the angular velocity vector on the invariable plane are called the *herpolhodes* to distinguish them from polhodes on the energy ellipsoid [9-13].

We have now summarized the theoretical background of a torque-free rotation of a rigid body. This summary is critical for the explanations of the Dzhanibekov and tennis racket phenomena.

2.1.6 The Dzhanibekov Phenomenon

On a space station in 1985, Vladimir Dzhanibekov, a Russian astronaut, conducted experiments concerning the rotation of a rigid body. For a rigid body with three distinct, moments of inertia, he applied an initial spin with each principal axis. His experiments in the space station were recorded and are available on-line.

In the space station, the gravitational attraction is negligible in Newton's equation (3b). Therefore, the translational velocity of a rigid body remains constant, and we only focus on the rotational motion of the body.

We attach a Cartesian coordinate system $\{s_1 \quad s_2 \quad s_3\}$ with the origin at the center of mass, point C, on a cuboid [4]. We choose the coordinate axes parallel to the edges to form principal coordinate axes. We name the axes, s_i, $i=1,2,3$, in the decreasing order of principal moment of inertia: $J_1 > J_2 > J_3 > 0$, as shown in Fig. 3 (a). The edges of the cuboid are $a < b < c$, in the s_1, s_2, and s_3-directions, respectively. The actual values of the principal moment of inertia are as follows:

$$J_1 = \frac{m}{12}(b^2 + c^2),\ J_2 = \frac{m}{12}(c^2 + a^2), \text{ and } J_3 = \frac{m}{12}(a^2 + b^2). \tag{21}$$

If the initial spin, $\hat{\omega}_0$, was applied to the cuboid's principal axis, $\mathbf{e}_1$, with the maximum moment of inertia, and the principal axis, $\mathbf{e}_3$, with the minimum moment of inertia, the cuboid continued rotating with the initial spin-axis unchanged. These spin behaviors can be easily interpreted as the result of the conservation of angular momentum since the rotational axes do not change with time.

If the cuboid, shown in Fig. 3 is spun with respect to the principal axis, $\mathbf{e}_2$—the axis with the intermediate moment of inertia—the cuboid initially rotates as expected, however, the other two rotations soon activate. The rotation about the other two axes is due to the growing component of either ω_1 or ω_3. This rotation was an unexpected event. In an experiment conducted on a wing nut, Dzhanibekov observed a similar phenomenon [3].

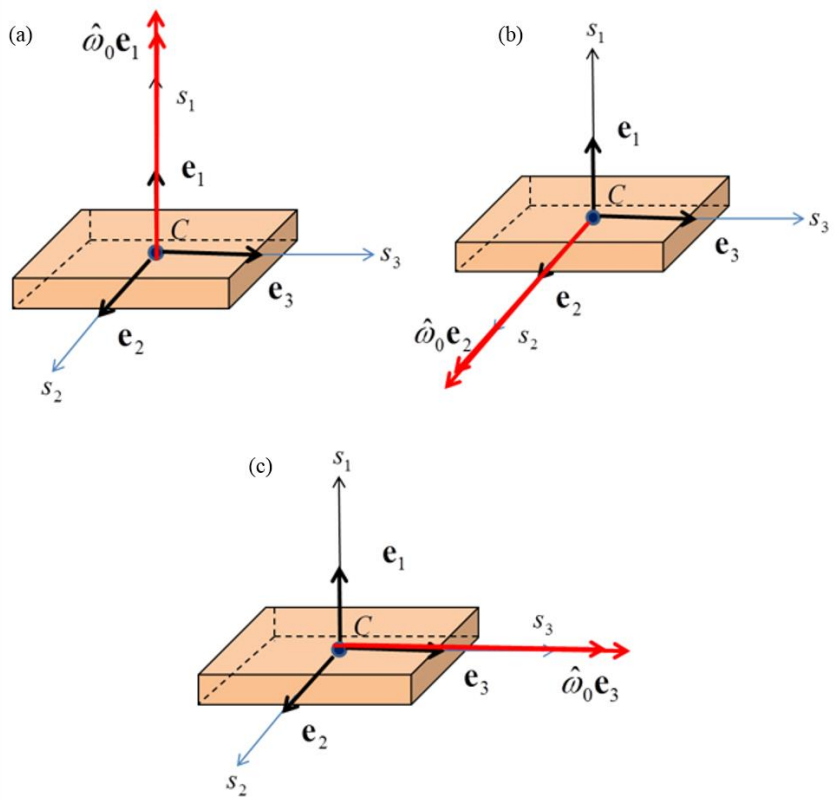

Figure 2-3: (a) A cuboid with an initial spin about the J_1 -axis; (b) with an initial spin about the J_2 -axis; and (c) an initial spin about the J_3 -axis

If we understand that the initial spin also includes minute perturbations, the unexpected rotational phenomenon, induced by an initial spin applied to the intermediate principal axis is easily explained by the hyperbolic orbits near the saddle points at the ends of the intermediate principal axis of a constant energy ellipsoid in Fig. 2. Furthermore, all the hyperbolic orbits near the intermediate permanent rotation are closed surrounding either the ω_1 - or the ω_3 -axis in Fig. 2. The closure of the orbit with either the ω_1 - or the ω_3 -axis implies that the initial spin axis also rotates periodically with the axis.

If one recalls that the conservation of angular momentum, Eq. (10), and the paragraph immediately following Eq. (18) do not prohibit the rotation of the initial spin

axis, Eq. (12a), the hyperbolic orbits near the saddle points explain Dzhanibekov's experiments. This includes the unexpected rotations observed when the initial spin was given with the intermediate axis.

Although polhodes are exact solutions, presented geometrically, they do not show: (i) how quickly or slowly each orbit is traced by the angular velocity vector and (ii) how the body is rotating with respect to the inertial coordinate frame. For this we overlay the power of geometry with that of numerical methods which will follow the next section.

2.1.7 The Tennis Racket Phenomenon

To explain the rotation of the racket, we define the principal coordinate system $\{s_1 \quad s_2 \quad s_3\}$ at the center of mass, as illustrated in Figs. 4 (a) and (b). The vector basis $\mathbf{e}(t) \equiv (\mathbf{e}_1(t) \quad \mathbf{e}_2(t) \quad \mathbf{e}_3(t))$ is defined using the unit tangent vectors to the coordinate axes. The s_2, s_3 -plane defines the head plane and the s_1 - axis is normal to the head plane. With this coordinate system, the principal mass moment of inertia appears in the decreasing order as: $J_1 > J_2 > J_3 > 0$. The moments of inertia of tennis rackets may be measured experimentally [15] since due to the symmetry, the principal planes are easily found.

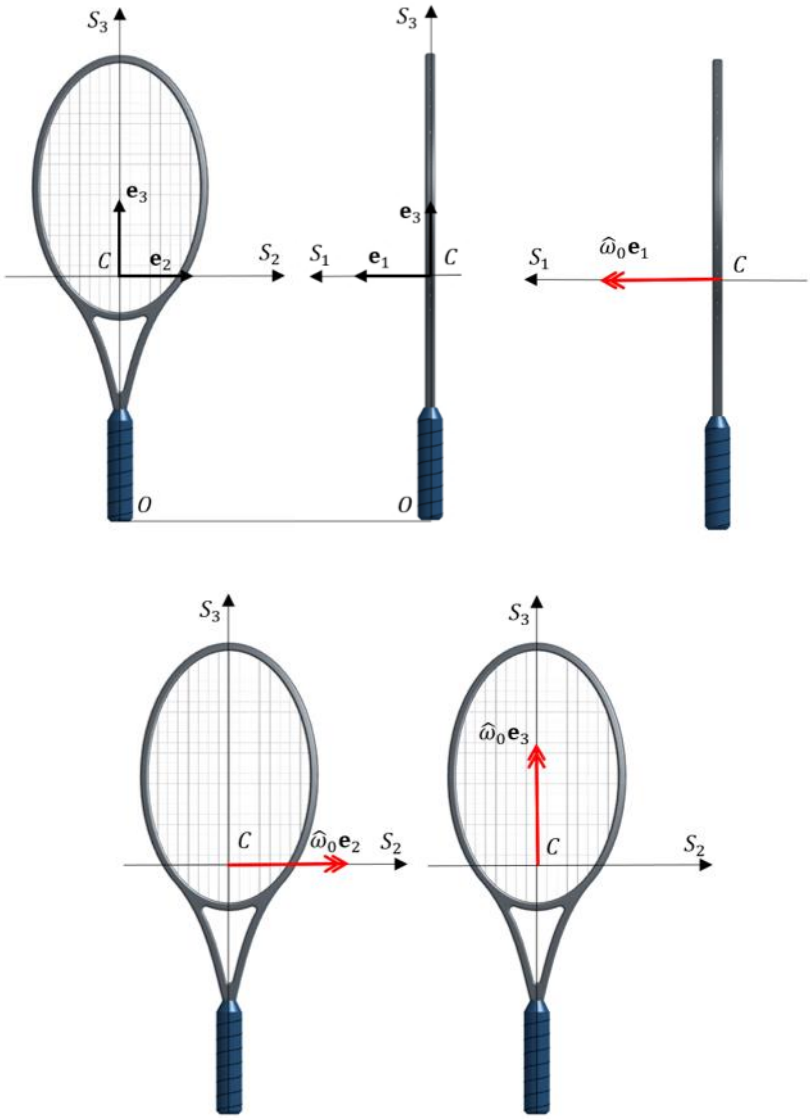

Figure 2-4: (a) The head plane of a tennis racket, (b) a side view normal to the head plane of the racket, (c) an initial spin with the normal axis to the head plane, (d), an initial spin with the axis normal to the grip axis, and (e) an initial spin with the grip axis.

To observe the rotational response, we toss a racket vertically up, simultaneously giving a spin along one of the principal axes of the racket. When we apply the initial spin with the s_1-axis with the maximum moment of inertia, the racket keeps spinning in a stable manner. A similar stable rotation is observed when the initial spin is applied with respect

to the s_3 - axis with the minimum moment of inertia. However, when the initial spin is applied with the s_2 - axis with the intermediate moment of inertia, in addition to the rotation of the racket with the s_2 -axis, the axis also rotates with the s_3 -axis. A recorded experiment is available online.

Although both Dzhanibekov's and the tennis racket phenomena are rotations of a torque-free body, the tennis racket experiment is ill-fated since it cannot demonstrate a periodic motion of the racket with the intermediate principal axis, shown in Fig. 4 (d). Due to gravity being a central force, the racket undergoes torque-free rotation as well as the vertical motion. The racket is up in the air only for a short duration. The time from the tossing to the catching is $2v_0 / g$ using Newton's equation (3b) if the initial vertical velocity given to the racket at the center of mass is $\dot{x}_0(0) = v_0$. Therefore, to compensate the shortcoming of the experiment, Poinsot's polhodes must be presented to reveal the nature of the tennis racket phenomenon.

In 1991, Ashbaugh, Chicone, and Cushman [16] reported the analytical solution for the tennis racket experiments by solving Eq. (12a) with respect to the components of the angular momentum vector. They only showed the final result and did not show the intermediate derivations. However, it is expected that their analysis parallels the analytical solution presented for the angular velocity components by Wittenburg [12, 13]. Both Wittenburg and Ashbaugh *et al*. used Euler angles to express the rotation of the tennis racket, but by doing so, critical points may be encountered.

Without showing the rotation of the body with respect to an inertial coordinate frame using three dimensional (3D) animations, it is difficult to explain the conservation of angular momentum regarding the strange rotation.

2.1.8 Work Presented in This Chapter

To summarize the background for the torque-free motion of a rigid body, a complete understanding consists of the two parts: (i) the solution of Euler's equations, Eqs. (13a-c) and (ii) the exhibition of the rotating body with respect to an inertial coordinate system, Eqs. (4) and (7a, b).

For the first part, an analysis is readily available. The analytical solution was obtained using the conservations of energy and angular momentum. Furthermore, polhodes on the energy ellipsoid help us understand the global rotational behavior. Although polhodes in Fig. 2 are easy to visualize, it is difficult to visualize the rotation of the body itself. The second part of the solution helps us visualize the rotating body with respect to an inertial coordinate system.

In the following, we analyze one of Dzhanibekov experiments concerning the motion of a wing nut as shown in the video [3]. In addition, we analyze a tennis racket experiment showing similar behavior [5]. Our approach employs numerical integration of Euler's torque-free equation and the *recovery equation for rotation matrix* in Eq. (4) to present 3D animations. To present the accuracy of the numerical solutions, we compare them with the orbits analytically obtained on the energy ellipsoid. The numerical analyses plotted on the energy ellipsoid supplement the missing information of the geometrical solution: how quickly or slowly each orbit is traced.

2.2 Formulation of the Torque-Free Rotation of a Rigid Body

We first formulate a torque-free rotation of a body with three distinct moment of inertia values. Then we present numerical integration scheme as well as the geometrical solution for the angular momentum.

2.2.1 Euler's Equation for a Torque-Free Body

We define the initial value problem of the angular momentum vector expressed by the body-attached coordinate frame, $\mathbf{e}(t)$, Eq. (9a). Euler's equations (12a) can be rewritten using the inverse of Eq. (9b) as follows:

$$\mathbf{e}_1(t): \quad \dot{H}_{1C}(t) + (\frac{1}{J_{2C}} - \frac{1}{J_{3C}}) H_{2C}(t) H_{3C}(t) = 0, \tag{22a}$$

$$\mathbf{e}_2(t): \quad \dot{H}_{2C}(t) + (\frac{1}{J_{3C}} - \frac{1}{J_{1C}}) H_{3C}(t) H_{1C}(t) = 0, \tag{22b}$$

$$\mathbf{e}_3(t): \quad \dot{H}_{3C}(t) + (\frac{1}{J_{1C}} - \frac{1}{J_{2C}}) H_{1C}(t) H_{2C}(t) = 0. \tag{22c}$$

The initial conditions at $t = 0$ are prescribed as:

$$\begin{pmatrix} H_{1C}(0) \\ H_{2C}(0) \\ H_{3C}(0) \end{pmatrix} = \begin{pmatrix} J_{1C}\omega_1(0) \\ J_{2C}\omega_2(0) \\ J_{3C}\omega_3(0) \end{pmatrix} = \begin{pmatrix} \hat{H}_1 \\ \hat{H}_2 \\ \hat{H}_3 \end{pmatrix}, \tag{23}$$

where $\hat{H}_1, \hat{H}_2$, and $\hat{H}_3$ are constants.

We will integrate Eqs. (22a-c) using the fourth-order Runge-Kutta method for discrete time with time increment Δt. For given values of $H_{iC}(t)$, Eqs. (22a-c) give $H_{iC}(t+\Delta t)$, $i = 1,2,3$. For the known angular momentum vector components, the angular velocity components $\omega(t)$ and $\omega(t+\Delta t)$ can be computed from the known angular momentum components using the inverse of Eq. (9b). Although the analytical

solution of Eqs. (22a-c) in terms of the Jacobi elliptic functions is available [14, 15], we find that solution not amenable to the imposition of arbitrarily selected initial conditions with some disturbances. Therefore, we chose to adopt the easily available numerical solutions and used the analytical solution for validation.

Next, we present the time integration of the angular velocity matrix in Eq. (7b) to find the rotation matrix *without using angular coordinates*.

2.2.2 Reconstruction of Rotation Matrix

When a rigid body freely rotates, any coordinate representation using three angular-coordinates may experience a critical point. To avoid critical points, four angular-coordinates, *e.g.*: quaternions, are used to express rotation matrices [17, 18]. However, the resulting equations of motion become more complicated than the original Euler's equations. Here, a simpler method is presented to deal with rotation matrices directly without resorting to four angular coordinates. Also, there are no critical points where the representation of rotation fails.

Equation (7b) gives *reconstruction formula* for $R(t)$ [6,1 9]:

$$\dot{R}(t) = R(t)\overleftrightarrow{\omega(t)}. \tag{24}$$

When the angular velocity remains constant, $\omega(t) = \omega_0$, Eq. (24) can be integrated analytically. Using the constant angular velocity case, we will develop a numerical integration scheme for time dependent angular velocity cases.

The solution of Eq. (24) with the initial value $R(0)$ becomes [5]:

$$R(t) = R(0)\exp(t\overleftrightarrow{\omega_0}), \tag{25}$$

where the matrix exponential is defined as:

$$\exp(t\overleftrightarrow{\omega_0}) \equiv I_d + t\overleftrightarrow{\omega_0} + \frac{t^2}{2!}(\overleftrightarrow{\omega_0})^2 + \frac{t^3}{3!}(\overleftrightarrow{\omega_0})^3 + \cdots = \sum_{k=0}^{\infty} \frac{t^k}{k!}(\overleftrightarrow{\omega_0})^k . \tag{26}$$

In order for Eq. (25) to be useful, we need a simple expression for the matrix exponential. In what follows, we simplify Eq. (26) using the *Cayley-Hamilton theorem* [20].

To simplify the computation of $(\overleftrightarrow{\omega_0})^k$ in Eq. (25), we first compute the characteristic equation of $\overleftrightarrow{\omega_0}$:

$$\det(\overleftrightarrow{\omega_0} - \lambda I_d) = \det\begin{bmatrix} -\lambda & -\omega_{30} & \omega_{20} \\ \omega_{30} & -\lambda & -\omega_{10} \\ -\omega_{20} & \omega_{10} & -\lambda \end{bmatrix} = -\lambda^3 - \|\boldsymbol{\omega}_0\|^2 \lambda = 0 , \tag{27a}$$

where

$$\|\boldsymbol{\omega}_0\|^2 = (\omega_{01})^2 + (\omega_{02})^2 + (\omega_{03})^2 . \tag{27b}$$

From Eq. (27a), the Cayley-Hamilton theorem gives

$$(\overleftrightarrow{\omega_0})^3 = -\|\boldsymbol{\omega}_0\|^2 (\overleftrightarrow{\omega_0}) . \tag{28}$$

Using Eq. (28), the right-hand side of Eq. (26) is expressed by $\boldsymbol{I}_d$, the 3×3 identity matrix, $\overleftrightarrow{\omega}_0$, and $(\overleftrightarrow{\omega}_0)^2$:

$$\exp(t\overleftrightarrow{\omega_0}) \equiv I_d + t\overleftrightarrow{\omega_0} + \frac{t^2}{2!}(\overleftrightarrow{\omega_0})^2 - \frac{t^3}{3!}\|\boldsymbol{\omega}_0\|^2 \overleftrightarrow{\omega_0} - \frac{t^4}{4!}\|\boldsymbol{\omega}_0\|^2 (\overleftrightarrow{\omega_0})^2 + \frac{t^5}{5!}\|\boldsymbol{\omega}_0\|^4 \overleftrightarrow{\omega_0} + \frac{t^6}{6!}\|\boldsymbol{\omega}_0\|^4 (\overleftrightarrow{\omega_0})^2 - \cdots .$$

Collecting each power of $\overleftrightarrow{\omega_0}$, we obtain

$$\exp(t\overleftrightarrow{\omega_0}) \equiv I_d + \overleftrightarrow{\omega_0}\{t - \frac{t^3}{3!}\|\boldsymbol{\omega}_0\|^2 + \frac{t^5}{5!}\|\boldsymbol{\omega}_0\|^4 - \frac{t^7}{7!}\|\boldsymbol{\omega}_0\|^6 + \cdots\}$$

$$+(\overleftrightarrow{\omega_0})^2\{\frac{t^2}{2!}-\frac{t^4}{4!}\|\boldsymbol{\omega}_0\|^2+\frac{t^6}{6!}\|\boldsymbol{\omega}_0\|^4-\frac{t^8}{8!}\|\boldsymbol{\omega}_0\|^6+\cdots\}.$$

$$\exp(t\overleftrightarrow{\omega_0})\equiv I_d+\frac{\overleftrightarrow{\omega_0}}{\|\boldsymbol{\omega}_0\|}\{t\|\boldsymbol{\omega}_0\|-\frac{1}{3!}(t\|\boldsymbol{\omega}_0\|)^3+\frac{1}{5!}(t\|\boldsymbol{\omega}_0\|)^5-\frac{1}{7!}(t\|\boldsymbol{\omega}_0\|)^7+\cdots\}$$

$$+\left(\frac{\overleftrightarrow{\omega_0}}{\|\boldsymbol{\omega}_0\|}\right)^2\{\frac{1}{2!}(t\|\boldsymbol{\omega}_0\|)^2-\frac{1}{4!}(t\|\boldsymbol{\omega}_0\|)^4+\frac{1}{6!}(t\|\boldsymbol{\omega}_0\|)^6-\frac{1}{8!}(t\|\boldsymbol{\omega}_0\|)^8+\cdots\}.$$

Finally, the simplified equation is found:

$$\exp(t\overleftrightarrow{\omega_0})\equiv I_d+\frac{\overleftrightarrow{\omega_0}}{\|\boldsymbol{\omega}_0\|}\sin(t\|\boldsymbol{\omega}_0\|)+\left(\frac{\overleftrightarrow{\omega_0}}{\|\boldsymbol{\omega}_0\|}\right)^2(1-\cos(t\|\boldsymbol{\omega}_0\|)). \tag{29}$$

If we define a unit vector $\mathbf{u}=\boldsymbol{\omega}_0/\|\boldsymbol{\omega}_0\|$ in the direction of the angular velocity vector, Eq. (29) agrees with the *Rodrigues formula* [12, 13]. The present linear algebraic analysis yields the same result as the geometric analysis adopted by Rodrigues.

Equation (29) is used in the numerical integration of Eq. (24) when the angular velocity changes with time with relatively small time steps.

2.2.3 Numerical Integration of the Reconstruction Formula for Rotation Matrix

We can integrate Eq. (24) analytically from t to $t+\Delta t$ if the angular velocity is constant. While this criterion is not met under the current phenomena, it can be applied by approximation to each time step of the Runge-Kutta integration. Therefore, we adopt the *mid-point integration method* using the mean value of the angular velocity, $\omega(t+\Delta t/2)$ [24]:

$$\omega(t+\Delta t/2)\equiv\{\omega(t)+\omega(t+\Delta t)\}/2. \tag{30}$$

Assuming that the angular velocity is constant during the time step from t to $t+\Delta t$, we integrate Eq. (24) analytically for the initial value of $R(t)$ to find $R(t+\Delta t)$:

$$R(t+\Delta t) = R(t)\exp\{\Delta t\,\overleftrightarrow{\omega(t+\Delta t/2)}\}, \tag{31}$$

where Eq. (29) is used to evaluate the exponential matrix for $\omega_0 = \omega(t+\Delta t/2)$.

2.2.4 Geometrical Solutions

The exact analytical solution is evinced geometrically using the two integrals of Euler's equations, Eq. (22a-c): the conservations of energy and the conservation of the magnitude of the angular momentum vector.

We use Eq. (16b) to construct the energy ellipsoid expressed with respect to the H_{1C}, H_{2C}, and H_{3C}-axes as follows.

Let the initial rotational kinetic energy be denoted by K_0. The energy ellipsoid is expressed as:

$$\left(\frac{H_{1C}(t)}{\sqrt{2K_0J_{1C}}}\right)^2 + \left(\frac{H_{2C}(t)}{\sqrt{2K_0J_{2C}}}\right)^2 + \left(\frac{H_{3C}(t)}{\sqrt{2K_0J_{3C}}}\right)^2 = 1. \tag{32a}$$

where

$$K_0 \equiv K_{rot}(0) = \left\{(\hat{H}_1)^2/J_{1C} + (\hat{H}_2)^2/J_{2C} + (\hat{H}_3)^2/J_{3C}\right\}/2. \tag{32b}$$

The major semi-axis of the ellipsoid is $\sqrt{2K_0J_{1C}}$ along the body-attached H_{1C}-axis, the intermediate semi-axis is $\sqrt{2K_0J_{2C}}$ along the body-attached H_{2C}-axis and the minor semi-axis $\sqrt{2K_0J_{3C}}$ along the body-attached H_{3C}-axis.

We use Eq. (19b) to construct the angular momentum sphere:

$$(H_{1C}(t))^2 + (H_{2C}(t))^2 + (H_{3C}(t))^2 = 2K_0D, \tag{33a}$$

where $\sqrt{2K_0D}$ represents the radius of the sphere as well as the magnitude of the angular

momentum vector. Here, we have parameterized the squared magnitude of the angular momentum vector by introducing a parameter *D* as:

$$2K_0 D \equiv \left\| \mathbf{H}_C(0) \right\|^2 \equiv (\hat{H}_1)^2 + (\hat{H}_2)^2 + (\hat{H}_3)^2, \tag{33b}$$

where *D* has the dimension of the moment of inertia, J_{iC} .

By changing the radius $\sqrt{2K_0 D}$ of the angular momentum sphere through the parameter *D*, we can find the exact trajectories of the angular momentum vector. This is done by expressing the intersections between the energy ellipsoid, Eq. (32a), and the angular momentum spheres of various radii, Eq. (33a) in the body-attached frame.

Before continuing, we remind the reader that we will leverage the following inequality: $J_{1C} > J_{2C} > J_{3C} > 0$. For a sphere to intersect with the energy ellipsoid, its radius $\sqrt{2K_0 D}$ must be less than or equal to the major semi-axis of the ellipsoid and greater than or equal to the minor semi-axis. This requirement imposes the inequality for the parameter *D*:

$$J_{3C} \le D \le J_{1C} \ . \tag{34}$$

The intersection of the ellipsoid and the sphere shows the exact trajectories of the angular momentum vector expressed with the body-attached coordinate frame.

We now plot the constant energy ellipsoid and intersecting spheres of various radii, *i.e.*, different magnitudes of the angular momentum vector. To do this, we first non-dimensionalize Eqs. (32a) and (33b) using J_{2C}. The non-dimensional angular momentum components and the ratio of moments of inertia are shown by over-bars:

$$\overline{H}_{iC} = H_{iC} / \sqrt{2K_0 J_{2C}} \ , i = 1, 2, 3, \tag{35a}$$

$$\bar{d} = D / J_{2C}. \tag{35b}$$

The non-dimensional energy ellipsoid becomes, from Eqs. (32a) and (35):

$$\left(\frac{J_{2C}}{J_{1C}}\right)\left(\overline{H}_{1C}\right)^2 + \left(\overline{H}_{2C}\right)^2 + \left(\frac{J_{2C}}{J_{3C}}\right)\left(\overline{H}_{3C}\right)^2 = 1. \tag{36}$$

The major semi-axis of the ellipsoid is $\sqrt{J_{1C} / J_{2C}}$ along the body-attached $\overline{H}_{1C}$-axis, the intermediate semi-axis is one along the body-attached $\overline{H}_{2C}$-axis and the minor semi-axis $\sqrt{J_{3C} / J_{2C}}$ along the body-attached $\overline{H}_{3C}$-axis.

The non-dimensional angular momentum sphere is obtained from Eqs. (33b) and (35):

$$\left(\overline{H}_{1C}\right)^2 + \left(\overline{H}_{2C}\right)^2 + \left(\overline{H}_{3C}\right)^2 = \bar{d}\,, \tag{37a}$$

where the radius $\sqrt{\bar{d}}$ of the sphere satisfies the non-dimensional inequality imposed by Eq. (34):

$$\frac{J_{3C}}{J_{2C}} \le \bar{d} \le \frac{J_{1C}}{J_{2C}}. \tag{37b}$$

We first consider the projection on to the $\overline{H}_{2C}$, $\overline{H}_{3C}$-plane. The equation for the trajectory is obtained by eliminating $\overline{H}_{1C}$ from Eqs. (36) and (37a):

$$\left(1 - \frac{J_{2C}}{J_{1C}}\right)\left(\overline{H}_{2C}\right)^2 + \left(\frac{J_{2C}}{J_{3C}} - \frac{J_{2C}}{J_{1C}}\right)\left(\overline{H}_{3C}\right)^2 = \left(1 - \frac{J_{2C}}{J_{1C}}\bar{d}\right) \ge 0. \tag{38}$$

Here, the inequality on the right–hand side is obtained by using the inequality (37b). The coefficients on the left hand side are both positive. Therefore, Eq. (38) shows an ellipse if the right-hand-side is positive. Otherwise it shows the state of permanent rotation:

$\overline{H}_{1C} = \sqrt{\overline{d}}$, $\overline{H}_{2C} = \overline{H}_{3C} = 0$. These elliptic trajectories appear inside the projected energy at $\overline{H}_{1C} = 0$ in Eq. (36).

Second, we consider the projection on to the $\overline{H}_{1C}$, $\overline{H}_{2C}$ -plane. The equation for the trajectory is obtained by eliminating $\overline{H}_{3C}$ from Eqs. (36) and (37a):

$$\left(\frac{J_{2C}}{J_{3C}} - \frac{J_{2C}}{J_{1C}} \right) \left(\overline{H}_{1C} \right)^2 + \left(\frac{J_{2C}}{J_{3C}} - 1 \right) \left(\overline{H}_{2C} \right)^2 = \left(\frac{J_{2C}}{J_{3C}} \overline{d} - 1 \right) \geq 0 . \tag{39}$$

Here, the inequality on the right–hand side is obtained by using the inequality (37b). Since the coefficients on the left hand side are both positive, Eq. (39) represents an ellipse if the right-hand side does not vanish, $\overline{d} > J_{3C} / J_{2C}$, *i.e.,* $D > J_{3C}$. If the right-hand side of Eq. (39) vanishes, $\overline{d} = J_{3C} / J_{2C}$, *i.e.,* $D = J_{3C}$, it becomes a point showing the state of permanent rotation: $\overline{H}_{1C} = \overline{H}_{2C} = 0$ and $\overline{H}_{3C} = \sqrt{\overline{d}}$. The projection of the energy ellipsoid becomes an ellipse at $\overline{H}_{3C} = 0$ in Eq. (36).

Finally, we consider the projection on to the $\overline{H}_{1C}$, $\overline{H}_{3C}$ -plane. The projected ellipsoid becomes an ellipse at $\overline{H}_{2C} = 0$ in Eq. (36). The equation for the trajectory is obtained by eliminating $\overline{H}_{2C}$ from Eqs. (36) and (37a):

$$-\left(1 - \frac{J_{2C}}{J_{1C}} \right) \left(\overline{H}_{1C} \right)^2 + \left(\frac{J_{2C}}{J_{3C}} - 1 \right) \left(\overline{H}_{3C} \right)^2 = 1 - \overline{d} . \tag{40a}$$

Here, the coefficients in pairs of parentheses on the left hand side are both positive. Therefore, Eq. (40a) shows a hyperbola. The equations of its *asymptotes* are

$$\overline{H}_{3C} = \pm\sqrt{\frac{J_{3C}(J_{1C} - J_{2C})}{J_{1C}(J_{2C} - J_{3C})}}\,\overline{H}_{2C}. \tag{40b}$$

If $\bar{d} < 1$, the vertices and focal points of the hyperbola are on the $\overline{H}_{3C}$-axis in the projected plane. Therefore, on the energy ellipsoid, *the trajectory is closed and circulates about the* $\overline{H}_{3C}$*-axis*. On the contrary, if $\bar{d} > 1$, the vertices and focal points of the hyperbola are on the $\overline{H}_{1C}$-axis in the projected plane. Therefore, on the energy ellipsoid, *the trajectory is closed and circulates about the* $\overline{H}_{1C}$*-axis*.

When $\bar{d} = 1$, *i.e.*, $D = J_{2C}$, the trajectory of Eq. (40a) also becomes Eq. (40b). Therefore, Eq. (40b) becomes separatrices. Furthermore, $\overline{H}_{1C} = \overline{H}_{3C} = 0$ represents the state of permanent rotation: $\overline{H}_{2C} = 1$.

Figure 5 (a) shows the intersecting energy ellipsoid and the angular momentum sphere for $J_{1C} / J_{2C} = 2$ and $J_{3C} / J_{2C} = 0.5$. For $\bar{d} = 0.65$, 0.8, 0.95, 1.05, 1.20, 1.35, 1.5, 1.65, 1.8, and 1.95, the projected trajectories onto the $\overline{H}_{2C}, \overline{H}_{3C}$-plane is shown in Fig. 5 (b), those onto the $\overline{H}_{1C}, \overline{H}_{3C}$-plane is in Fig. 5 (c), and those onto the $\overline{H}_{1C}, \overline{H}_{2C}$-plane in Fig. 5 (d).

As Fig. 5 (a) illustrates, the trajectories that form a pair of hyperbolas on the projected $\overline{H}_{1C}, \overline{H}_{3C}$-plane is closed on the energy ellipsoid, indicating that the rotation is periodic.

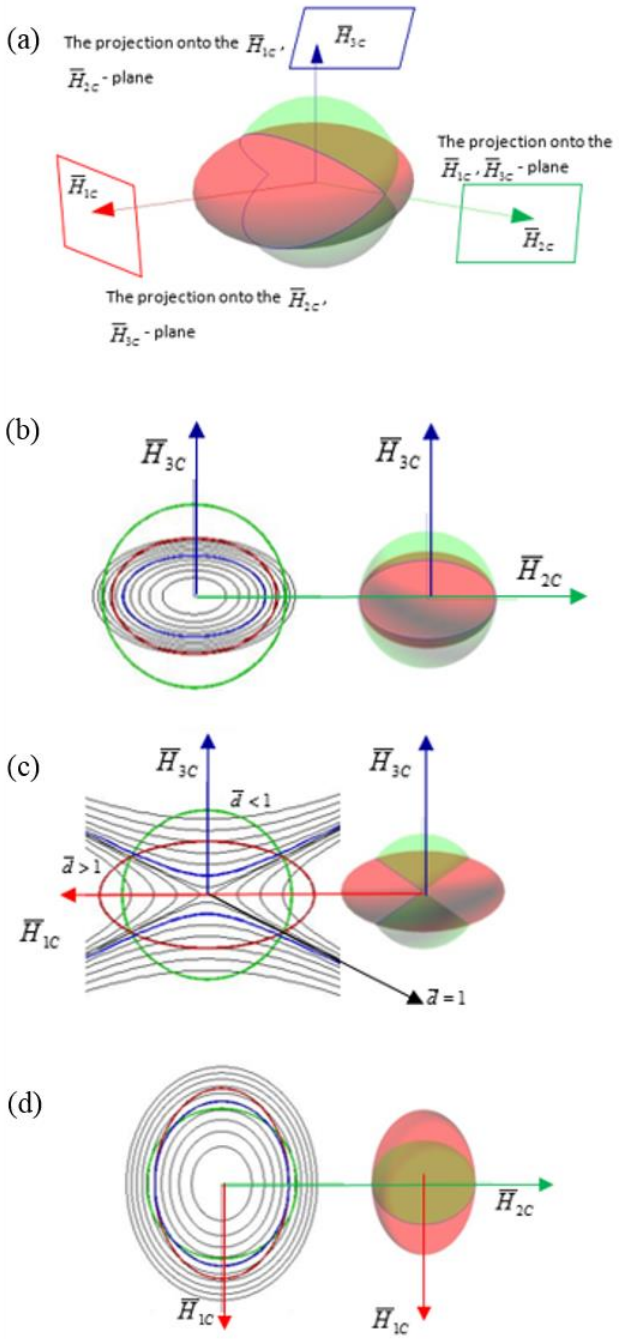

Figure 2-5: (a) Angular momentum trajectories which are intersections between the energy ellipsoid and the angular momentum sphere for $J_{1C}/J_{2C}=2.0$ and $J_{3C}/J_{2C}=0.5$. For $\bar{d}=0.65, 0.8, 0.95, 1.05, 1.20, 1.35, 1.5, 1.65, 1.8, 1.95$, the projection of the trajectories: (b) onto the $\overline{H}_{2C},\overline{H}_{3C}$-plane, (c) onto the $\overline{H}_{1C},\overline{H}_{3C}$-plane, and (d) onto the plane $\overline{H}_{1C},\overline{H}_{2C}$-plane

2.3 Numerical Results

We present the numerical simulations of Dzhanibekov's experiment of an unscrewing wing nut and the tennis racket experiment. For numerical solutions, we integrate Euler's equations (22a-c) using the fourth-order Runge-Kutta method and the recovery formula for the rotation matrix, Eq. (24), using the mid-point method, Eq. (31) and Eq. (29). Using the recovered rotation matrices, 3D animations have been developed for both the wing nut and the tennis racket experiments, available at http://tinyurl.com/ucsdhib [22]. The animations provide the necessary visual tool to connect and validate the numerical solutions with the experiments.

2.3.1 Dzhanibekov's Experiment

For the numerical simulation, we used the following properties for the mass moment of inertia of the wing nut: $J_{1C} = 3.036 \times 10^{-6}$ kg/m^2, $J_{2C} = 2.741 \times 10^{-6}$ kg/m^2, and $J_{3C} = 0.699 \times 10^{-6}$ kg/m^2. The intermediate moment of inertia appears in the axial direction of the nut, as illustrated in Fig. 6. The ratios of the moments of inertia become $J_{1C} / J_{2C} = 1.11$ and $J_{3C} / J_{2C} = 0.26$.

In the simulation, an unscrewed wing nut advances to the left. Time $t = 0$ is set to be just before it separates from the bolt with a major angular momentum of $H_{2C}(0) = 2.1252 \times 10^{-5}$ kg/m^2 s and minute disturbances $H_{1C}(0) = 0.001 \times 10^{-5}$ kg/m^2 s and $H_{3C}(0) = 0.001 \times 10^{-5}$ kg/m^{2}s. For the initial conditions, the computation of the rotational energy and the magnitude of the angular momentum vector gives $\bar{d} = D / J_{2C} \cong 1.0$. An inertial coordinate frame is selected to be the body-attached frame at $t = 0$: $\mathbf{e}^I = \mathbf{e}(0)$.

Figure 6 (a) shows the snap shots at times t = 0.00, 4.75, 5.25, 5.50 and 7.00 seconds [22]. The first-row image shows the configuration at t = 0, and the snap shots in the second row start from the leftmost figure at t = 4.75s and show the wing nut at 5.25, 5.50 and 7.00s. The figures qualitatively reproduce the periodic rotation of the wing nut observed by Dzhanibekov in space.

Figure 6(b) presents the angular momentum about the inertial coordinate axes. The magnitude and the x_2-component of the angular momentum (black lines) have the common value of 2.1252×10^{-5} kg-m^2/s. The components of the angular momentum about the x_1 and x_3-axes (blue) are both 0.0.

Figure 6(c) presents the angular momentum about the body-attached axes, and the magnitude of the angular momentum (black line 'total'); the latter retains the value 2.1252×10^{-5} kg-m^2/s.

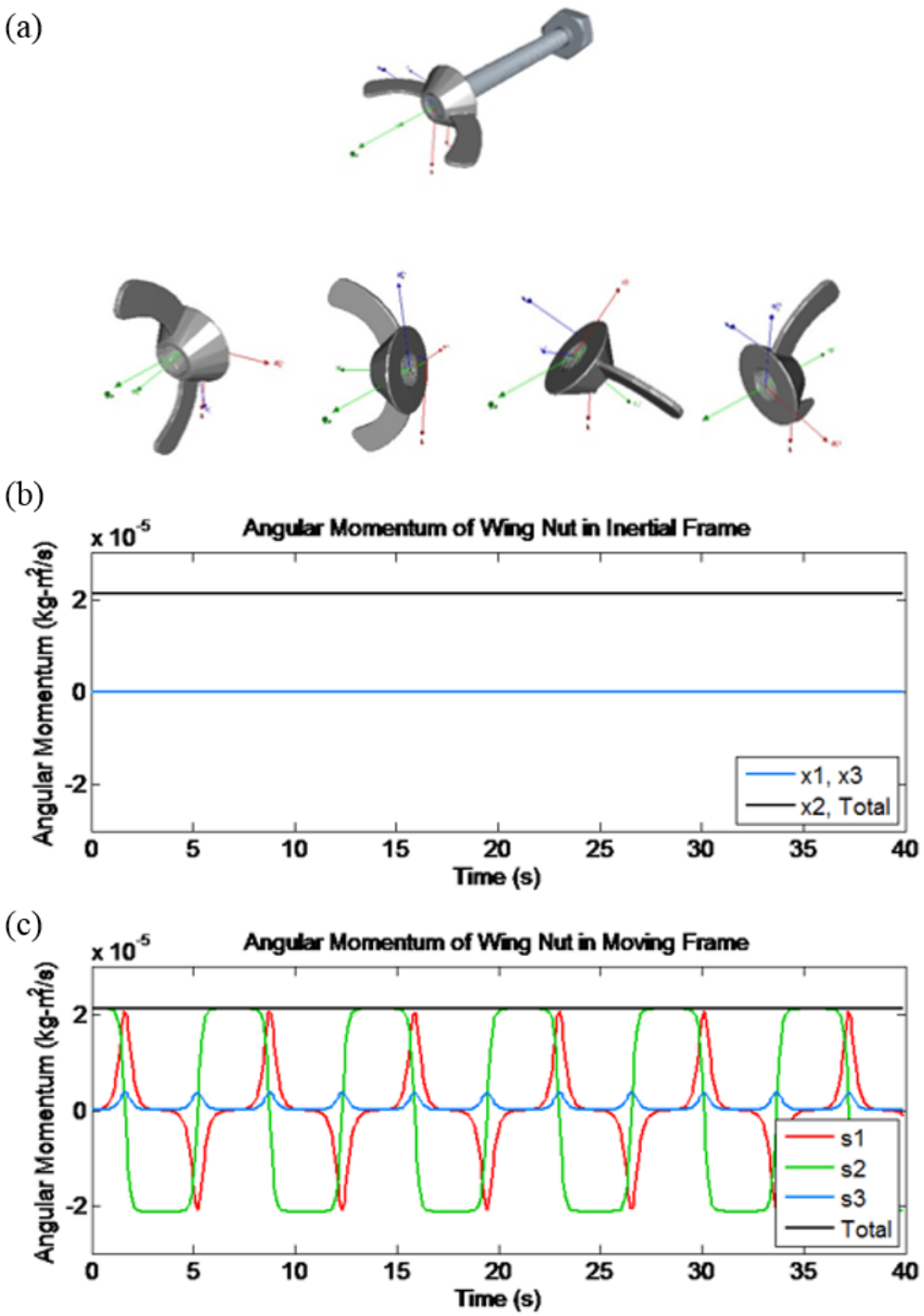

Figure 2-6: (a) A sequence of snap shots of the wing nut at times t = 50.00, 4.75, 5.25, 5.50, and 7.00 s (b) The magnitude and the components of the angular momentum vector about the inertial coordinate axes and (c) about the body-attached coordinate axes

2.3.2 The Tennis Racket Experiment

We present the simulation of a tennis racket, illustrated in Fig. 4. The parameters are m = 0.375 kg, J_{1C} = 0.0185 kg/m^2, J_{2C} = 0.0164 kg/m^2, J_{3C} = 0.00121 kg/m^2. We only present the result when the initial spin is applied with the $\mathbf{e}_2$-axis in Fig. 4 (d). The initial angular velocities are:

$$\omega_2(0) = 5.0 \text{ rad/s}, \ \omega_1(0) = \omega_3(0) = 0.001 \text{ rad/s}.$$

The vertical velocity of 24.5 m/s is applied at the center of mass, which gives the racket air time of 5 seconds. The initial value gives $\bar{d} = D / J_{2C} \cong 1$. An inertial coordinate frame is selected to be the body-attached frame at t = 0: $\mathbf{e}^I = \mathbf{e}(0)$.

Figure 7 (a) shows a sequence of snap shots of the tennis racket, in the first row at t = 0 and in the second row from the leftmost figure at t = 1.4, 1.8, 3.0, and 4.0 s [22].

Figure 7 (b) illustrates the inertial components of the angular velocity as well as the magnitude of the angular velocity vector. The x_2-component and the magnitude of the vector display the common value of 0.082 kg-m^2/s (black lines). The angular velocity components in the x_3- and x_1-directions remain zero (blue lines).

Figure 7 (c) presents the angular momentum about the body-attached coordinate axes. The magnitude of the angular momentum vector (black line ‘total’) retains the same value of 0.082 kg-m^2/s.

(a)

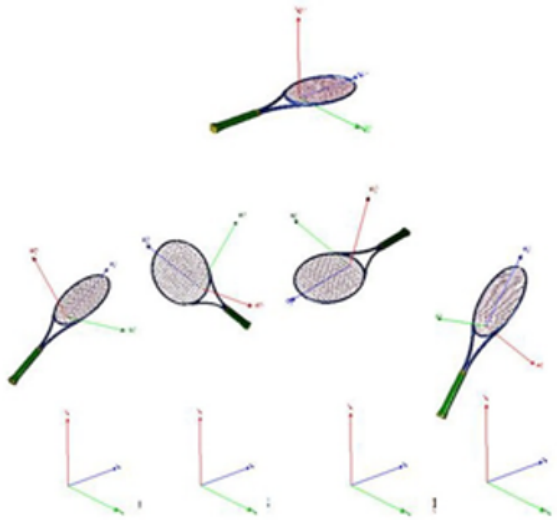

(b)

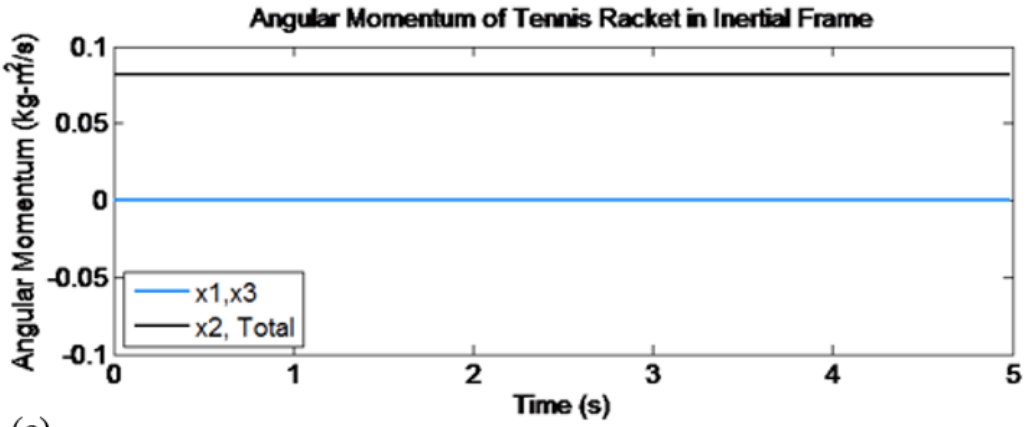

(c)

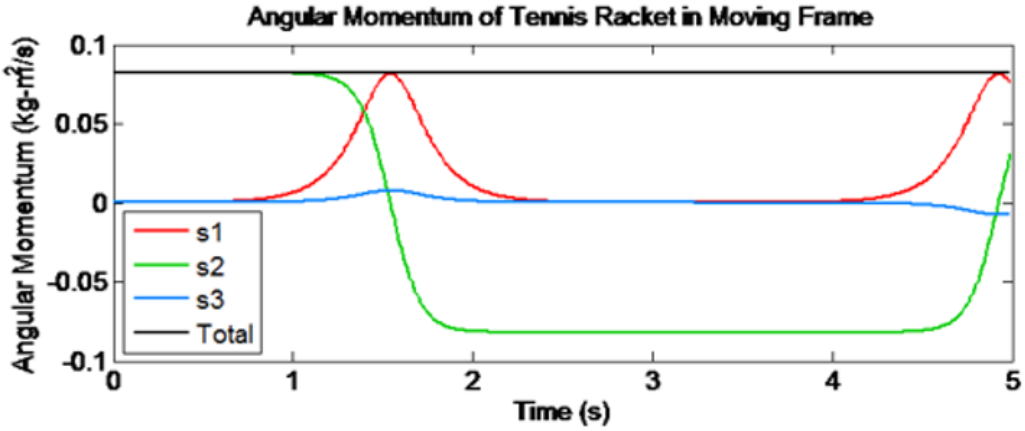

Figure 2-7: (a) A sequence of snap shots of the wing nut: t = 50.0, 1.4, 1.8, 3.0, and 4.0 s. The components of the angular momentum vector about the inertial coordinate axes and its magnitude (b); about the body-attached coordinate axes and its magnitude (c)

The accuracy of the numerical solutions was checked both geometrically and analytically. To compare the momentum's trajectory with the geometrically exact trajectory, the angular momentum vector was plotted on the angular momentum sphere, shown in Fig. 5 (a). This geometrically exact trajectory is the intersection between the energy ellipsoid and the angular momentum sphere. For both simulations of the Dzhanibekov and the tennis racket experiments, the numerically computed trajectories of the angular momentum vector are indistinguishably close to the exact orbit.

The accuracy of the numerical simulation for the tennis racket experiment was compared with the analytical solution [12, 13] in Fig. 8. The relative maximum error was 0.19%. The presentation of the analytical solution can be seen in a separate publication, where this analysis was further applied to the stability of a satellite as the solar panels open [23].

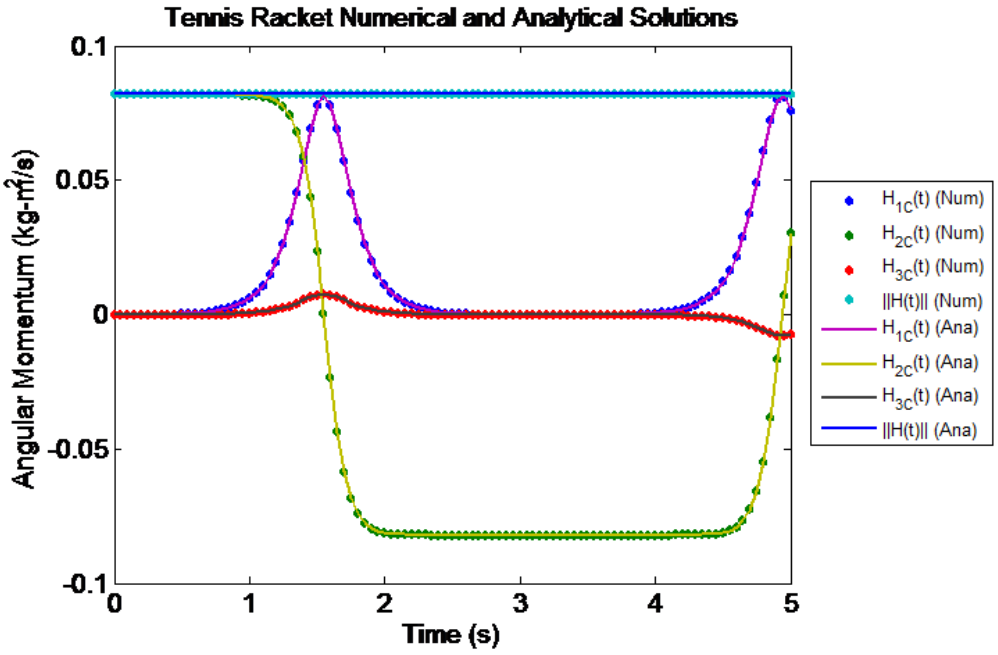

Figure 2-8: Comparisons between the numerical (dotted) and the analytical (solid line) solutions for the tennis racket

2.4 Concluding Remarks

In both the Dzhanibekov and tennis racket experiments, an initial angular velocity about the principal axes of the smallest and largest moment of inertias creates stable permanent rotations. This is easily interpreted as the result of the conservation of angular momentum. However, when the initial rotation is applied to the principal axis of the intermediate moment of inertia value, the body exhibits rotations about the other axes. This unstable rotation could be easily misinterpreted as evidence for violating the conservation of angular momentum in torque-free motion. In this Chapter, it was theoretically and numerically demonstrated (the latter with 3D animations) that the rotations are periodic with the principal axis of the intermediate moment of inertia. Our computational approach employs numerical integration of Euler's torque-free equation and a recovery equation for rotation matrices to present 3D animations.

Chapter 2, in part, is published as "A Theoretical and Numerical Study of the Dzhanibekov and Tennis Racket Phenomena." *Journal of Applied Mechanics* 83.11 (2016): 111006. This work was coauthored by H. Murakami, T. Ono, and T.J. Impelluso. The dissertation author is the second author of this work.

Chapter 2, in part, is published as "A Theoretical and Numerical Study of the Dzhanibekov and Tennis Racket Phenomena." *ASME 2015 International Mechanical Engineering Congress and Exposition*. American Society of Mechanical Engineers, 2015. This work was coauthored by H. Murakami, T. Ono, and T.J. Impelluso. The dissertation author is the second author of this work.

2.5 References

[1] Euler, L., 1758, “Du mouvement de rotation des corps solides autour d’un axe variable,” M_emoires de l’acad_emie des sciences de Berlin, Vol. 14, Berlin Academy, Berlin, Germany, pp. 154–193.,

[2] Euler, L., 1964, “Du mouvement de rotation des corps solides autour d’un axe variable,” Opera Omnia: Commentationes Mechanicae ad Theoriam Corporum Rigidorum Pertinentes, volumen prius, Orell F€ussli, Z€urich, Switzerland, pp. 200–235.

[3] Cartan, _E., 1928, Lec¸ons sur la G_eom_etrie des Espaces de Riemann, Gauthiers-Villars, Paris, France.

[4] Cartan, E., 1986, On Manifolds With an Affine Connection and the Theory of General Relativity (Translated by A. Magnon and A. Ashtekar), Bibiliopolis, Napels, Italy.

[5] Frankel, T., 2012, The Geometry of Physics: An Introduction, 3rd ed., Cambridge University Press, New York.

[6] Murakami, H., 2013, “A Moving Frame Method for Multi-Body Dynamics,” ASME Paper No. IMECE2013-62833.

[7] Synge, J. L., 1960, “Classical Dynamics,” Principles of Classical Mechanics and Field Theory (Encyclopedia of Physics), Vol. III/1, S. Fl€ugge, ed., Springer-Verlag, Berlin, Germany.

[8] Landau, L. D., and Lifshitz, E. M., 1960, Mechanics (Translated From Russian by J. B. Sykes and J. S. Bell), Pergamon Press, New York.

[9] Goldstein, H., 1980, Classical Mechanics, 2nd ed., Addison-Wesley Publishing, Reading, MA.

[10] Greenwood, D. T., 1965, Principle of Dynamics, Prentice-Hall, Englewood Cliffs, NJ.

[11] Arnold, V. I., 1989, Mathematical Methods of Classical Mechanics, 2nd ed., Springer-Verlag, New York.

[12] Wittenburg, J., 1977, Dynamics of Rigid Bodies, B. G. Teubner, Stuttgart, Germany.

[13] Wittenburg, J., 2008, Dynamics of Multibody Systems, 2nd ed., Springer, Berlin, Germany.

[14] Poinsot, L., 1834, Theorie Nouvelle de la Rotation des Corps, Bachelier, Paris, France.

[15] Brody, H., 1985, "The Moment of Inertia of a Tennis Racket," Phys. Teach., 23(4), pp. 213–216.

[16] Ashbaugh, M., Chicone, C. C., and Cushman, A. H., 1991, "The Twisting Tennis Racket," J. Dyn. Differ. Equations, 3(1), pp. 67–85.

[17] Haug, E. J., 1989, Computer-Aided Kinematics and Dynamics of Mechanical Systems, Vol. I: Basic Methods, Allyn and Bacon, Boston, MA.

[18] Nikravesh, P., 1988, Computer-Aided Analysis of Mechanical Systems, Prentice Hall, Englewood Cliffs, NJ.

[19] Holm, D. D., 2008, Geometric Mechanics, Part II: Rotating, Translating, and Rolling, Imperial College Press, London.

[20] Noble, B., and Daniel, J. W., 1977, Applied Linear Algebra, 2nd ed., Prentice-Hall, Englewood, NJ.

[21] Hughes, T. J. R., 1987, The Finite Element Method, Linear Static and Dynamics Finite Element Analysis, Prentice-Hall, Englewood Cliffs, NJ.

[22] Impelluso, T. J., 2016, "WebGL Animations for: A Theoretical and Numerical Study of the Dzhanibekov and Tennis Racket Phenomena," accessed Aug. 11, 2016, http://tinyurl.com/ucsdhib

[23] Rios, O., Ono, T., Murakami, H., and Impelluso, J. T., 2016, "An Analytical and Geometrical Study of the Dzhanibekov and Tennis Racket Phenomena," ASME Paper No. IMECE2016-65570.

CHAPTER 3: MODELING OF RIGID MULTIBODY GYROSCOPIC SYSTEMS

3.1 Introduction to Kinematics of Multibody Systems Using Moving Frames

Before analyzing gyroscopic structures, a quick overview of the moving frame method and its application to multibody systems will be introduced. The previous chapter, which simply analyzed a single rigid body, introduced the basic notation of the moving frame method that will translate to multi-body systems. To begin, as with the tennis racket and wing nut, a body-attached coordinate frame and corresponding vector basis will be defined for each body-α in the system.

The orientation and origin of any rigid body can be defined relative to the inertial frame as shown below:

$$\mathbf{e}^{(\alpha)}(t) = \mathbf{e}^{I} R^{(\alpha)}(t) \quad \text{and} \quad \mathbf{r}_c^{(\alpha)}(t) = \mathbf{e}^{I} x_c^{(\alpha)}(t) \tag{1}$$

where the superscript α identifies a moving body, $R^{(\alpha)}(t)$ denotes a 3×3 rotation matrix, and $x_c^{(\alpha)}(t)$ represents the coordinates to the center of mass of body- α with respect to the inertial frame. Both expressions in Eq. (1) can be placed in a compact 4×4 matrix $E^{(\alpha)}(t)$, the frame connection matrix of body-α, to form a moving frame as shown below in Eq. (2).

$$\left(\mathbf{e}^{(\alpha)}(t) \;\; \mathbf{r}_C^{(\alpha)}(t)\right) = (\mathbf{e}^{I} \quad \mathbf{0}) E^{(\alpha)}(t) = \begin{bmatrix} R^{(\alpha)}(t) & x_C^{(\alpha)}(t) \\ 0_1{}^{T} & 1 \end{bmatrix} \tag{2}$$

where

$$0_1 = \begin{bmatrix} 0 \\ 0 \\ 0 \end{bmatrix} \tag{3}$$

The above compactly represents the orientation and position of a rigid body and clearly states the frame of reference as the inertial frame. Taking the inverse of Eq. (2) allows for the inertial frame to be described relative to the body-α frame.

$$\begin{aligned}(\mathbf{e}^{I} \quad \mathbf{0}) &= \left(\mathbf{e}^{(\alpha)}(t) \;\; \mathbf{r}_C^{(\alpha)}(t)\right)\left(E^{(\alpha)}(t)\right)^{-1} \\ &= \begin{bmatrix}\left(R^{(\alpha)}(t)\right)^{T} & -\left(R^{(\alpha)}(t)\right)^{T} x_C^{(\alpha)}(t) \\ {0_1}^{T} & 1\end{bmatrix}\end{aligned} \tag{4}$$

Similarly, the orientation and origin of the body-$(\alpha+1)$ frame can be defined relative to the origin of the body-α frame as:

$$\begin{aligned}\mathbf{e}^{(\alpha+1)}(t) &= \mathbf{e}^{(\alpha)}(t)R^{(\alpha+1/\alpha)}(t), \\ \mathbf{r}_C^{(\alpha+1)}(t) &= \mathbf{r}_C^{(\alpha)}(t) + \mathbf{e}^{(\alpha)}(t)s_C^{(\alpha+1/\alpha)}(t)\end{aligned} \tag{5}$$

where $s_C^{(\alpha+1/\alpha)}(t)$ represents the relative position vector of the body-$(\alpha+1)$ frame from the body-α frame and $R^{(\alpha+1/\alpha)}(t)$ is the 3×3 rotation matrix relating the body-$(\alpha+1)$ frame to the body-α frame.

Equation (5), as similarly done with Eq. (1), can be written in a 4×4 matrix $E^{(\alpha+1/\alpha)}(t)$, known as the relative frame connection matrix of body-$(\alpha+1)$, shown below in Eq. (6).

$$\begin{aligned}\left(\mathbf{e}^{(\alpha+1)}(t) \;\; \mathbf{r}_C^{(\alpha+1)}(t)\right) &= \left(\mathbf{e}^{(\alpha)}(t) \quad \mathbf{r}_C^{(\alpha)}(t)\right)E^{(\alpha+1/\alpha)}(t) \\ &= \left(\mathbf{e}^{(\alpha)}(t) \quad \mathbf{r}_C^{(\alpha)}(t)\right)\begin{bmatrix}R^{(\alpha+1/\alpha)}(t) & s_C^{(\alpha+1/\alpha)}(t) \\ {0_1}^{T} & 1\end{bmatrix}\end{aligned} \tag{6}$$

Equation (6), with the use of Eq. (2), can easily be expressed with respect to the inertial frame by a simple matrix multiplication of $E^{(\alpha)}(t)E^{(\alpha+1/\alpha)}(t)$ as shown below.

Note in Eq. (7) how the superscripts make the process of relating back to the inertial frame very intuitive as the α terms in the superscripts appear to cancel out.

$$\begin{aligned}\left(\mathbf{e}^{(\alpha+1)}(t)\ \ \mathbf{r}_C^{(\alpha+1)}(t)\right) &= (\mathbf{e}^I \quad \mathbf{0})E^{(\alpha)}(t)E^{(\alpha+1/\alpha)}(t) \\ &= (\mathbf{e}^I \quad \mathbf{0})E^{(\alpha+1)}(t)\end{aligned} \tag{7}$$

Though so far only two bodies have been considered, this can very easily be expanded to analyze a system of connected rigid bodies by simply finding the relative position vectors and relative rotation matrices and building the relative frame connection matrices.

Apart from the compact bookkeeping of orientation and position with respect to any frame of reference, the strength of the moving frame method lies in the systematic derivation of the angular velocity and the velocity vector of the origin. For any frame connection matrix expressed with respect to the inertial frame, the time derivative can be easily performed. Taking the time derivative of Eq. (2) as an example, leads to the following expression:

$$\left(\dot{\mathbf{e}}^{(\alpha)}(t)\ \ \dot{\mathbf{r}}_C^{(\alpha)}(t)\right) = (\mathbf{e}^I \quad \mathbf{0})\dot{E}^{(\alpha)}(t) \tag{8}$$

Using the inverse relationship shown in Eq. (4), the above can be related back to the moving frame:

$$\left(\dot{\mathbf{e}}^{(\alpha)}(t)\ \ \dot{\mathbf{r}}_C^{(\alpha)}(t)\right) = \left(\mathbf{e}^{(\alpha)}(t)\ \ \mathbf{r}_C^{(\alpha)}(t)\right)\left(E^{(\alpha)}(t)\right)^{-1}\dot{E}^{(\alpha)}(t) \tag{9}$$

where $\left(E^{(\alpha)}(t)\right)^{-1}\dot{E}^{(\alpha)}(t) = \Omega^{(\alpha)}(t)$ and is defined as the *time-rate frame-connection matrix*. The submatrices of the rime-rate frame connection matrix can be computed as follows:

$$\Omega^{(\alpha)}(t) = \begin{bmatrix} \overleftrightarrow{\omega^{(\alpha)}(t)} & \left(R^{(\alpha)}(t)\right)^T \dot{x}_c(t) \\ {0_1}^T & 0 \end{bmatrix} \tag{10}$$

Where the skew-symmetric angular velocity matrix, $\overleftrightarrow{\omega^{(\alpha)}(t)}$, can be expressed as shown below:

$$\overleftrightarrow{\omega^{(\alpha)}(t)} = \begin{bmatrix} 0 & -\omega_3^{(\alpha)}(t) & \omega_2^{(\alpha)}(t) \\ \omega_3^{(\alpha)}(t) & 0 & -\omega_1^{(\alpha)}(t) \\ -\omega_2^{(\alpha)}(t) & \omega_1^{(\alpha)}(t) & 0 \end{bmatrix} = \left(R^{(\alpha)}(t)\right)^T \dot{R}^{(\alpha)}(t) \tag{11}$$

From Eq. (10), we note that the angular velocity vector can be obtained from the first column while the velocity vector can be obtained from the second column. When analyzing multiple rigid bodies, as will be done in this chapter, the angular velocity and velocity vectors can thus be obtained by relating the relative connection matrix back to the inertial frame as done with Eq. (7) and then taking the time derivative, or taking the time derivative of Eq. (6) and incorporating the relationship found in Eq. (9). Further detail regarding the use of the moving frame method, specifically the use of the special Euclidean group denoted as SE(3) and the use of lie group theory in multibody kinematics, can be found in related work presented by Murakami [1,2].

3.2 The Gyroscopic Ocean Wave Energy Converter (GOWEC)

3.2.1 GOWEC Introduction

Global attempts to increase generation of clean and reproducible natural energy have greatly contributed to the progress of renewable energy generation. Unlike other renewable energy resources, the ocean remains a relatively untapped source with great potential. The west coast of the United States alone, which includes the coasts of California, Oregon, and Washington, is estimated to have 590 TWh/yr of available wave energy [3].

Unlike solar and wind energy, ocean wave energy is still in its infancy and does not yet have a standard agreed upon design. There are various patents that utilize various ocean induced movements to produce electricity. As examples, point absorbers such as PowerBuoy utilize the vertical or heaving motion while attenuators like Pelamis use the induced movement of its joints [4,5]. Of interest in this section of this chapter is the gyroscopic ocean wave energy converter (GOWEC). The GOWEC is a fully enclosed device able to harness the rocking or pitching motion induced by ocean waves through the use of a gyroscope. It is a novel system that allows for the showcase of the moving frame method and, due to its complete enclosure, may provide a solution to the survivability, noise, and visual pollution challenges faced by other devices.

The basic gyroscopic converter consists of a rotor, a gimbal, and a buoy (or outer gimbal). As the rotor spins at a high angular velocity and the buoy is excited by an incoming wave, a gyroscopic moment is created on the inner gimbal causing it to rotate. This rotation is then transmitted through a gearbox to an electric generator, which produces electricity. A few inventions, simulations, and experiments have been conducted that use the basic gyroscopic principles to harness energy from the ocean. Aaron Goldin demonstrated a small scale on land single gyroscopic converter prototype at a Siemens Westinghouse competition while Bracco et al. developed numerical simulations and performed water tank tests of a single gyroscopic system [6-8]. H. Kanki built full-scale models of gyroscopic ocean wave energy converters that were able to capture 20kW in 2006 and 50kW in 2012 off the coast of Japan [9]. However, despite the recent numerical and experimental work, the theoretical modeling of gyroscopic ocean wave energy converters is still in the preliminary stages compared to other converters.

The objective of this section in this chapter is thus to produce a detailed mathematical model of the general system and approximate the power output using off-the-shelf gyroscope units. While Townsend et al. have derived the gyroscopic equations of motion in previous work through the use of quaternions [10], the research presented in this paper takes a different approach by explicitly writing the frame of reference and by using rotation matrices and the group theory associated with rotation matrices (S0(3)) and the SE(3) group [1,2,11]. Through the use of the moving frame method [1,2], a systematic approach is developed to obtain the equations of motion that aids in optimizing the power output and in understanding the roles of key converter parameters. The analysis begins by developing the kinematics and kinetics of the system shown in Fig. 1 to derive the equations of motion. Using the derived equations of motion, an expression for the maximum average power output is obtained that will then be used to evaluate the use of off-the-shelf gyroscopic stabilizer systems developed by Seakeeper Inc.

3.2.2 Ocean Wave Energy and Power

Most of the wave energy generated by wind is contained in the period interval from 5s to 15s. The wave energy and power are obtained by using linearized gravity-wave theory [12, 13] assuming small amplitude compared to wave length. In Fig. 1, harmonic water wave with amplitude a, wave length λ, and period T is shown with respect to the undisturbed water surface $x_3 = 0$ using an inertial coordinate system $\{x_1, x_2, x_3\}$. The bottom surface is located at $x_3 = -D$. A harmonic wave profile propagating in the x_2-direction is written as:

$$\eta(x_2, t) = a * \cos\left(2\pi\left(\frac{x_2}{\lambda} - \frac{t}{T}\right)\right) \tag{12}$$

The wave number k is expressed by the wave length λ as: $k = 2\pi/\lambda$ and wave angular velocity $\omega^{(w)} = 2\pi/T$, where superscript (w) denotes that the angular velocity is of the ocean wave in order to distinguish it from the angular velocities of generator components: buoy, gimbal, and rotor.

A straightforward analysis [12, 13] shows that waves are dispersive: the wave speed changes depending on wave length λ. The phase velocity c_p of waves is

$$c_p = \frac{\omega^{(w)}}{k} = \sqrt{\frac{g\lambda}{2\pi}\tanh\left(\frac{2\pi D}{\lambda}\right)} \tag{13}$$

For deep water waves, $\lambda/D \ll 1$, $c_p = (g\lambda/2\pi)^{1/2}$. We find $c_p = gT/2\pi$ using $\lambda = c_p T$. Equation (13) indicates that waves with longer wavelength travel faster.

A general wave consists of a set of simple harmonic components with different wave lengths. Such waves travel in wave packets with the carrier wave traveling with the phase velocity c_p and the modulation traveling with the group velocity c_g:

$$c_g = \frac{d\omega^{(w)}}{dk} = \frac{c_p}{2}\left(1 + \frac{2kD}{\sinh(2kD)}\right) \tag{14}$$

The energy propagates at the speed of the group velocity.

The energy E of a simple sinusoidal wave motion in Eq. (12), consists of equal amount of kinetic energy E_k and potential energy E_p. The total energy per unit horizontal area in the unit of J/m^2 is

$$E = E_k + E_p = \rho g a^2/2 \tag{15}$$

where $\rho = 1020\ \mathrm{kg/m^3}$ is mass density of sea water and $g = 9.81\mathrm{m/s^2}$ represents the gravitation acceleration.

The same energy formula is used for non-periodic or random waves, which are characterized by *significant wave height* H_s by using the conversion relation:

$$a = H_s/2\sqrt{2} \tag{16}$$

The significant wave height statistically describes the distribution of ocean wave height. The forecast for significant wave height along the Pacific coast and the Atlantic coast are provided by Ocean Prediction Center [14].

By using the significant wave height, the wave energy per unit horizontal area is expressed as:

$$E = \frac{\rho g H_s^2}{16} \tag{17}$$

The power across the vertical plane $x_2 = 0$ per meter of wave crest is expressed in terms of the wave number k, the phase velocity c_p and the group velocity c_g as:

$$P = Ec_g = E\frac{c_p}{2}\left(1 + \frac{2kD}{\sinh(2kD)}\right) \tag{18}$$

For deep water wave, $\lambda/D \ll 1$, the group velocity becomes $c_g = \frac{c_p}{2} = gT/4\pi$, and the power per meter of wave crest simplifies as:

$$P = \frac{\rho g^2}{64\pi} H_s^2 T = 0.48 H_s^2 T \text{ kW/m} \tag{19}$$

Along the central and northern California coast and the Oregon coast as well as the Atlantic coast there are many locations where P is greater than 5 kW/m [15].

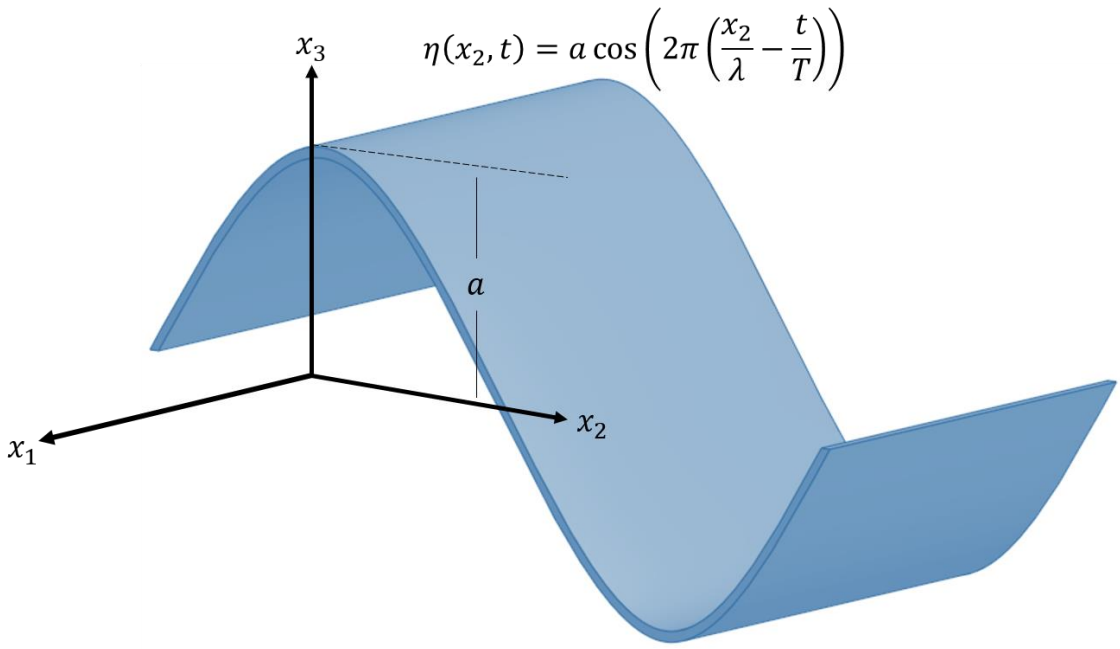

Figure 3-1: Harmonic ocean wave propagating along the x_2-direction

3.2.3 Kinematics of the System

The model GOWEC to be analyzed in this paper is shown in Fig. 2. It consists of a dual gyroscopic configuration to cancel the reactionary moments known to arise when just a single gyroscope is installed. Due to the symmetry of the design and to avoid repetitive derivations, the system will be analyzed with only the left gyroscope in place. As the derivation is completed, we will simply keep in mind that the power output obtained will only account for half of the total produced. The system thus has three major components as noted by the bubble callouts in Fig. 2. They include: (1) the buoy (including the generator and power transmission), (2) the gimbal (including the motor and the counterweight), and (3) the rotor. The kinematic analysis, using the moving frame method is presented in the proceeding sections.

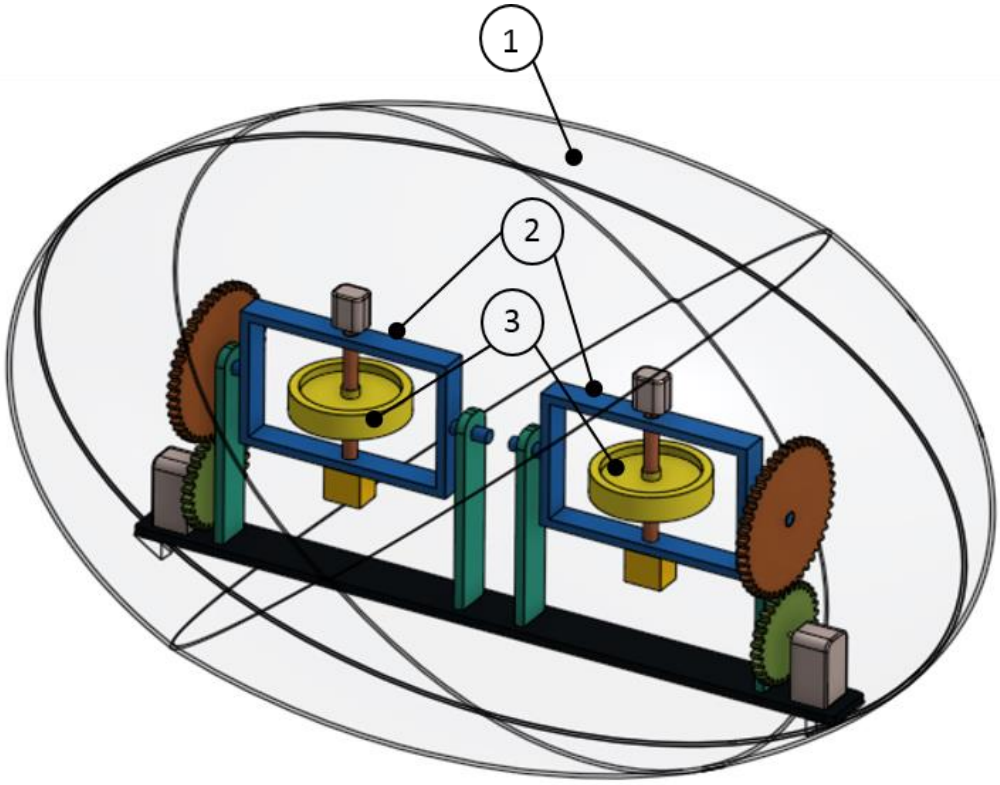

Figure 3-2: Model system of a gyroscopic ocean wave energy converter demonstrating the major components: 1) buoy, 2) inner gimbal, and 3) rotor

3.2.3.1 Inertial Frame

The kinematics section begins by establishing the inertial coordinate system $\{x_1 \ x_2 \ x_3\}$, where $x_3 = 0$ denotes undisturbed ocean waves. The unit tangent vectors to the coordinate axes define the inertial frame, denoted by $\mathbf{e}^I$.

$$\mathbf{e}^I = (\mathbf{e}_1^I \quad \mathbf{e}_2^I \quad \mathbf{e}_3^I) \tag{20}$$

The inertial frame remains fixed and thus has no time derivative, $\dot{\mathbf{e}}^I = 0$. To differentiate between the inertial and the coordinate frames to be defined, a superscript I will be used. Furthermore, a bolded typeface from now on will indicate a vector representation.

3.2.3.2 Buoy Connection and Time Rate Connection Matrices

The first component of the GOWEC to be analyzed will be the buoy. As a standard approach of the moving frame method, we begin with the outermost component of the system. A coordinate system $\left\{s_1^{(1)}\ s_2^{(1)}\ s_3^{(1)}\right\}$ along with a coordinate frame $\mathbf{e}^{(1)}(t) = \left(\mathbf{e}_1^{(1)}(t)\ \mathbf{e}_2^{(1)}(t)\ \mathbf{e}_3^{(1)}(t)\right)$ is established and attached at the center of mass of the buoy. Thus as the buoy moves and rotates, so does the coordinate or moving frame. To compactly express the position and orientation of the buoy with respect to the inertial frame, a 4×4 buoy frame connection matrix, $E^{(1)}(t)$, is developed:

$$\left(\mathbf{e}^{(1)}(t) \quad \mathbf{r}_c^{(1)}(t)\right) = (\mathbf{e}^I \quad \mathbf{0})E^{(1)}(t) = (\mathbf{e}^I \quad \mathbf{0})\begin{bmatrix} R^{(1)}(t) & x_c^{(1)}(t) \\ 0_1{}^T & 1 \end{bmatrix}, \tag{21}$$

where $R^{(1)}(t)$ is a rotation matrix, $x_c^{(1)}(t)$ is a 3×1 vector containing the components of the position vector, and $0_1^T = [0\ \ 0\ \ 0]$. Note that the orientation and position of the buoy are in the first and second columns of $E^{(1)}(t)$ respectively. At this moment, the rotation matrix of the buoy will not be prescribed and will be considered an arbitrary rotation matrix. In a later section, we will prescribe the buoy motion to ease the derivation of the power output expression. Frame connection matrices allow one to easily calculate both the velocity and angular velocity vectors. Taking the time derivative of Eq. (21) and expressing the result with the buoy frame itself using the inverse of Eq. (21), results in the time-rate of the buoy frame connection matrix $\Omega^{(1)}(t)$:

$$\left(\dot{\mathbf{e}}^{(1)}(t) \quad \dot{\mathbf{r}}_c^{(1)}(t)\right) = \left(\mathbf{e}^{(1)}(t) \quad \mathbf{r}_c^{(1)}(t)\right)\Omega^{(1)}(t), \tag{22}$$

where $\Omega^{(1)}(t)$ is expressed below in Eq. (23)

$$\Omega^{(1)}(t) = \begin{bmatrix} \overleftrightarrow{\omega^{(1)}(t)} & \left(R^{(1)}(t)\right)^T \dot{x}_C^{(1)}(t) \\ 0_1^T & 0 \end{bmatrix}. \tag{23}$$

The time-rate of the buoy frame connection matrix contains both the angular velocity and velocity vectors in columns one and two, respectively. The velocity vector of the buoy can be expressed, as shown in Eq. (24) below, with respect to the inertial frame by observing the second column above. To be noted, since the velocity vector with respect to the inertial frame is needed, the rotation matrix $\left(R^{(1)}(t)\right)^T$, which expresses the vector with a buoy frame of reference, is not needed. The second column thus gives the velocity vector of the buoy as below:

$$\dot{\mathbf{r}}_C^{(1)}(t) = \mathbf{e}^I \dot{x}_C^{(1)}(t). \tag{24}$$

The first column contains the skew symmetric angular velocity matrix $\overleftrightarrow{\omega^{(1)}(t)}$, which can be expressed through rotation matrices as follows:

$$\overleftrightarrow{\omega^{(1)}(t)} = \left(R^{(1)}(t)\right)^T \dot{R}^{(1)}(t). \tag{25}$$

The skew symmetric angular velocity matrix is used to express the time-rate of the buoy coordinate frame with respect to its own frame:

$$\dot{\mathbf{e}}^{(1)}(t) = \mathbf{e}^{(1)}(t)\, \overleftrightarrow{\omega^{(1)}(t)} = \mathbf{e}^{(1)}(t) \begin{bmatrix} 0 & -\omega_3^{(1)} & \omega_2^{(1)} \\ \omega_3^{(1)} & 0 & -\omega_1^{(1)} \\ -\omega_2^{(1)} & \omega_1^{(1)} & 0 \end{bmatrix}, \tag{26}$$

and directly leads to the construction of the angular velocity vector for the buoy as shown below.

$$\boldsymbol{\omega}^{(1)}(t) = \mathbf{e}^{(1)}(t)\omega^{(1)}(t) \tag{27}$$

3.2.3.3 Gimbal Connection and Time-Rate Connection Matrices

The kinematics of the gimbal follows a similar procedure to that of the buoy. Once again, a coordinate system $\left\{s_1^{(2)}\ s_2^{(2)}\ s_3^{(2)}\right\}$, and a coordinate frame $\mathbf{e}^{(2)}(t) = \left(\mathbf{e}_1^{(2)}(t)\ \mathbf{e}_2^{(2)}(t)\ \mathbf{e}_3^{(2)}(t)\right)$, are established at the center of mass of the gimbal. To describe the orientation and translational motion of the gimbal, the relative connection matrix will be derived relative to the buoy's moving frame.

To describe the translational motion of the center of mass of the gimbal from the center of mass of the buoy, a relative position vector $\boldsymbol{s}_c^{(2/1)}(t)$ is needed. It is now noted, staying consistent with the notation presented by H. Murakami, that $\boldsymbol{s}_c(t)$ will be reserved for relative position vectors and the partitioned superscript will indicate the two frames and bodies involved [1,2]. For our particular case, we are expressing the gimbal with respect to the buoy frame and thus we have expressed the superscript as (2/1). The relative position vector will allow for the modeling of the GOWEC with a gyroscope anywhere within the buoy, and not just at the center of mass. We further note that the distance between the buoy and gimbal frame remains constant (only if the gimbal is rotating around an axis that intersects its center of mass) which allows the relative position vector to be expressed as:

$$\boldsymbol{s}_c^{(2/1)}(t) = \mathbf{e}^{(1)}(t)\begin{pmatrix} h_1^{(2/1)} \\ h_2^{(2/1)} \\ h_3^{(2/1)} \end{pmatrix} = \mathbf{e}^{(1)}(t)s_c^{(2/1)}, \tag{28}$$

where $h_i^{(2/1)}$ for $i = 1,2,3$, are fixed distances, or constants, from the buoy's center of mass to the gimbal's center of mass.

Next, the relative orientation is derived through the use of rotation matrices. The gimbal frame can be expressed relative to the buoy frame as follows:

$$\mathbf{e}^{(2)}(t) = \mathbf{e}^{(1)}(t)R^{(2/1)}(t), \tag{29}$$

where $R^{(2/1)}(t)$ is an elementary rotation matrix as shown below:

$$R^{(2/1)}(t) = {R_2}^{(2/1)}\left(\varphi^{(2)}(t)\right) =$$

$$\begin{bmatrix} \cos\left(\varphi^{(2)}(t)\right) & 0 & \sin\left(\varphi^{(2)}(t)\right) \\ 0 & 1 & 0 \\ -\sin\left(\varphi^{(2)}(t)\right) & 0 & \cos\left(\varphi^{(2)}(t)\right) \end{bmatrix}. \tag{30}$$

The superscript in the rotation matrix, as shown with the relative position vectors, denotes that the rotation for the gimbal is with respect to the buoy frame. In this particular case, as can be seen from Fig. 2, the gimbal is forced to rotate with respect to its $\mathbf{e}_2^{(2)}(t)$ axis, noted by the subscript of the rotation matrix.

With the relative position and orientation now defined, the relative connection matrix $E^{(2/1)}(t)$ may now be expressed with respect to the buoy moving frame. The relationship between the gimbal frame and the buoy frame is expressed below:

$$\left(\mathbf{e}^{(2)}(t) \quad \mathbf{r}_c^{(2)}(t)\right) = \left(\mathbf{e}^{(1)}(t) \quad \mathbf{r}_c^{(1)}(t)\right) E^{(2/1)}(t), \tag{31}$$

where $E^{(2/1)}(t)$ is expressed as the following combination of submatrices:

$$E^{(2/1)}(t) = \begin{bmatrix} {R_2}^{(2/1)}\left(\varphi^{(2)}(t)\right) & s_c^{(2/1)} \\ {0_1}^T & 1 \end{bmatrix}. \tag{32}$$

To express the position and orientation of the gimbal frame with respect to the inertial frame, only a simple substitution for $\left(\mathbf{e}^{(1)}(t) \quad \mathbf{r}_c^{(1)}(t)\right)$ using Eq. (21) is needed. Equation (31) thus leads to Eq. (33) below:

$$\left(\mathbf{e}^{(2)}(t) \quad \mathbf{r}_c^{(2)}(t)\right) = (\mathbf{e}^I \quad \mathbf{0})E^{(1)}(t)E^{(2/1)}(t) = (\mathbf{e}^I \quad \mathbf{0})E^{(2)}(t), \tag{33}$$

where $E^{(2)}(t)$, after performing the matrix multiplication $E^{(1)}(t)E^{(2/1)}(t)$, is defined below.

$$E^{(2)}(t) = \begin{bmatrix} R^{(1)}(t){R_2}^{(2/1)}\left(\varphi^{(2)}(t)\right) & R^{(1)}(t)s_C^{(2/1)} + x_C^{(1)}(t) \\ {0_1}^T & 1 \end{bmatrix}. \tag{34}$$

To obtain the velocity and angular velocity vectors of the gimbal frame, the time derivative of Eq. (33) is taken, resulting in the time rate of the connection matrix $\Omega^{(2)}(t)$:

$$\left(\dot{\mathbf{e}}^{(2)}(t) \quad \dot{\mathbf{r}}_c^{(2)}(t)\right) = \left(\mathbf{e}^{(2)}(t) \quad \mathbf{r}_c^{(2)}(t)\right)\Omega^{(2)}(t), \tag{35}$$

To note, the time derivative of Eq. (31) can just as easily be taken to obtain the same result shown in Eq. (35), but the time rate of the buoy frame needs to be considered. The above $\Omega^{(2)}(t)$ matrix contains the velocity and angular velocity vectors of the gimbal with respect to the gimbal frame. The velocity vector of the gimbal is located in the rightmost column of $\Omega^{(2)}(t)$. Expressing the velocity vector with respect to the inertial coordinate frame results in the following:

$$\dot{x}_c^{(2)}(t) = R^{(1)}(t)\left(\overleftrightarrow{s_C^{(2/1)}}\right)^T \omega^{(1)}(t) + \dot{x}_c^{(1)}(t). \tag{36}$$

The first column of $\Omega^{(2)}(t)$ contains the skew symmetric angular velocity matrix $\overleftrightarrow{\omega^{(2)}(t)}$ from which, once again, the angular velocity vector can be easily obtained as shown in Eq. (37)

$$\omega^{(2)}(t) = \left({R_2}^{(2/1)}\left(\varphi^{(2)}(t)\right)\right)^T \omega^{(1)}(t) + \dot{\varphi}^{(2)}\mathrm{e}_2 \tag{37}$$

In the above expression, e_2 is a unit column vector expressed as $[0 \;\; 1 \;\; 0]^T$.

3.2.3.4 Rotor Connection and Time-Rate Connection Matrices

The last component to be analyzed is the rotor housed within the gimbal. Similar to the previous components of the GOWEC, the kinematic analysis begins by establishing the coordinate system $\left\{s_1^{(3)}\ s_2^{(3)}\ s_3^{(3)}\right\}$, and coordinate frame $\mathbf{e}^{(3)}(t) = \left(\mathbf{e}_1^{(3)}(t)\ \mathbf{e}_2^{(3)}(t)\ \mathbf{e}_3^{(3)}(t)\right)$, at the center of mass.

To assemble the rotor frame connection matrix, the rotor relative position vector is defined with respect to the gimbal frame. Noting from Fig. 2 that both the gimbal's and rotor's center of masses coincide, the relative position vector $\boldsymbol{s}_c^{(3/2)}(t)$ is simply a zero vector. Lastly, the relative orientation of the rotor is derived. The rotor frame is defined below relative to the gimbal through the use of a rotation matrix:

$$\mathbf{e}^{(3)}(t) = \mathbf{e}^{(2)}(t)R^{(3/2)}(t), \tag{38}$$

where $R^{(3/2)}(t)$ can once again be expressed as an elementary rotation matrix below.

$$R^{(3/2)}(t) = {R_3}^{(3/2)}\left(\psi^{(3)}(t)\right)$$

$$= \begin{bmatrix} \cos\left(\psi^{(3)}(t)\right) & -\sin\left(\psi^{(3)}(t)\right) & 0 \\ \sin\left(\psi^{(3)}(t)\right) & \cos\left(\psi^{(3)}(t)\right) & 0 \\ 0 & 0 & 1 \end{bmatrix} \tag{39}$$

The subscript indicates the rotor's axis of rotation is along the $\mathbf{e}_3^{(3)}$ axis. The rotor relative connectivity matrix $E^{(3/2)}(t)$ can now be assembled:

$$\left(\mathbf{e}^{(3)}(t) \quad \mathbf{r}_c^{(3)}(t)\right) = \left(\mathbf{e}^{(2)}(t) \quad \mathbf{r}_c^{(2)}(t)\right) E^{(3/2)}(t), \tag{40}$$

where $E^{(3/2)}(t)$ is expressed below

$$E^{(3/2)}(t) = \begin{bmatrix} {R_3}^{(3/2)}\left(\psi^{(3)}(t)\right) & 0_1 \\ {0_1}^T & 1 \end{bmatrix}. \tag{41}$$

Obtaining the rotor frame connection matrix $E^{(3)}(t)$ simply requires Eq. (33) to express it with respect to the inertial frame observer:

$$\left(\mathbf{e}^{(3)}(t) \quad \mathbf{r}_c^{(3)}(t)\right) = (\mathbf{e}^I \quad \mathbf{0})E^{(3)}(t) = (\mathbf{e}^I \quad \mathbf{0})E^{(2)}(t)E^{(3/2)}(t), \tag{42}$$

where $E^{(3)}(t)$ is expressed below

$$E^{(3)}(t) = \begin{bmatrix} R^{(1)}(t)R_2^{(2/1)}\left(\varphi^{(2)}(t)\right)R_3^{(3/2)}\left(\psi^{(3)}(t)\right) & R^{(1)}(t)s_C^{(2/1)} + x_C^{(1)}(t) \\ {0_1}^T & 1 \end{bmatrix}. \tag{43}$$

Taking the time derivative of Eq. (42) and relating back to the corresponding frame, results in the time rate of the rotor frame connection matrix, $\Omega^{(3)}(t)$.

$$\left(\dot{\mathbf{e}}^{(3)}(t) \quad \dot{\mathbf{r}}_c^{(3)}(t)\right) = \left(\mathbf{e}^{(3)}(t) \quad \mathbf{r}_c^{(3)}(t)\right)\Omega^{(3)}(t) \tag{44}$$

Once again, the first column of $\Omega^{(3)}(t)$ contains the skew symmetric angular velocity matrix $\overleftrightarrow{\omega^{(3)}(t)}$ from which the angular velocity vector can be obtained:

$$\omega^{(3)}(t) = \left(R^{(3/1)}(t)\right)^T + \left(R_3^{(3/2)}\left(\psi^{(3)}(t)\right)\right)^T \dot{\varphi}^{(2)}(t)\mathrm{e}_2 + \dot{\psi}^{(3)}\mathrm{e}_3, \tag{45}$$

where $R^{(3/1)}(t)$ is expressed as the sequence of rotations below:

$$R^{(3/1)}(t) = R_2^{(2/1)}\left(\varphi^{(2)}(t)\right)R_3^{(3/2)}\left(\psi^{(3)}(t)\right). \tag{46}$$

Similar to the e_2 column vector, e_3 is expressed as $[0 \;\; 0 \;\; 1]^T$. The second column contains the rotor velocity vector, which can be expressed with respect to the inertial frame for use in the upcoming kinetics section.

$$\dot{x}^{(3)}(t) = \dot{x}_C^{(1)}(t) + R^{(1)}(t)\left(\overleftarrow{s_C^{(2/1)}}\right)^T \omega^{(1)}(t) \tag{47}$$

Note that the velocity of both the rotor and gimbal are the same, since their center of masses coincide at all times.

3.2.4 Generalized Velocities

Due to the symmetry of the system, only three components corresponding to the buoy and left gyroscope were analyzed in the above kinematics section. Collectively, the velocity vectors of the three components can be expressed in an 18×1 column matrix, $\{\dot{X}(t)\}$, referred to as the *generalized velocities* vector. The generalized velocities can be expressed by a set of independent velocities referred to as the *essential generalized velocities*, assembled in an 8×1 column matrix $\{\dot{X}^*(t)\}$.

$$\{\dot{X}(t)\} = \begin{pmatrix} \dot{x}_c^{(1)} \\ \omega^{(1)} \\ \dot{x}_c^{(2)} \\ \omega^{(2)} \\ \dot{x}_c^{(3)} \\ \omega^{(3)} \end{pmatrix}, \quad \{\dot{X}^*(t)\} = \begin{pmatrix} \dot{x}_c^{(1)} \\ \omega^{(1)} \\ \dot{\varphi}^{(2)} \\ \dot{\psi}^{(3)} \end{pmatrix} \tag{48}$$

The generalized velocities are linearly related to the essential generalized velocities through the following expression:

$$\{\dot{X}(t)\} = [B(t)]\{\dot{X}^*(t)\}, \tag{49}$$

where $[B(t)]$ is an 18×8 matrix shown in Eq. (50). This relationship removes the extraneous or constrained components of the velocity vectors and simplifies the number of equations of motion.

$$[B(t)]$$

$$= \begin{bmatrix} I_3 & 0_3 & 0_1 & 0_1 \\ 0_3 & I_3 & 0_1 & 0_1 \\ I_3 & R^{(1)}(t)\left(\overleftrightarrow{s_c^{(2/1)}}\right)^T & 0_1 & 0_1 \\ 0_3 & \left(R_2^{(2/1)}(t)\left(\varphi^{(2)}(t)\right)\right)^T & \mathrm{e}_2 & 0_1 \\ I_3 & R^{(1)}(t)\left(\overleftrightarrow{s_c^{(2/1)}}\right)^T & 0_1 & 0_1 \\ 0_3 & \left(R^{(3/1)}(t)\right)^T & \left(R_3^{(3/2)}\left(\psi^{(3)}(t)\right)\right)^T \mathrm{e}_2 & \mathrm{e}_3 \end{bmatrix} \tag{50}$$

In the above, $0_3$and I_3 represent a 3×3 zero and identity matrix respectively. The derivation of the $[B(t)]$ matrix is the final step of the kinematics section.

3.2.5 Kinetics of the System

In this section, the framework to assemble the equations of motion of the GOWEC will be presented. Through the use of Hamilton's principle, the principle of virtual work will be obtained from which the equations of motion can be derived.

3.2.5.1 The Principle of Virtual Work

To obtain the principle of virtual work, and the resulting equations of motion, Hamilton's principle shown in Eq. (51) will be utilized.

$$\int_{t_0}^{t_1} \left(\delta\hat{L}^{(\alpha)}(t) + \delta W^{(\alpha)}(t)\right) dt \tag{51}$$

Before taking the variation, one must first define the Lagrangian $\hat{L}$ and the work by non-conservative forces. The Lagrangian is expressed as the difference between the kinetic energy K and the potential energy U as shown in Eq. (52).

$$\hat{L} = K - U \tag{52}$$

The total kinetic energy of the system includes both the translational and rotational kinetic energy of each body-α. Therefore, expressions for the linear momentum $\boldsymbol{L}_C^{(\alpha)}$, expressed with the inertial frame, and angular momentum $\boldsymbol{H}_C^{(\alpha)}$, expressed with the moving frame, are needed.

$$\boldsymbol{L}_C^{(\alpha)} = \mathbf{e}^I L_C^{(\alpha)} = \mathbf{e}^I m^\alpha \dot{x}_C^{(\alpha)} \tag{53}$$

$$\boldsymbol{H}_C^{(\alpha)} = \mathbf{e}^{(\alpha)} H_C^{(\alpha)} = \mathbf{e}^{(\alpha)} J_C^{(\alpha)} \omega^{(\alpha)} \tag{54}$$

The total kinetic energy can be compactly expressed in matrix form as:

$$K = \frac{1}{2}\{\dot{X}\}^T\{H\} = \frac{1}{2}\{\dot{X}\}^T[M]\{\dot{X}\}, \tag{55}$$

where $\{H\}$ contains both the linear and angular momenta in a column matrix and $[M]$ is the mass matrix containing both the masses and mass moments of inertia of the bodies in the system expressed in Eq. (56). Since the coordinate systems were placed to coincide with the principle axes, the mass matrix $[M]$ is an 18×18 diagonal matrix.

$$[M] = \begin{bmatrix} m^{(1)}I_3 & 0_3 & 0_3 & 0_3 & 0_3 & 0_3 \\ 0_3 & J_C^{(1)} & 0_3 & 0_3 & 0_3 & 0_3 \\ 0_3 & 0_3 & m^{(2)}I_3 & 0_3 & 0_3 & 0_3 \\ 0_3 & 0_3 & 0_3 & J_C^{(2)} & 0_3 & 0_3 \\ 0_3 & 0_3 & 0_3 & 0_3 & m^{(3)}I_3 & 0_3 \\ 0_3 & 0_3 & 0_3 & 0_3 & 0_3 & J_C^{(3)} \end{bmatrix} \tag{56}$$

The potential energy U of each component will be solely due to the gravitational acceleration.

$$U^{(\alpha)} = m^{(\alpha)} g x_{3C}^{(\alpha)} \tag{57}$$

The generalized forces and moments acting on the system will now be defined in a column matrix $\{Q(t)\}$ shown in Eq. (58). The moments and forces acting on the system

are those due to the ocean waves while the actuator couples are due to the motors powering the rotor and the generators connected to the output shaft of the gimbal. The actuator couples and forces are factored in due to Newton's third law of action and reaction. Contributions from the gravitational potential energy will also be expressed in the $\{Q(t)\}$ column matrix.

$$\{Q(t)\} = \begin{pmatrix} F_c^{(1)I}(t) \\ M_c^{(1)}(t) \\ F_c^{(2)I}(t) \\ M_c^{(2)}(t) \\ F_c^{(3)I}(t) \\ M_c^{(3)}(t) \end{pmatrix} = \begin{pmatrix} F^{(w)I}(t) + F_b^I - m^{(1)} g \mathrm{e}_3 \\ M^{(w)}(t) - M^{(g)}(t)\mathrm{e}_2 + M^{(g)}(t)\mathrm{e}_2 \\ -m^{(2)} g \mathrm{e}_3 \\ -M^{(r)}(t) + M^{(g)}(t)\mathrm{e}_2 \\ -m^{(3)} g \mathrm{e}_3 \\ M^{(r)}{}_m(t)\mathrm{e}_3 \end{pmatrix} \tag{58}$$

In the above $\{Q(t)\}$ expression, the superscript I indicates that the components of the forces are with respect to the inertial frame. $F^{(w)I}(t)$ and $M^{(w)}(t)$ are the wave forces and couples acting on the buoy, respectively, and F_b^I is the constant buoyancy force expressed in Eq. (59).

$$F_b^I = \left(m^{(1)} + m^{(2)} + m^{(3)} + m^{(4)} + m^{(5)}\right) g \mathrm{e}_3 \tag{59}$$

The action and reaction couples $M^{(r)}(t)$ and $M^{(g)}(t)$ are due to the motor powering the rotor and the generator, respectively. The major advantage of a double gyro configuration, as previously stated, is the ability to cancel the reactionary moment. To do so, the rotors are simply spun in opposite directions. The left rotor is spun with respect to the positive $\mathbf{e}_3^{(3)}$ axis while the right rotor is spun about the negative $\mathbf{e}_3^{(5)}$ axis.

To obtain the principal of virtual work from Hamilton's principle, the variation of the Lagrangian is needed. The variation of a moving frame attached to each body of the

system is obtained in a single step by taking the variation of the connection matrices. Listed below is the general matrix expression, $\delta\Pi$, for the variation of a connection matrix [1,2].

$$\delta\Pi = \begin{bmatrix} \overleftrightarrow{\delta\pi^{(\alpha)}(t)} & \left(R^{(\alpha)}(t)\right)^T \delta x_C^{(\alpha)}(t) \\ 0_1^T & 0 \end{bmatrix} \tag{60}$$

From $\delta\Pi$, the virtual generalized displacements can be obtained, where the virtual rotational displacement $\overleftrightarrow{\delta\pi^{(\alpha)}(t)}$ is defined for body-α below.

$$\overleftrightarrow{\delta\pi^{(\alpha)}(t)} = \left(R^{\alpha}(t)\right)^T \delta R^{(\alpha)}(t) \tag{61}$$

In order to take the variation of the Lagrangian, the virtual generalized displacements are assembled in an 18×1 column matrix $\{\delta\tilde{X}\}$.

$$\{\delta\tilde{X}\} = \begin{pmatrix} \delta x_C^{(1)} \\ \delta\pi^{(1)} \\ \delta x_C^{(2)} \\ \delta\pi^{(2)} \\ \delta x_C^{(3)} \\ \delta\pi^{(3)} \end{pmatrix} \tag{62}$$

Imposing the commutativity of the time differentiation, d/dt-operator, and the variation of the frame, δ-operator, results in the variation of the generalized velocities shown in Eqs. (63a) and (63b) below [2,16].

$$\delta\omega^{(\alpha)}(t) = \frac{d}{dt}\delta\pi^{(\alpha)}(t) + \overleftrightarrow{\omega^{(\alpha)}(t)}\delta\pi^{(\alpha)}(t) \tag{63a}$$

$$\frac{d}{dt}\delta x_C^{(\alpha)}(t) = \delta\dot{x}_C^{(\alpha)}(t) \tag{63b}$$

Placing Eqs. (63a) and (63b) in matrix form for use in the variation of the Lagrangian results in the compact expression for the variation of the generalized velocities:

$$\{\delta\dot{X}\} = \left\{\delta\dot{\tilde{X}}\right\} + [D]\{\delta\tilde{X}\}, \tag{64}$$

where the skew symmetric matrix $[D]$ is shown below:

$$[D] = \begin{bmatrix} 0_3 & 0_3 & 0_3 & 0_3 & 0_3 & 0_3 \\ 0_3 & \overleftrightarrow{\omega^{(1)}(t)} & 0_3 & 0_3 & 0_3 & 0_3 \\ 0_3 & 0_3 & 0_3 & 0_3 & 0_3 & 0_3 \\ 0_3 & 0_3 & 0_3 & \overleftrightarrow{\omega^{(2)}(t)} & 0_3 & 0_3 \\ 0_3 & 0_3 & 0_3 & 0_3 & 0_3 & 0_3 \\ 0_3 & 0_3 & 0_3 & 0_3 & 0_3 & \overleftrightarrow{\omega^{(3)}(t)} \end{bmatrix} \tag{65}$$

The variation of the Lagrangian can thus be compactly expressed as shown in Eq. (66), where $\{G\}$ is the 18×1 gravitational force column matrix.

$$\delta L = \left\{\delta\dot{X}\right\}^T [M]\left\{\dot{X}\right\} - \{\delta\tilde{X}\}^T\{G\} \tag{66}$$

Lastly, the virtual work done by the generalized forces, $\{Q(t)\}$, which as stated earlier includes the gravitation force column matrix, is expressed as:

$$\delta W = \{\delta\tilde{X}\}^T\{Q(t)\} \tag{67}$$

Hamilton's principle can now be expressed using Eqs. (66) and (67) as:

$$\int_{t_0}^{t_1} \left\{\delta\dot{\tilde{X}}\right\}^T \{H\} + \{\delta\tilde{X}\}^T ([D]^T\{H\} + \{Q(t)\})dt = 0 \tag{68}$$

Integrating by parts, and noting that the virtual displacements vanish at t_0 and t_1, yields the principle of virtual work that holds for all time:

$$\{\delta\tilde{X}\}^T\left[\left\{\dot{H}(t)\right\} + [D]\{H(t)\} - \{Q(t)\}\right]. \tag{69}$$

3.2.5.2 Equations of Motion

Using the principal of virtual work, shown in Eq. (69), the equations of motion can be derived. To simplify the analysis and the number of equations, the essential virtual displacements $\{\delta\tilde{X}^*\}$, are introduced in place of the virtual displacements:

$$\{\delta\tilde{X}^*\} = \begin{pmatrix} \delta x_C^{(1)} \\ \delta\pi^{(1)} \\ \delta\varphi^{(2)} \\ \delta\psi^{(3)} \end{pmatrix}. \tag{70}$$

As with the generalized velocities in Eq. (49), the same $[B(t)]$ matrix relates the virtual generalized displacements $\{\delta\tilde{X}\}$ and the essential virtual displacements $\{\delta\tilde{X}^*\}$.

$$\{\delta\tilde{X}\} = [B(t)]\{\delta\tilde{X}^*\} \tag{71}$$

The angular momenta derived in Eq. (55), can be written with respect to the essential generalized velocities:

$$\{H(t)\} = [M][B(t)]\{\dot{X}^*(t)\}. \tag{72}$$

Substituting Eqs. (72) and (71) back into the principal of virtual work, Eq. (69), results in Eq. (73) below.

$$\begin{gathered} \{\delta\tilde{X}^*\}^T([B(t)]^T[M][B(t)]\{\ddot{X}^*\} + \\ [B(t)]^T\left([M]\left[\dot{B}(t)\right] + [D(t)][M][B(t)]\right)\{\dot{X}^*(t)\} - \\ [B(t)]^T\{Q(t)\}) = \{0\} \end{gathered} \tag{73}$$

Equation (73) is the general formula, in matrix form, needed to obtain the equations of motion in terms of the essential generalized velocities. It can be rewritten in a more compact form as seen below in Eq. (74):

$$[M^*]\{\ddot{X}^*\} + [N^*]\{\dot{X}^*(t)\} - \{F^*\} = 0, \tag{74}$$

where the matrices are defined as follows:

$$[M^*] = [B(t)]^T[M][B(t)] \tag{75a}$$

$$[N^*] = [B(t)]^T\left([M]\left[\dot{B}(t)\right] + [D(t)][M][B(t)]\right) \tag{75b}$$

$$\{F^*\} = [B(t)]^T\{Q(t)\} \tag{75c}$$

With the help of symbolic computational software available in MATLAB, Eqs. (75a-75c) can be computed to obtain the 8×1 output column matrix that governs a gyroscopic ocean wave energy converter.

3.2.6 Simplified Mathematical Model

To simplify the analysis of the GOWEC, the motion of both the rotor and buoy will be prescribed, leaving only the equation of motion for the gimbal. To estimate the angular velocity of the buoy, a wave propagating along the positive x_2-axis will be considered as shown in Fig. 1:

$$\eta(x_2,t) = a * \cos\left(2\pi\left(\frac{x_2}{\lambda} - \frac{t}{T}\right)\right) \tag{76}$$

where a is the wave amplitude, T is the wave period, and λ is the wave length [13]. Assuming the buoy rocks due to the tangent of the wave surface profile, the rotation angle $\beta(t)$ along the x_1-axis at $x_2 = 0$ can be expressed as shown below in Eq. (77).

$$\beta(t) \approx \frac{\partial\eta}{\partial x_2}(0,t) = \frac{2\pi a}{\lambda}\sin\left(\frac{2\pi t}{T}\right) \tag{77}$$

The magnitude of $\beta(t)$ is also known as the wave's steepness, normally expressed using the wavenumber and the wave amplitude as ka. By taking the time derivative of Eq. (77), the first and only non-zero component of the buoy angular velocity vector can be obtained.

$$\omega_1^{(1)}(t) = \dot{\beta}(t) = \frac{(2\pi)^2 a}{T\lambda} cos\left(\frac{2\pi t}{T}\right), \omega_2^{(1)}(t) = \omega_3^{(1)}(t) = 0 \tag{78}$$

Using a deep water wave approximation for the wavelength, $\lambda = \frac{gT^2}{2\pi}$, the angular velocity magnitude can be simplified to $A = \left(\frac{2\pi}{T}\right)^3\left(\frac{a}{g}\right)$, allowing us to express the angular velocity in terms of wave amplitude and period. The above buoy rocking will work as a preliminary

approximation. For larger scale computations with a known buoy geometry, the impedance matrix must be accounted for [17]. To further simplify the gimbal's equation of motion, the moment of inertia assumptions shown in Eq. (79) below are used. The assumptions are valid for a thin disk rotor with a large angular momentum and a symmetric inner gimbal with a considerable small moment of inertia with respect to the rotor.

$$J_{1C}^{(3)} = J_{2C}^{(3)} = \frac{J_{3C}^{(3)}}{2}, J_{1C}^{(2)} = J_{2C}^{(2)} = J_{3C}^{(2)}, J_{3C}^{(2)} \ll J_{3C}^{(3)} \tag{79}$$

The equation of motion for the gimbal is thus expressed as follows:

$$\begin{aligned} J_{3C}^{(3)} \left\{ \frac{1}{2} \ddot{\varphi}^{(2)}(t) + \left(\omega_1^{(1)}(t)\right)^2 \left(\frac{1}{4} \sin\left(2\varphi^{(2)}(t)\right)\right) \right. \\ \left. - \omega_1^{(1)}(t) \dot{\psi}^{(3)} \cos\left(\varphi^{(2)}(t)\right)\right) \Big\} + M^{(g)} = 0 \end{aligned} \tag{80}$$

Substituting for $\omega_1^{(1)}(t)$ using Eq. (78) in the above expression, provides the equation of motion in terms of the system and wave parameters.

$$\begin{aligned} J_{3C}^{(3)} \left\{ \frac{1}{2} \ddot{\varphi}^{(2)}(t) - \left(A\cos\left(\frac{2\pi t}{T}\right)\right)^2 \frac{1}{4} \sin\left(2\varphi^{(2)}(t)\right) \right. \\ \left. - A\cos\left(\frac{2\pi t}{T}\right) \dot{\psi}^{(3)} \cos\left(\varphi^{(2)}(t)\right) \right\} + M^{(g)} = 0 \end{aligned} \tag{81}$$

The equation of motion above is a nonlinear second order differential equation of motion that governs the motion of the gimbal due to an incoming wave exciting the buoy. It is now noted that the most important term for power generation is the third term in the equation of motion, containing the rotor angular velocity $\dot{\psi}^{(3)}$. If the rotor of the gyroscope is switched off, only the first two terms will remain, accounting only for the inertia and buoy oscillation effects.

3.2.7 Power Generation

The power generated by the inner gimbal, P, can be described by the couple $M^{(g)}$ and the angular velocity $\dot{\varphi}^{(2)}$:

$$P = M^{(g)}\dot{\varphi}^{(2)}, \tag{82}$$

where $M^{(g)}$ can be obtained from the equation of motion in Eq. (81). Of interest is the gyroscopically generated power, P_g, arising from the third term in the equation of motion. P_g can thus be expressed as a function of the system and wave parameters as shown in Eq. (83).

$$P_g = \left(J_{3C}^{(3)} A \cos\left(\frac{2\pi t}{T}\right) \dot{\psi}^{(3)} \cos\left(\varphi^{(2)}(t)\right)\right) \dot{\varphi}^{(2)}(t) \tag{83}$$

To obtain the average gyroscopically generated power, the integral of P_g is taken over an ocean wave period T as shown in Eq. (84).

$$\bar{P}_g = J_{3C}^{(3)} A \dot{\psi}^{(3)} \left(\frac{1}{T}\right) \int_0^T \cos\left(\frac{2\pi t}{T}\right) \cos\left(\varphi^{(2)}(t)\right) \dot{\varphi}^{(2)}(t)\, dt \tag{84}$$

Evaluating the integral using integration by parts results in the expression below:

$$\bar{P}_g = J_{3C}^{(3)} A \dot{\psi}^{(3)} \left(\frac{1}{T}\right) \left[\sin\left(\varphi^{(2)}(T)\right) - \sin\left(\varphi^{(2)}(0)\right) + \left(\frac{2\pi}{T}\right) \int_0^T \sin\left(\frac{2\pi t}{T}\right) \sin\left(\varphi^{(2)}(t)\right)\, dt \right] \tag{85}$$

To maximize the average gyroscopically generated power output, it can be noted that $\varphi^{(2)}(t)$ must be matched with $2\pi t/T$. After doing so and substituting in for A, the

maximum average power that can be produced with a single gyroscope configuration thus becomes:

$$\left(\bar{P}_g\right)_{max} = \frac{1}{2}\left|\dot{\psi}^{(3)}\right| J_{3C}^{(3)} \left(\frac{a}{g}\right)\left(\frac{2\pi}{T}\right)^4 \tag{86}$$

The major parameters that can be controlled to proportionally affect the power produced are the moment of inertia and angular velocity of the rotor. As can be seen by the above equation, the highest rated power output is produced in oceanic regions with high amplitude and, more importantly, high frequency waves. To match the gimbal motion to the incoming wave in order to maximize the power output, a phase locking loop can be implemented in the system.

The equation for the maximum average power output can also be expressed in terms of the buoy rotation angle rather than ocean wave parameters. Using Eq. (87), the buoy rotation can alternatively be expressed as the following:

$$\beta(t) \approx \frac{\partial \eta}{\partial x_2}(0,t) = \beta_o \sin\left(\frac{2\pi t}{T}\right) \tag{87}$$

In the above, β_o is the amplitude of rotation. Carrying β_o through the above maximum average power derivation, it is noted from Eq. (88) below, that power is proportional to the rotation angle and the squared incoming wave frequency.

$$\left(\bar{P}_g\right)_{max} = \frac{1}{2}\left|\dot{\psi}^{(3)}\right| J_{3C}^{(3)} \beta_o \left(\frac{2\pi}{T}\right)^2 \tag{88}$$

3.2.8 2-Dimensional Ocean Wave Excitation

The maximum average power expression shown in Eq. (86) assumed an incoming wave traveling along a single axis (Eq. (76)), thus exciting the buoy only about that one axis. Of more general interest is the excitation of the buoy from a 2-dimensional ocean

wave and its effect on the maximum power output that can be obtained. We will describe the 2-dimensional ocean wave profile as shown in Eq. (89).

$$\eta(x_1, x_2, t) = a\cos(kx_1\cos\theta + kx_2\sin\theta - \omega t) \tag{89}$$

Figure 3 demonstrates visually the directional wave with respect to the orientation of the buoy. As can be noted, if $\theta = \frac{\pi}{2}$, the above expression simplifies to that shown in Eq. (76) which denotes a wave traveling along the x_2-axis.

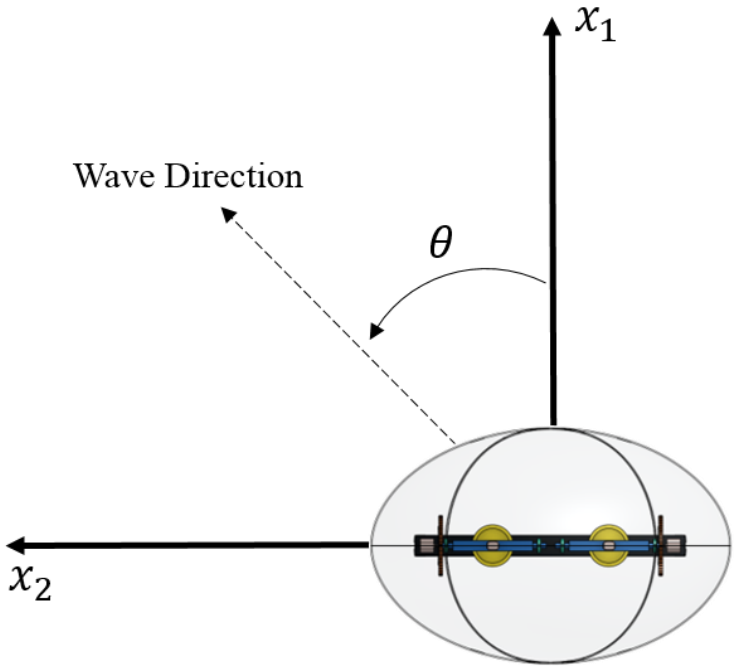

Figure 3-3: 2D harmonic wave profile exciting the buoy

Of interest is the angular velocity that the incoming wave will induce on the buoy, specifically $\omega_1^{(1)}(t)$ and $\omega_2^{(1)}(t)$. Once again, we will assume that buoy rocks due to the tangent of the wave surface profile. Thus, the rotation of the buoy can be expressed along the x_1 and x_2 axes by taking the partial derivatives and setting $x_1 = x_2 = 0$.

$$\beta_1^{(1)} = \frac{\partial \eta(0,0,t)}{\partial x_2} = ak\sin(\omega t)\sin(\theta) \tag{90}$$

$$\beta_2^{(1)} = \frac{\partial \eta(0,0,t)}{\partial x_1} = ak\sin(\omega t)\cos(\theta) \tag{91}$$

The first two angular velocity components can thus be expressed after taking the time derivative of the above expressions.

$$\omega_1^{(1)} = \dot{\beta}_1^{(1)} = ak\omega\cos(\omega t)\sin(\theta) \tag{92}$$

$$\omega_2^{(1)} = \dot{\beta}_2^{(1)} = ak\omega\cos(\omega t)\cos(\theta) \tag{93}$$

Using the newly obtained components, the gyroscopic power can thus be expressed below:

$$P_g = \left(J_{3C}^{(3)} A\cos(\omega t)\sin(\theta)\,\dot{\psi}^{(3)}\cos\left(\varphi^{(2)}(t)\right)\right)\dot{\varphi}^{(2)}(t) \tag{94}$$

As can be noted, the expression above simply adds the $\sin(\theta)$ term which modulates the power output that can be obtained. Thus, the maximum average power output that can be produced from a 2D ocean wave can be expressed as shown below in Eq. (95). Once again, to maximize the power output over a period, the gimbal motion must be matched to the frequency of the incoming wave.

$$\left(\bar{P}_g\right)_{max} = \frac{1}{2}\left|\dot{\psi}^{(3)}\right| J_{3C}^{(3)}\left(\frac{a}{g}\right)\left(\frac{2\pi}{T}\right)^4 \sin(\theta) \tag{95}$$

From the above expression, we can first note that if the incoming ocean wave is along the x_1-axis, corresponding to $\theta = 0$, the power output would be zero. Physically, this result makes sense and occurs because the buoy and gimbal are both rotating about the same axis. As expected, we get Eq. (86) if the wave is solely traveling along the x_2-axis, $\theta = \pi/2$.

3.2.9 Changes in Period Excitations

Apart from wave direction, incoming ocean waves will vary in frequency, altering the buoy rotation rate. Of interest is the effect of changes in frequency on the power output of the GOWEC. After matching the motion of the gimbal to the incoming wave to maximize the average power output, the frequency of excitation can vary slightly. To express the power loss of the system, Eq. (86) will be further observed. If the gimbal motion has been already matched with that of predominant ocean wave frequency in a specific location, in other words $\varphi^{(2)}(t) = \frac{2\pi t}{T}$, the terms of importance in Eq. (96), other than the system parameters, are the two remaining cosine terms. To observe the effect of a change in the incoming ocean wave period, a new variable ϵ is introduced as seen below in Eq. (96).

$$P_g = J_{3C}^{(3)} A\dot{\psi}^{(3)}\, \dot{\varphi}^{(2)}(t) \left(\cos\left(\frac{2\pi t}{T+\epsilon}\right)\cos\left(\frac{2\pi t}{T}\right)\right) \tag{96}$$

By observing the cosine terms, assuming the constants are equal to 1W and $T = 4$s for demonstration purposes, the effect of ϵ on the power output can be shown as in Fig. 4. As can be seen, when $\epsilon = 0$, the maximum average power output is equal to that obtained in Eq. (83). If the exciting period is varied by as little as 1%, a power output decrease of 20% is shown. Note, the maximum average power output levels off because the controller is keeping the gimbal rotating at the initially prescribed rate.

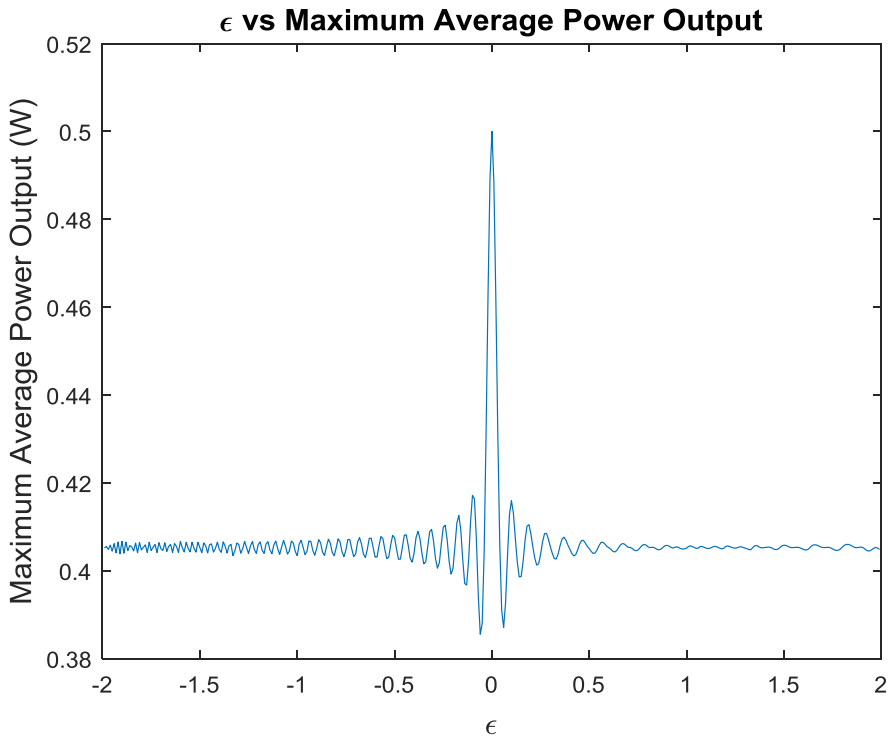

Figure 3-4: The maximum average power output as the excitation period varies from $-T/2$ to $T/2$ for $T = 4s$

3.2.10 Potential Power Output Using Off-the-Shelf Gyroscopic Units

To better estimate the possible electrical power that can be generated, off-the-shelf gyroscopic roll stabilizers by Seakeeper will be used in the model. Seakeeper offers six gyroscopic roll stabilizer models, each with a vacuum-sealed rotor and varying angular momentum to accommodate a wide range of vessels. The angular momentum and RPM of the rotors, as well as the spool up power consumption for each of the models, is shown in Table 1 [18]. The active gyroscopic roll stabilizers produced by Seakeeper and other companies, as will be mentioned in section 3.3, have the inner gimbal excited to produce a moment on the outer housing (or ship). For the GOWEC, the inner gimbal is the output while the outer housing (the buoy) is excited. While these differences mean that the

Seakeeper stabilizers cannot be used without modification, they do provide a vacuum sealed rotor enclosure that is ideal to maximize the power output.

Table 3-1: Seakeeper gyroscopic stabilizers

Model No.	**Rotor RPM**	**Angular Momentum**	**Power Consumption (W)**
3DC	6400	3000	900
5	10700	5000	2000
9	9000	9000	2000
16	6130	16000	3000
26	5000	26000	3000
35	5150	35000	5000

Using Eq. (86), the maximum electrical power output for each of the models offered by Seakeeper can be approximated. Assuming a generator efficiency of 80% and subtracting the power consumption needed to power the rotor, the power output for two of the larger gyro models is obtained as a function of both wave height and period as shown in Fig. 5. It should be noted that not all the wave conditions shown in Fig. 5 are attainable. The maximum wave crest angle before deep water waves begin to break is known to be 120°, which indicates that the largest rotation angle that the buoy can achieve is 30° or 0.5236 radians [17]. Using this rotation constraint and a deep water wave approximation, a relationship between the wave period and wave height can be obtained as shown in Eq. (97).

$$\frac{a}{gT^2} \leq 0.01326 \tag{97}$$

This rotation constraint is shown in Fig. 5 as a dashed-curve, where anything below the curve indicates attainable wave conditions, or waves that are yet to break. The system thus has the capabilities of producing power in the magnitude of kW or even MW in

oceanic regions where the buoy rapidly oscillates at high frequencies and when the gimbal motion is matched with the incoming wave. It should also be noted from the darker regions in Fig. 5, that the system has limitations in terms of deployment locations with respect to efficiency and feasibility. Regions shown in black indicate zero net power output.

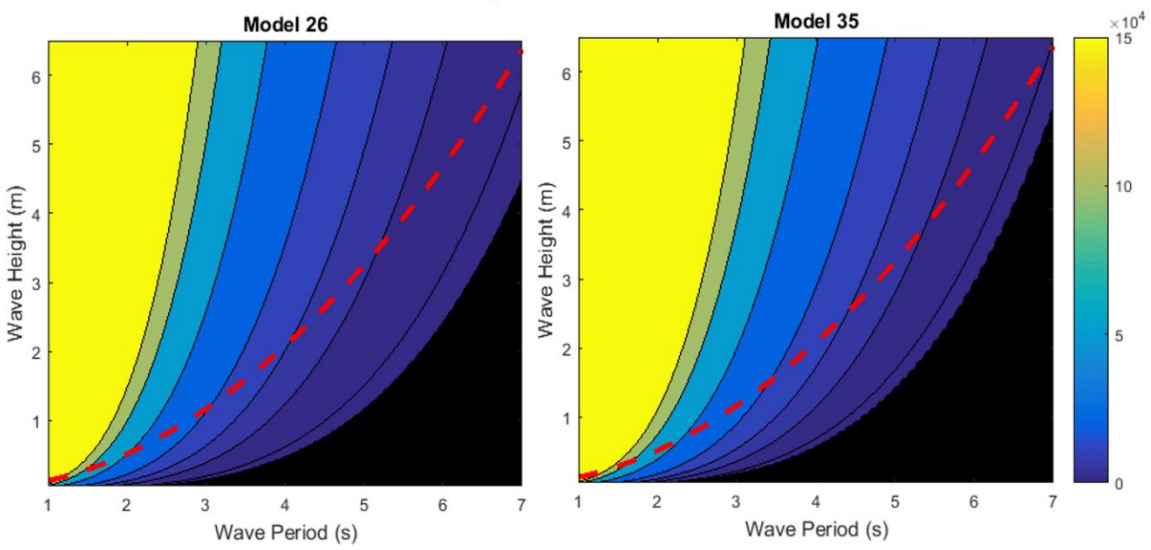

Figure 3-5: Power estimation using the Seakeep Model's 26 and 35

3.3 The Gyroscopic Stabilizer

3.3.1 The Gyroscopic Stabilizer Introduction

The introduction of gyroscopes as a means of stabilization and attitude control has been well documented in various fields. Of interest in the research presented is the development of a mathematical model for the application of gyroscopes in the stabilization of offshore systems and validation with preliminary experiments. The rolling and pitching of ships and boats induced by the ocean waves results in undesirable motion. In an effort to increase the stability of the deck/platform and human comfort and safety, various add-on stability systems have been developed. The add-on systems can be classified as internal

or external, and further subdivided and labeled as active or passive. Internal and external systems generate forces and moments inside and outside the hull, respectively. Active systems require a forced input while passive systems simply react to wave induced motions to improve stability of the marine vessel. Of interest in the research presented are internal active systems, specifically the active gyroscopic stabilizer. Work on gyroscopic stabilization of marine vessels dates back to the early 1900's, with work from Thomas Forbes (1904), Ernst Otto Schlick (1904), and Elmer Perry (1908) [19-21]. The work on gyroscopic roll stabilizers continues to this day in both industry and academia. Of interest in the research presented is the development of a mathematical model using the moving frame method for an internal active gyroscopic stabilizer.

Previous research and industrial use, specifically in the past couple decades, have shown the validity of the gyroscopic roll stabilizer in reducing rolling motion of ships: Works in academia by Townsend, who proposed a continuous method of excitation, and in industry by Seakeeper, have shown a roll reduction rate of 30% to 70% and 70% to 90%, respectively [18,22]. The research presented here will be focused on developing a general mathematical model for gyroscopic stabilization. Through the use of the moving frame method, we will show a systematic derivation of the equations of motion and identify key design parameters and their impact on the output torque [1,2].

It is known that the use of a single gyroscope will create unwanted reactionary moments. To address the reactionary moments, the derivation addresses a system with a dual gyroscope configuration. Initially, the utmost general nonlinear equations of motion are obtained. The mathematical model is then simplified to more clearly examine the role of the different gyroscope parameters and their effect on roll stabilization. In addition to

the parameters, we further look into different methods of exciting the gimbal and the effect that the rate of excitation has on the structure. The simplified model is then solved numerically for the proposed methods of rocking through the use of the fourth order Runge-Kutta method.. The goal of this study is thus to analyze the key converter parameters to better aid the design and control of the active gyroscopic stabilizer.

3.3.2 Model System Description

The model system that will be analyzed is pictured in Fig. 6 below. As shown in the figure, the system consists of a double gyroscope configuration, which cancels the reactionary moments on the deck/platform that would appear if only a single gyroscope were installed. With the dual gyroscope system, the reactionary moments can be cancelled if one of the gyroscopes has the rotor and gimbal excitation operating in reverse.

Each gyroscope consists of a rotor operated by a motor and a gimbal excited by either a hydraulic system, or servo as done in the preliminary experiments. Both gyroscopes are then bolted down to the deck or platform of the body. As the gimbal is rocked around one axis and the rotor spins around a second axis, a gyroscopic moment is produced around the third axis. The direction of the gyroscopic moment is determined by the direction of the rotor and gimbal excitation. The major components of the system that will be included in the analysis will be the outer body (ship or offshore platform), gimbals, and rotors.

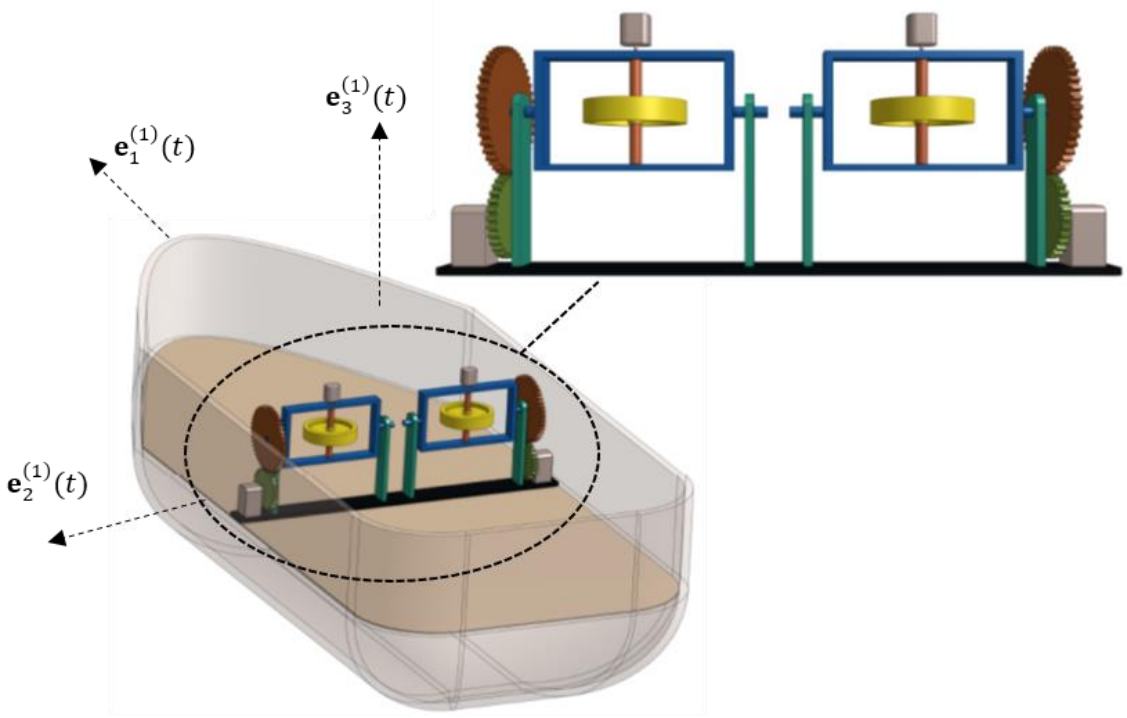

Figure 3-6: Model ship installed with dual gyroscopes

3.3.3 Mathematical Model of Dual Gyroscope Configuration

The mathematical model of the system shown in Fig. 6 equipped with dual gyroscopic roll stabilizers will be obtained. In this section of the chapter, we will use some of the previously derived equations for the GOWEC. Due to the similar nature of both the stabilizer and the GOWEC, only minor modifications to the equations need to be made. After obtaining the equations of motion, we will then simplify the mathematical model to gain insight into the role of the different system parameters. The main difference between this and the energy converter is the component that is excited. While the buoy, or outer housing, was excited in the GOWEC to produce a gimbal rotation, the stabilizer will have the gimbal excited to produce a gyroscopic moment on the ship. To easily see the effect of

the parameters, the model will be simplified to a single gyroscope which allows for an easier interpretation of the system.

3.3.3.1 Kinematics of System

Much of the kinematics of the stabilizer will be the same as that previously derived for the GOWEC. As can be noted from the previous sections, the main objective in the kinematics section is to obtain the $[B(t)]$ matrix, shown in Eq. (49), which relates the generalized velocities $\{\dot{X}(t)\}$ and the essential generalized velocities $\{\dot{X}^*(t)\}$. It can be noted that the kinematics of both the GOWEC and the active gyroscopic stabilizer are similar. The ship to be analyzed, like the GOWEC's buoy, is initially free to translate and rotate, the rotor spins along the $\mathbf{e}_3^{(3)}(t)$ axis, and the gimbal rotates along the $\mathbf{e}_2^{(2)}(t)$ axis. Since the motion of the ship/marine-vessel is the desired output, the kinematics will be obtained with two gyroscopic units as shown in Fig. 6. The kinematics of the ship will once again progress from the outermost component to the innermost as seen in the kinematic graph tree in Fig. 7. Before the kinematics section, the essential generalized velocities need to be identified to properly express the velocity and angular velocity vectors and build the $[B(t)]$ matrix. The ship, since not constrained initially, will have $\dot{x}_c^{(1)}(t)$ and $\omega^{(1)}(t)$ as the essential generalized velocities. The rotors and gimbals are constrained to only rotate around a single axis, therefore, rather than using the three components of $\omega^{(2)}(t)$, $\omega^{(3)}(t)$ etc., the essential generalized velocities will be expressed as $\dot{\varphi}^{(2)}$and $\dot{\psi}^{(3)}$ respectively. This greatly simplifies the number of equations of motion and allows the user to easily prescribe the angular velocity of either the rotor or gimbal on the ship.

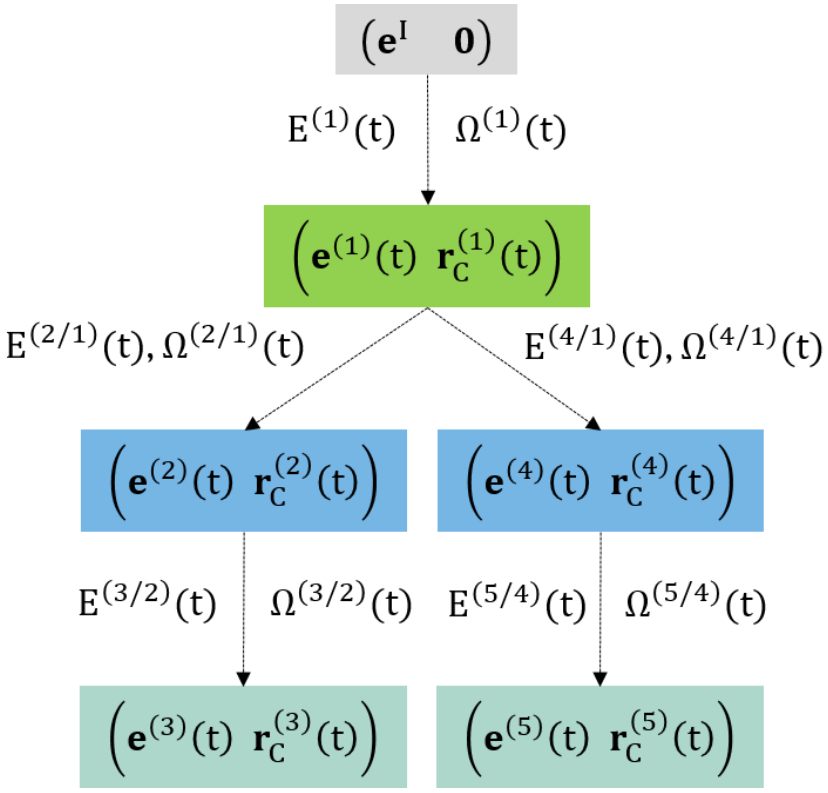

Figure 3-7: Kinemtaics graph tree of stabilizer with dual gyroscopes

3.3.3.1.1 Ship Frame Connection Matrix

The ship frame connection matrix $E^{(1)}(t)$ and the time rate of the ship frame connection matrix $\Omega^{(1)}(t)$ are identical to that of the GOWEC's buoy as shown in Eq's. (21) - (23).

3.3.3.1.2 Gimbal Frame Connection Matrices

Two symmetrically placed gimbals will be analyzed. The corresponding vector basis of the gimbals' will be expressed as $\mathbf{e}^{(2)}(t)$ and $\mathbf{e}^{(4)}(t)$. The gimbals, which are the user controlled inputs, will be excited by equal but opposite torques around the $\mathbf{e}_2^{(2)}(t)$ and $\mathbf{e}_2^{(4)}(t)$ respectively with reference to the ship's moving frame. Therefore, the rotation

matrices will be defined around the same axis and by equal but opposite angles as shown below:

$$\mathbf{e}^{(2)}(t) = \mathbf{e}^{(1)}(t)R_2^{(2/1)}\left(\varphi^{(2)}(t)\right), \tag{98}$$

$$\mathbf{e}^{(4)}(t) = \mathbf{e}^{(1)}(t)R_2^{(4/1)}\left(-\varphi^{(2)}(t)\right). \tag{99}$$

From Fig. 6, it is assumed that the gimbals are placed symmetrically on the $\mathbf{e}_2^{(1)}(t)$ and $\mathbf{e}_3^{(1)}(t)$ plane. For more general placement, only minor modifications to the first component of the relative position vectors below need to be made

$$\boldsymbol{s}_c^{(2/1)}(t) = \mathbf{e}^{(1)}(t)s_c^{(2/1)} = \mathbf{e}^{(1)}(t)\begin{bmatrix}0\\h_2\\h_3\end{bmatrix}, \tag{100}$$

$$\boldsymbol{s}_c^{(4/1)}(t) = \mathbf{e}^{(1)}(t)s_c^{(4/1)} = \mathbf{e}^{(1)}(t)\begin{bmatrix}0\\-h_2\\h_3\end{bmatrix}. \tag{101}$$

With the frames and relative position vectors now defined, the connection matrices can be built and the time derivative of those matrices can be obtained to get the angular velocity and velocity vectors. Since the process has been reviewed in the previous GOWEC section, only the final vectors are shown. The angular velocity vectors with respect to the $\mathrm{e}^{(2)}(t)$ and $\mathrm{e}^{(4)}(t)$ frames are as follows:

$$\omega^{(2)}(t) = \left({R_2}^{(2/1)}\left(\varphi^{(2)}\right)\right)^T \omega^{(1)} + \dot{\varphi}^{(2)}\mathrm{e}_2 \tag{102}$$

$$\omega^{(4)}(t) = \left({R_2}^{(4/1)}\left(-\varphi^{(2)}\right)\right)^T \omega^{(1)} - \dot{\varphi}^{(2)}\mathrm{e}_2 \tag{103}$$

and the velocity vectors with respect to the inertial frame:

$$\dot{x}_c^{(2)} = \dot{x}_c^{(1)} + R^{(1)}(t)\left(\overleftrightarrow{s_c^{(2/1)}}^T\right)\omega^{(1)} \tag{104}$$

$$\dot{x}_c^{(4)} = \dot{x}_c^{(1)} + R^{(1)}(t)\left(\overleftrightarrow{s_c^{(4/1)}}^{T}\right)\omega^{(1)} \tag{105}$$

3.3.3.1.3 Rotor Frame Connection Matrices

The rotors, which are housed within the gimbals, will also have attached coordinates frames and vector bases $\mathbf{e}^{(3)}(t)$ and $\mathbf{e}^{(5)}(t)$. Similar to the gimbals, the rotors will be excited by equal but opposite torques around the $\mathbf{e}_3^{(3)}(t)$ and $\mathbf{e}_3^{(5)}(t)$ to cancel any reactionary moments. Therefore, the rotation angle of the rotor with the attached $\mathbf{e}^{(5)}(t)$ frame, is expressed as $-\psi^{(3)}(t)$.

$$\mathbf{e}^{(5)}(t) = \mathbf{e}^{(4)}(t)R_2^{(5/4)}\left(\psi^{(3)}(t)\right), \tag{106}$$

$$\mathbf{e}^{(3)}(t) = \mathbf{e}^{(2)}(t)R_2^{(3/2)}\left(-\psi^{(3)}(t)\right). \tag{107}$$

Next, the relative position vectors of the rotors with respect to the gimbal's center of mass will be obtained. Assuming the rotors are placed such that the center of masses coincide with that of the gimbals', the relative position vectors will simply be zero vectors as shown below:

$$\boldsymbol{s}_c^{(5/4)}(t) = \mathbf{e}^{(4)}(t)s_c^{(5/4)} = \mathbf{e}^{(4)}(t)\begin{bmatrix}0\\0\\0\end{bmatrix}, \tag{108}$$

$$\boldsymbol{s}_c^{(3/2)}(t) = \mathbf{e}^{(2)}(t)s_c^{(3/2)} = \mathbf{e}^{(2)}(t)\begin{bmatrix}0\\0\\0\end{bmatrix}. \tag{109}$$

The above completes the work necessary for the assembly of the relative connection matrices $E^{(5/4)}(t)$ and $E^{(3/2)}(t)$ that contain the relative position and orientation of the rotors with respect to the gimbal frames. As done with the GOWEC, by simply taking the

time derivative of the connection relationships, the angular velocity vectors with respect to the rotor frames can be obtained are systematically obtained:

$$\omega^{(3)}(t) = \left(R^{(3/1)}\right)^T \omega^{(1)} + \left(R_3^{(3/2)}\left(\psi^{(3)}\right)\right)^T \dot{\varphi}^{(2)}\mathrm{e}_2 + \dot{\psi}^{(3)}\mathrm{e}_3 \tag{110}$$

$$\omega^{(5)}(t) = \left(R^{(5/1)}\right)^T \omega^{(1)} - \left(R_3^{(5/4)}\left(\psi^{(5)}\right)\right)^T \dot{\varphi}^{(2)}\mathrm{e}_2 - \dot{\psi}^{(3)}\mathrm{e}_3 \tag{111}$$

In the above expressions, $R^{(3/1)}$ and $R^{(5/1)}$ are expressed as the following:

$$R^{(3/1)} = R_2^{(2/1)}\left(\varphi^{(2)}\right)R_3^{(3/2)}\left(\psi^{(3)}\right), \tag{112}$$

$$R^{(5/1)} = R_2^{(4/1)}\left(-\varphi^{(2)}\right)R_3^{(5/4)}\left(-\psi^{(3)}\right). \tag{113}$$

Since the rotors center of masses coincide with the gimbals center of masses, the velocity vectors of the rotors will be identical to that of the gimbals.

3.3.3.2 Generalized Velocities

The generalized velocities, which include the velocity and angular velocity vectors of all the components, can be expressed by a set of independent velocities referred to as the *essential generalized velocities*, assembled in an 8×1 column matrix $\{\dot{X}^*(t)\}$.

$$\{\dot{X}(t)\} = \begin{pmatrix} \dot{x}_c^{(1)} \\ \omega^{(1)} \\ \dot{x}_c^{(2)} \\ \omega^{(2)} \\ \dot{x}_c^{(3)} \\ \omega^{(3)} \\ \dot{x}_c^{(4)} \\ \omega^{(4)} \\ \dot{x}_c^{(5)} \\ \omega^{(5)} \end{pmatrix}, \quad \{\dot{X}^*(t)\} = \begin{pmatrix} \dot{x}_c^{(1)} \\ \omega^{(1)} \\ \dot{\varphi}^{(2)} \\ \dot{\psi}^{(3)} \end{pmatrix} \tag{114}$$

For the case at hand, where the gimbals and rotors are rotating by equal amounts in opposing directions, only 8 essential generalized velocity components are needed. If not

for this restriction, the essential generalized velocity vector would include a total of 10 components to account for the two additional rotations. The generalized velocities are linearly related to the essential generalized velocities through the $[B(t)]$ matrix as shown in the appendix. The derivation of the $[B(t)]$ matrix concludes the kinematic analysis of a ship installed with dual gyroscopic roll stabilizers.

3.3.3.3 Kinetics of System

The equations of motion can thus be directly calculated using the expression previously derived and shown in Eq's. (74-75). The three necessary matrices, $[M]$, $[D(t)]$, and $[B(t)]$ are known and shown in the Appendix in Eq's. (120-122) and can be used to derive the mathematical model. After symbolically solving Eq. (74), the user will obtain a 10×1 column vector that contains the coupled differential equations of motion.

To specifically apply the mathematical model to the gyroscopic stabilizer, the inputs of the system and the external moments and forces must be defined and incorporated into the equations. The user defines the motion of both the rotor and the gimbal, and thus the variational statement below can be applied:

$$\delta\varphi = \delta\psi = 0 \tag{115}$$

The above simplifies the system to six equations of motion that govern the six degrees of freedom of the ship: surge, heave, sway, roll, yaw, and pitch. The non-conservative and conservative forces present will be assumed to be the same as those in the GOWEC, which included the wave induced forces and moments and the reactionary couples from the motors. For the case of the stabilizer, rather than a generator connected to the gimbal, a motor will be placed for excitation. Since the rotors and gimbals are excited in the opposite direction, the action and reaction moments cancel and thus do not affect the ship.

The utmost general mathematical model that governs the active gyroscopic roll stabilizer can thus be obtained. In the sections to follow, the equations of motion will be simplified to clearly see the role of different parameters.

3.3.4 Simplified Mathematical Model

The six equations of motion that obtained are extremely nonlinear, mainly due to the relative position vectors of the gimbals relative to the ship's center of mass. To validate the mathematical model, the equations of motion will be further simplified. This will also allow us to easily solve the equations of motion numerically as well as clearly see the effect of several of the system parameters such as period and amplitude of excitation. To simplify the mathematical model, a few assumptions will be made. First, it will be assumed that the ship will not translate.

$$\delta x_C^{(1)} = 0. \tag{116}$$

Note, this assumption greatly simplifies the rotational equations of motion of the ship. When assuming no translational motion, the position of the gyroscopes relative to the ship's frame has very little impact on the yaw, pitch, and roll of the ship. If translational motion were to be considered, the relative position vectors of the gimbals will appear in the equations of motion coupled with the components of the ship's rotation matrix relative to the inertial frame, $R^{(1)}(t)$. For that case, the rotation matrix would need to be constructed at every time step by using the reconstruction scheme presented in Chapter 2. Second, the following mass moment of inertia relations will be assumed for the rotors and gimbals:

$$J_1^{(3)} = J_2^{(3)} = J_3^{(3)}/2, J_1^{(2)} = J_3^{(2)} = J_2^{(2)} \tag{117}$$

The above simply assumes a thin disk as a rotor and a fully symmetric gimbal, similar to the spherical enclosure used by Seakeeper in their stabilizers.

The equations of motion governing the roll, pitch, and yaw of a ship installed with two gyroscopic stabilizers, after taking the assumptions into account, can thus be obtained and are shown in the Appendix in Eq's. (123-125) (the equations of motion for a ship installed with a single gyroscope are also shown in the Appendix in Eq's. (126-128)). As can be noted, they are coupled first order differential equations. The ocean induced moments present in the equations will be a summation of the hydrostatic components, the added mass and damping components, and the exciting moment proportional to the incident wave amplitude [23]. For the complete solution of the problem, the geometrical and mass properties of the boat are necessary for the adequate calculation of the added mass and damping coefficients.

3.3.4.1 Methods of Gimbal Excitation

Two methods have been previously proposed to eliminate the rolling motion. The traditional method rocks, or nutates, the gimbal back and forth accordingly to eliminate or reduce the rolling motion. Seakeeper for example, follows the traditional method for stabilizing ships [18]. By detecting the rate and rolling angle of the ship, an onboard controller outputs the gimbal rotation. The second method, proposed by Townsend et al., rotates the gimbal continuously to reduce roll [10]. While the first method changes the direction of the applied torque (rocking of the gimbal), the second passively changes the direction of the rotor's angular momentum vector every 180° of rotation. To observe the effect of both methods on the system, the equations of motion will be numerically solved without the presence of the ocean induced moments using the gimbal excitation

expressions shown in Eq's. (118-119) along with the following test values: $J_1^{(1)} = 10e5\ , J_2^{(1)} = 10e8\ , J_3^{(1)} = 10e9, J_2^{(2)} = 10, J_3^{(3)} = 50\ kgm^2, \dot{\psi} = 8050\ RPM.$ The test values were simply chosen for demonstration purposes and do not reflect the mass properties of a marine vessel.

$$\varphi^{(2)}(t) = 4a_g(f_g)t \quad \text{– Continuous Excitation} \tag{118}$$

$$\varphi^{(2)}(t) = a_g \sin(2\pi f_g t - phi) \text{ – Sinusoidal Excitation} \tag{119}$$

In the above, a_g is the amplitude of oscillations in radians and f_g is the frequency. The phase of the sinusoidal excitation will be assumed to be zero. The above two methods and their respective time derivative, or angular velocity, are shown below in Fig. 8. The continuous method of excitation thus has a constant angular velocity value of $4a_g(f_g)$ while the oscillating method is represented by a cosine function.

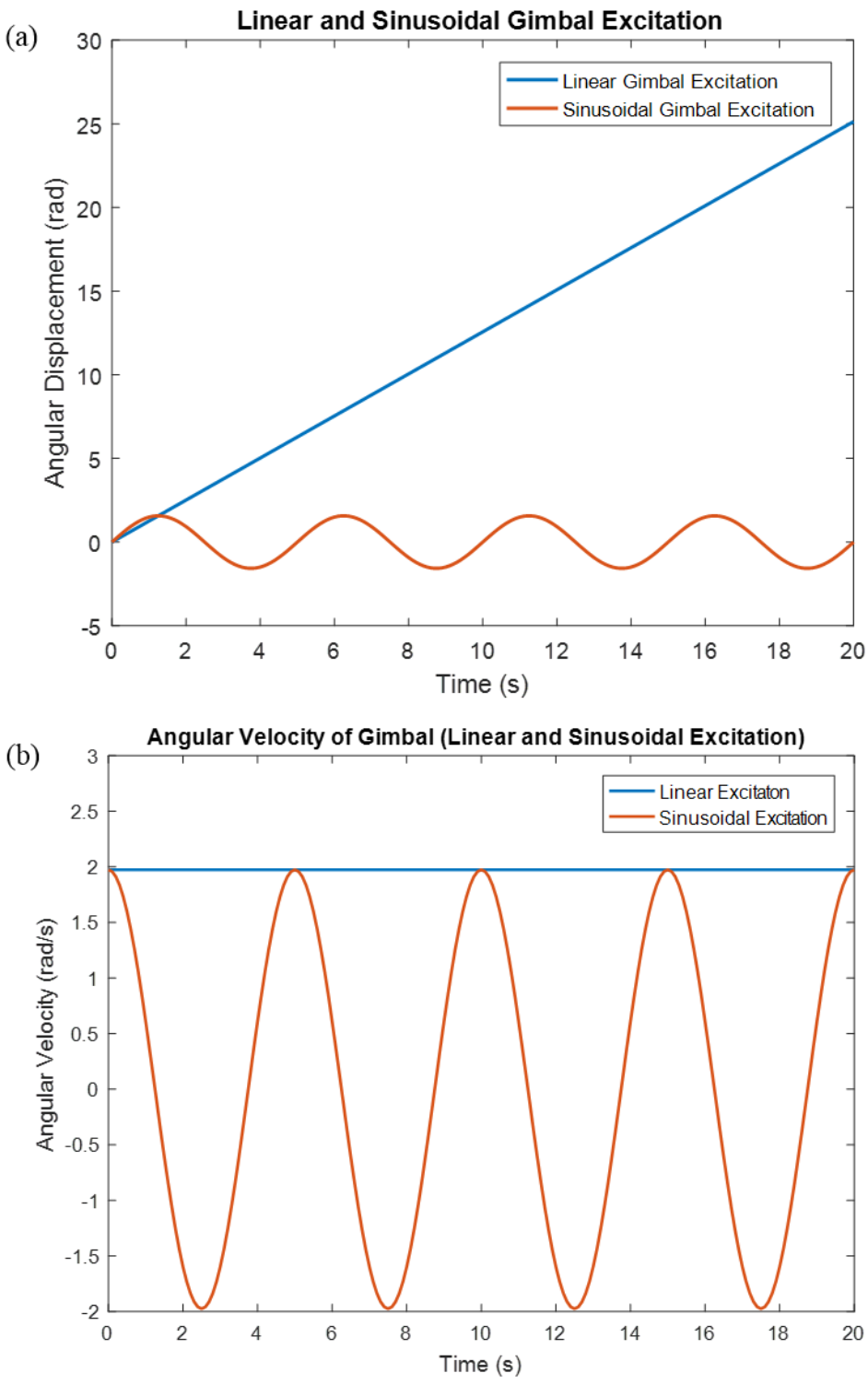

Figure 3-8: (a) Angular displacement of both linear and sinusoidal excitation and (b)angular velocity of the gimbal excitation methods

The slope of the continuous excitation was chosen such that when $t = T$, both methods of excitation travel the same angular distance. Of specific interest is when $a_g = \pi/2$. At this chosen amplitude, both methods should theoretically have the same effect. In other words, both methods of excitation reverse the direction of one of the vectors in the system (input torque on the gimbal by the sinusoidal method and angular velocity vector of the rotor by the continuous method) at the same time. Figure 9 demonstrates the numerical solutions of the three governing equations of motion. Shown is the output angular velocity components of the ship using both methods of excitation and with zero initial angular velocity components ($\omega_1^{(1)}(0) = \omega_2^{(1)}(0) = \omega_3^{(1)}(0) = 0$).

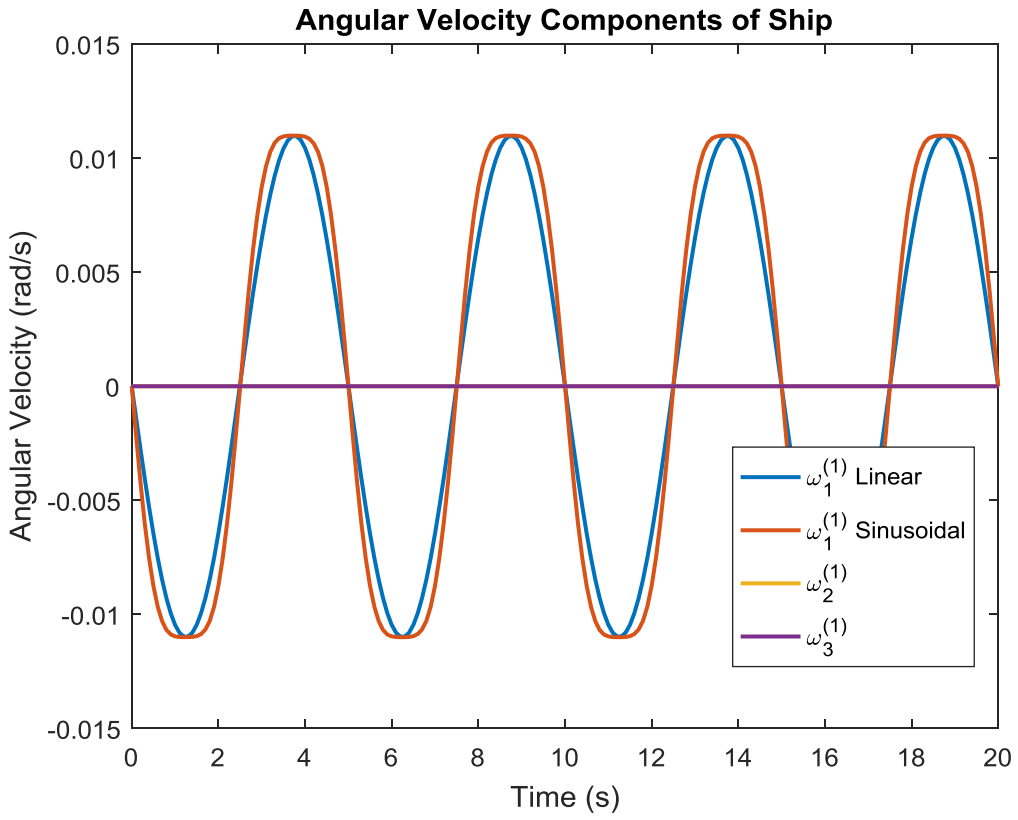

Figure 3-9: Output angular velocity components of the ship from the liner and sinusoidal excitation.

While both excitation methods produce the same results, the continuous method is restricted by the fact that it needs to travel half a revolution before applying a moment on the ship in the opposite direction. Also to note is the phase of the sinusoidal excitation in comparison to the input gimbal excitation. The applied angular velocity of the gimbal and the output angular velocity of the ship are out of phase by π. To demonstrate the use of the stabilizers, we will prescribe an external moment on the ship, $M_e = 1e5\cos((2\pi/T)t)$. Shown below in Fig. 10, without turning the rotor on, are the three components of the angular velocity vector that result when M_e is precribed. The same system parameters introduced above are also used to produce the results below.

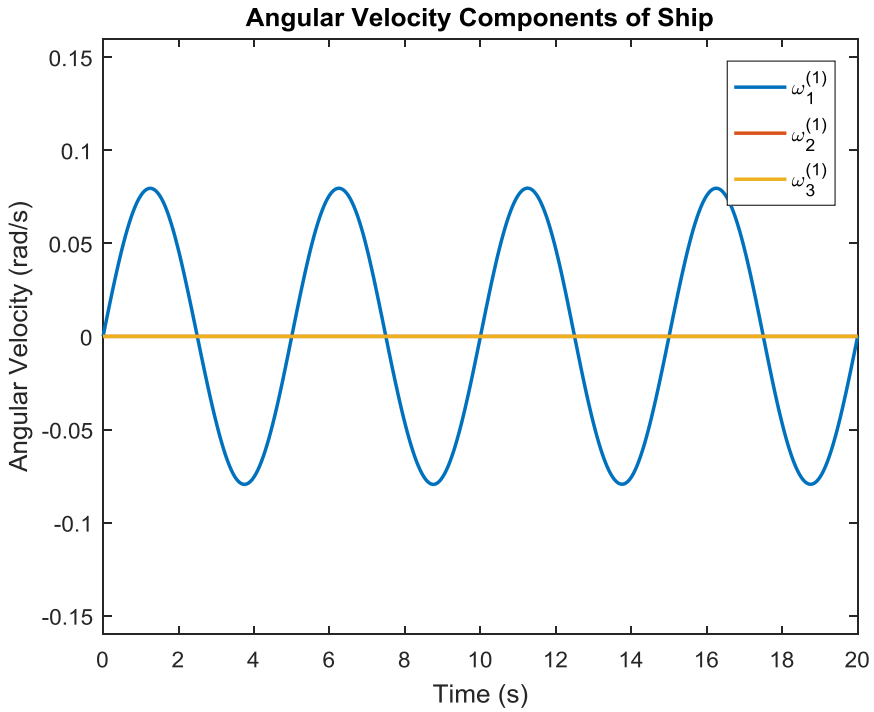

Figure 3-10: Angular velocity components due to an external moment without the use of the stabilizer

For the stabilizer to eliminate the roll, the period of both the gimbal excitation and the external moment will be made the same. In Fig. 11, we show the effect of increasing

the amplitude of oscillation from $a = \pi/10$ to $a = \pi/3.6$ on the output angular velocity components. As can be seen, as we turn on the rotor and increase the amplitude of oscillation, the output angular velocity of the ship decreases, but is not eliminated. Thus, for certain external moments that act on the ship, varying the amplitude alone may not always reduce roll to the extent needed. Other factors, such as the RPM and mass moment of inertia of the rotor, play important factors in the design of a stabilizer for various vessel sizes and wave conditions.

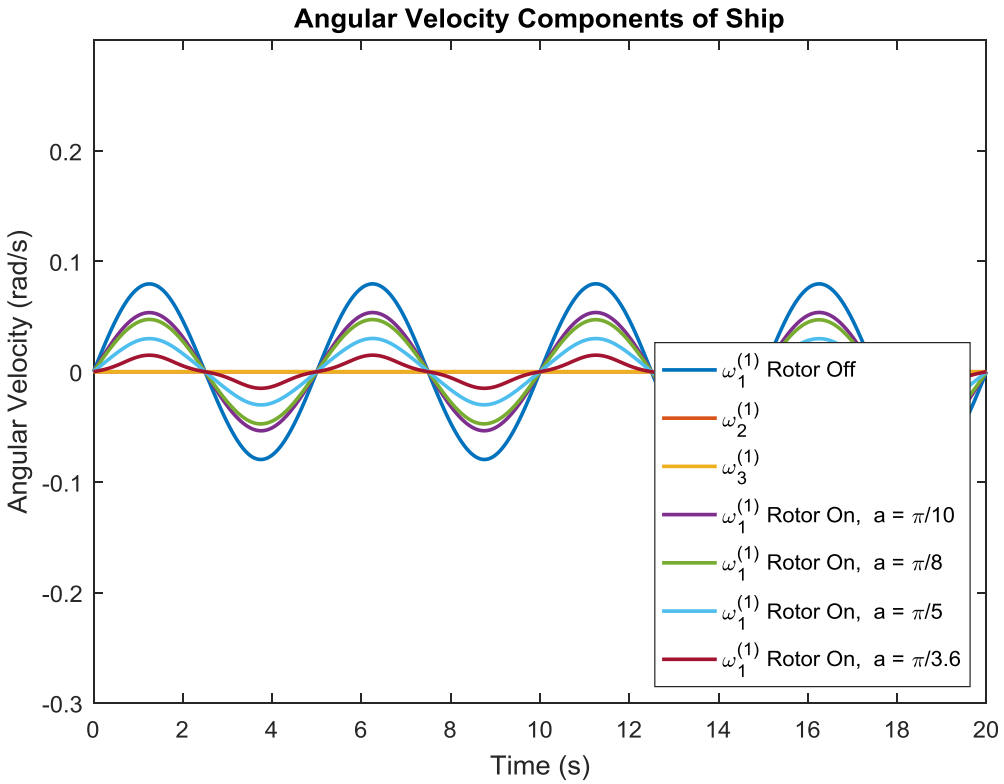

Figure 3-11: Angular velocity components with the rotor off and with the rotor on while sinusoidally oscillating at various amplitudes to demonstrates the effect of the stabilizer

In the following section, further attention is placed on the sinusoidal excitation method and the effect of the system parameters and excitation terms.

3.3.4.2 Effect of Parameters on Output Angular Velocity

Of interest is the effect of the system parameters on the output amplitude, angular velocity, and angular acceleration imposed by the gyroscopes on the ship to optimize the gyroscope design. Specifically, the effect of the mass properties are of importance in the design of the gyroscopic stabilizer.

To observe the effect of the rotor inertia and the period and amplitude of the gimbal excitation, the equations of motion will be numerically solved without the presence of ocean induced moments and other terms such as the added mass moment of inertia. Furthermore, a sinusoidal method of excitation will be employed. The moment of inertia of the rotor, $J_3^{(3)}$, is varied and visualized in the non-dimensional plot below as the gimbal is rocked at varying amplitudes. As shown in Fig. 12, the x-axis is the ratio between the mass moment of inertia of the rotor and the ship and the y-axis is the ratio between the output magnitude of the angular velocity of the ship and the input angular velocity of the rotor. The plot clearly shows a linear relationship between the two ratios and indicates that an increase in the mass moment of inertia of the rotor leads to a linear increase in the possible maximum angular velocity. While, presumably, the mass moment of inertia of the rotor cannot be adjusted after the stabilizer is assembled, the figure provides the user details regarding the speed and oscillating amplitude required to counter the excitation moment. The figure can also serve as an aid for selecting the motors to power the rotor and the gimbal for the desired angular velocity and the resulting angular acceleration and torque. Note, since the angular velocity output is a sinusoidal function, the angular acceleration can be computed by multiplying the maximum angular velocity by the angular frequency. Also to note, Fig. 12 does not include changes in the period simply because the

oscillating frequency has no effect on the maximum angular velocity of the ship. It will, on the other hand, affect the angular acceleration and angular displacement. If angular displacement is desired, the user can simply divide the maximum angular velocity by the angular frequency of excitation.

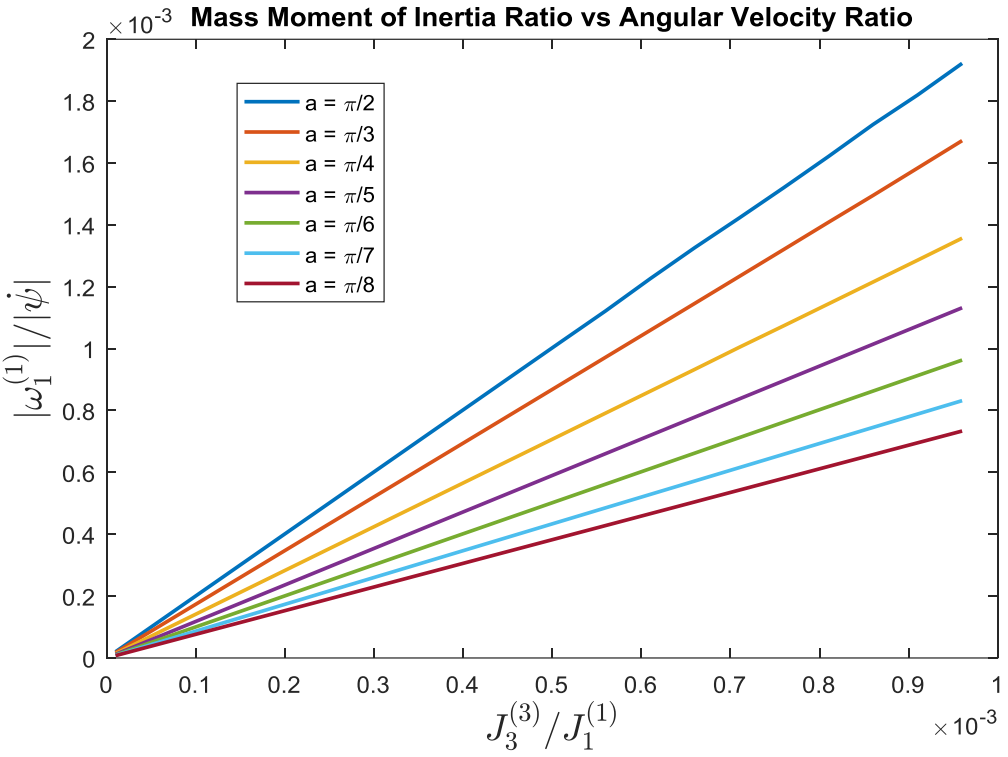

Figure 3-12: Mass moment of inertia ratio of the rotor and ship vs the angular velocity ratio of the ship and rotor while varying the amplitude of oscillation

The sensitivity of the angular velocity of the ship, or the change in slope of the above plot, when varying the amplitude of oscillation is shown below in Fig. 13. A sinusoidal function, $f(a) = 2.003\sin(1.002 * a)$, was used to fit the change in slope as the amplitude of oscillation was varied from 0 to $\pi/2$ radians. Due to the sinusoidal fit, we know that at small amplitudes of oscillation, the angular velocity of the ship will linearly

increase when increasing the angle of the gimbal excitation and level off as it reaches a value of $\pi/2$.

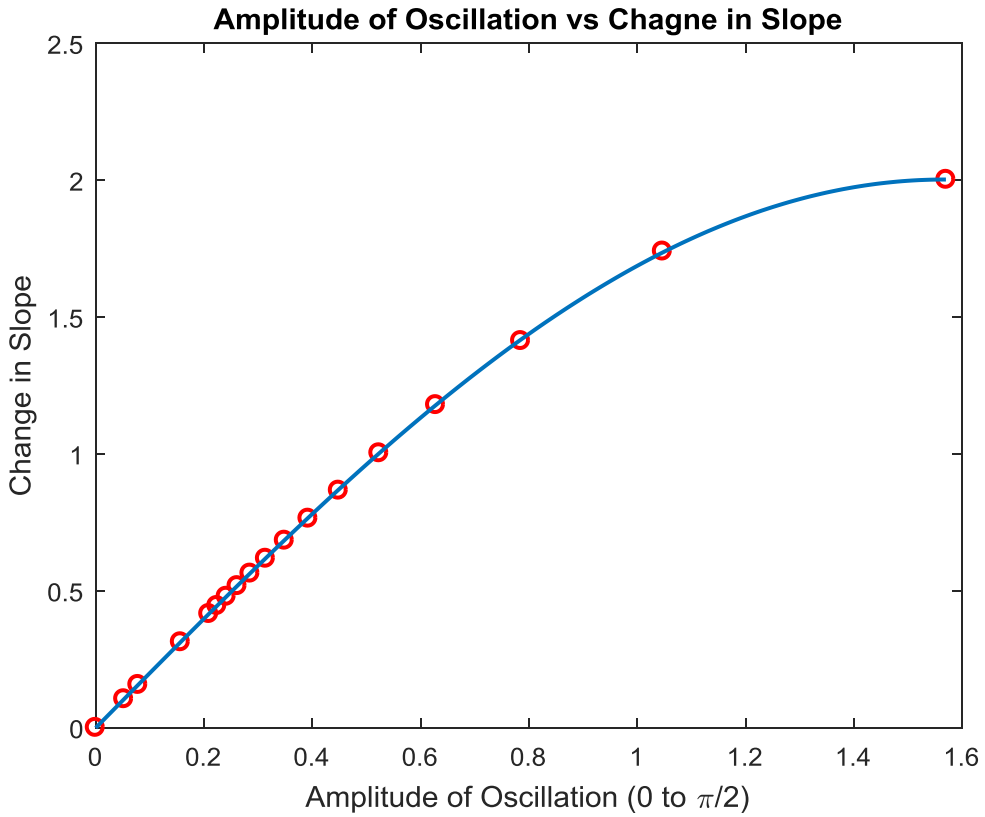

Figure 3-13: Sensitivity of the ships angular velocity to changes in the amplitude of oscillation

To see the overall effect of the period or frequency of oscillation on the output angular displacement, all parameters will be held constant as the excitation period is varied. As shown below in Fig. 14, as the period of excitation increases, a linear increase in the output angular displacement is observed. Note however, the righting moment has not been taken into account.

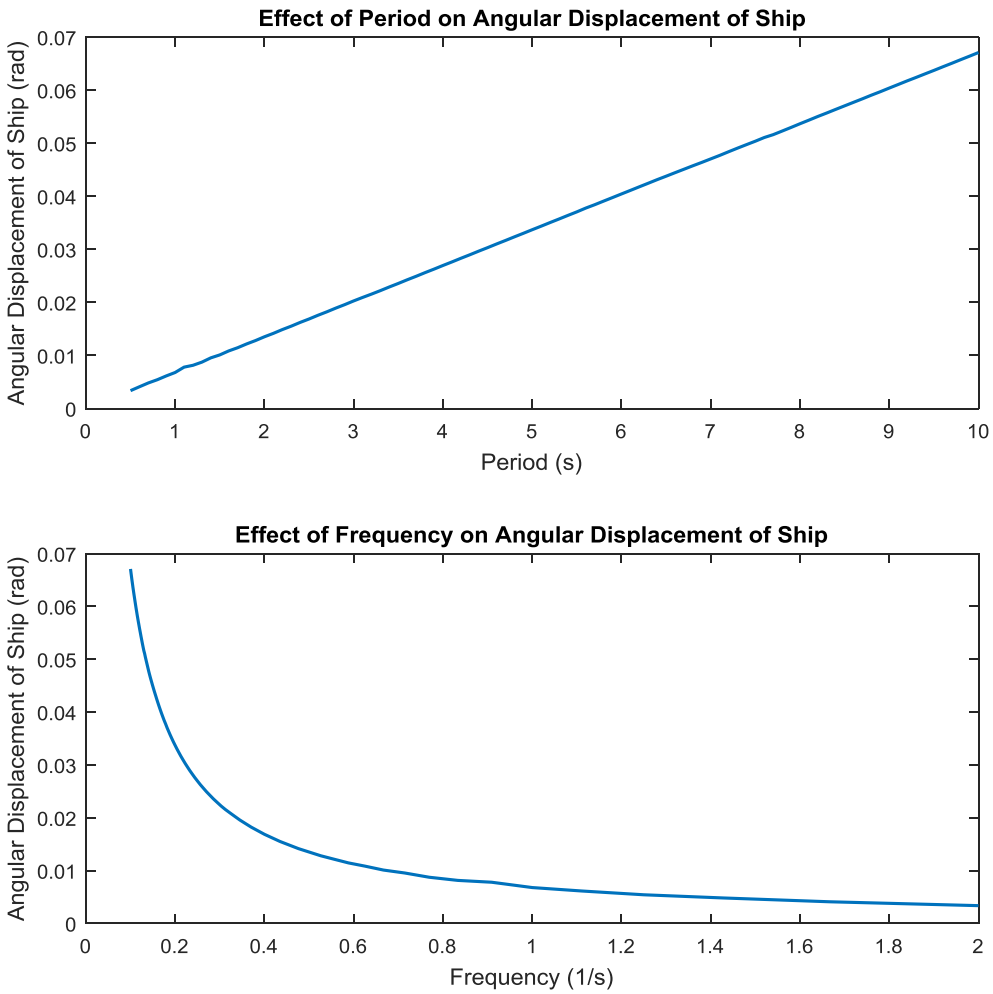

Figure 3-14: Effect of exciting period and frequency on the output angular displacement

Figure 15 below demonstrates the effect of the period and frequency on the output angular acceleration, from which the magnitude of the output torque by the gyroscopic stabilizer onto the ship can be obtained by simply multiplying the angular acceleration by the mass moment of inertia along the axis. It can also be noted that the system's acceleration is very sensitive when applying a small period of oscillation.

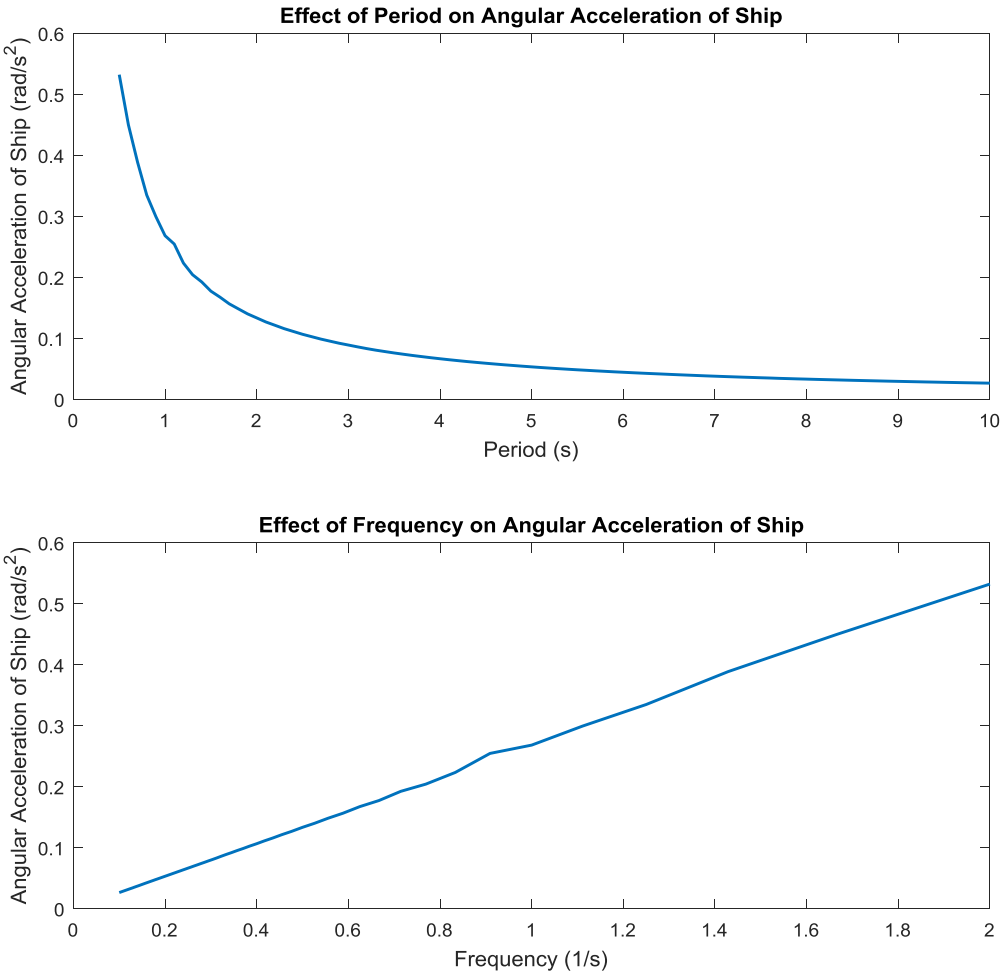

Figure 3-15: Effect of exciting period and frequency on the output angular acceleration

From the above figure, since all other parameters were kept constant including the amplitude of oscillation, we observe an exponentially decaying angular acceleration around the $\mathbf{e}_1^{(1)}(t)$ axis as the period increases. Therefore, as expected, large torques are produced when exciting the gimbal at faster rates.

3.4 Concluding Remarks

In this chapter, the modeling of two gyroscopic multibody systems, including a gyroscopic ocean wave energy converter and a gyroscopic roll stabilizer, has been

completed. The mathematical model of the GOWEC has been derived using the moving frame method, allowing for a systematic approach in deriving the kinematics of the system. The equation of motion derived was then used to obtain an expression for the average power output. To maximize the power output of the GOWEC, it was found that the gimbal motion, ,has to be matched with that of the incoming wave. The maximum power output was shown to greatly depend on the frequency and amplitude of oscillation and can greatly decrease with any changes in the incoming wave direction and frequency. Lastly, an estimate of the electrical power output using off-the-shelf gyroscopic stabilizers produced by Seakeeper is reported.

As a natural extension of the GOWEC, a general mathematical model of a marine vessel installed with dual gyroscopes was developed using the moving frame method. In addition, both continuous and sinusoidal methods of excitation have been discussed and shown to produce similar output results on the ship. Furthermore, the systems parameters have been characterized and their effect on the output angular velocity and displacement have been analyzed.

Chapter 3, in part, is published as "A Mathematical Model for a Gyroscopic Ocean-Wave Energy Converter." Proceedings of the ASME 2013 International Mechanical Engineering Congress & Exposition. Paper: IMECE2013-62834. ASME, New York. This work was coauthored by H. Murakami. The dissertation author is the second author of this work.

Chapter 3, in part, is published as "A Mathematical Model with Preliminary Experiments of a Gyroscopic Ocean Wave Energy Converter." Proceedings of the ASME 2015 International Mechanical Engineering Congress & Exposition. Paper: IMECE2015-

51163. ASME, New York. This work was coauthored by H. Murakami, and A. Amini. The dissertation author is the second author of this work.

Chapter 3, in part, is published as "A Mathematical Model of an Active Gyroscopic Roll Stabilizer Using the Moving Frame Method." Proceedings of the ASME 2015 International Mechanical Engineering Congress & Exposition. Paper: IMECE2015-51157. ASME, New York. This work was coauthored by H. Murakami. The dissertation author is the first author of this work.

3.5 Appendix

3.5.1 Gyroscopic Roll Stabilizer Matrices

Shown in this section are the matrices needed for the derivation of the equations of motion of a ship (or any marine vessel/platform) installed with dual gyroscopic stabilizers with one operating in the opposite direction. The $[B(t)]$ matrix shown below, relates the generalized velocities and the essential generalized velocities.

$$[B(t)] = \begin{bmatrix} I_3 & 0_3 & 0_1 & 0_1 \\ 0_3 & I_3 & 0_1 & 0_1 \\ I_3 & R^{(1)}\left(\overleftarrow{s_c^{(2/1)}}\right)^T & 0_1 & 0_1 \\ 0_3 & \left(R_2^{(2/1)}(\varphi^{(2)})\right)^T & \mathrm{e}_2 & 0_1 \\ I_3 & R^{(1)}\left(\overleftarrow{s_c^{(2/1)}}\right)^T & 0_1 & 0_1 \\ 0_3 & \left(R^{(3/1)}\right)^T & \left(R_3^{(3/2)}\left(\psi^{(3)}\right)\right)^T \mathrm{e}_2 & \mathrm{e}_3 \\ I_3 & R^{(1)}\left(\overleftarrow{s_c^{(4/1)}}\right)^T & 0_1 & 0_1 \\ 0_3 & \left(R_2^{(4/1)}(-\varphi^{(2)})\right)^T & -\mathrm{e}_2 & 0_1 \\ I_3 & R^{(1)}\left(\overleftarrow{s_c^{(4/1)}}\right)^T & 0_1 & 0_1 \\ 0_3 & \left(R^{(5/1)}\right)^T & -\left(R_3^{(5/4)}\left(\psi^{(5)}\right)\right)^T \mathrm{e}_2 & -\mathrm{e}_3 \end{bmatrix} \tag{120}$$

In the above matrix, the notation can be defined as follows:

$$I_3 = \begin{bmatrix} 1 & 0 & 0 \\ 0 & 1 & 0 \\ 0 & 0 & 1 \end{bmatrix}, 0_3 = \begin{bmatrix} 0 & 0 & 0 \\ 0 & 0 & 0 \\ 0 & 0 & 0 \end{bmatrix}, 0_1 = \begin{bmatrix} 0 \\ 0 \\ 0 \end{bmatrix}$$

The rotation matrices, $R^{(3/1)}$ and $R^{(5/1)}$ are defined below as the sequence of rotations:

$$R^{(3/1)} = R_2^{(2/1)}\left(\varphi^{(2)}\right) R_3^{(3/2)}\left(\psi^{(3)}\right)$$

$$R^{(5/1)} = R_2^{(4/1)}\left(-\varphi^{(2)}\right) R_3^{(5/4)}\left(-\psi^{(3)}\right)$$

The mass matrix $[M]$ is defined below along with the submatrices:

$$[M] = \begin{bmatrix} m^{(1)}I_3 & 0_3 & 0_3 & 0_3 & 0_3 & 0_3 & 0_3 & 0_3 & 0_3 & 0_3 \\ 0_3 & J_C^{(1)} & 0_3 & 0_3 & 0_3 & 0_3 & 0_3 & 0_3 & 0_3 & 0_3 \\ 0_3 & 0_3 & m^{(2)}I_3 & 0_3 & 0_3 & 0_3 & 0_3 & 0_3 & 0_3 & 0_3 \\ 0_3 & 0_3 & 0_3 & J_C^{(2)} & 0_3 & 0_3 & 0_3 & 0_3 & 0_3 & 0_3 \\ 0_3 & 0_3 & 0_3 & 0_3 & m^{(3)}I_3 & 0_3 & 0_3 & 0_3 & 0_3 & 0_3 \\ 0_3 & 0_3 & 0_3 & 0_3 & 0_3 & J_C^{(3)} & 0_3 & 0_3 & 0_3 & 0_3 \\ 0_3 & 0_3 & 0_3 & 0_3 & 0_3 & 0_3 & m^{(4)}I_3 & 0_3 & 0_3 & 0_3 \\ 0_3 & 0_3 & 0_3 & 0_3 & 0_3 & 0_3 & 0_3 & J_C^{(4)} & 0_3 & 0_3 \\ 0_3 & 0_3 & 0_3 & 0_3 & 0_3 & 0_3 & 0_3 & 0_3 & m^{(5)}I_3 & 0_3 \\ 0_3 & 0_3 & 0_3 & 0_3 & 0_3 & 0_3 & 0_3 & 0_3 & 0_3 & J_C^{(5)} \end{bmatrix} \quad (121)$$

where $J_C^{(2)} = J_C^{(4)}$, $J_C^{(3)} = J_C^{(5)}$, $m^{(3)} = m^{(5)}$, and $m^{(2)} = m^{(4)}$ if both gyroscopes used are the same.

The skew-symmetric matrix, $[D(t)]$, containing the skew-symmetric angular velocity matrices and used in the variation of the angular velocities is shown below:

$$[D(t)] = \begin{bmatrix} 0_3 & 0_3 & 0_3 & 0_3 & 0_3 & 0_3 & 0_3 & 0_3 & 0_3 & 0_3 \\ 0_3 & \overleftrightarrow{\omega^{(1)}(t)} & 0_3 & 0_3 & 0_3 & 0_3 & 0_3 & 0_3 & 0_3 & 0_3 \\ 0_3 & 0_3 & 0_3 & 0_3 & 0_3 & 0_3 & 0_3 & 0_3 & 0_3 & 0_3 \\ 0_3 & 0_3 & 0_3 & \overleftrightarrow{\omega^{(2)}(t)} & 0_3 & 0_3 & 0_3 & 0_3 & 0_3 & 0_3 \\ 0_3 & 0_3 & 0_3 & 0_3 & 0_3 & 0_3 & 0_3 & 0_3 & 0_3 & 0_3 \\ 0_3 & 0_3 & 0_3 & 0_3 & 0_3 & \overleftrightarrow{\omega^{(3)}(t)} & 0_3 & 0_3 & 0_3 & 0_3 \\ 0_3 & 0_3 & 0_3 & 0_3 & 0_3 & 0_3 & 0_3 & 0_3 & 0_3 & 0_3 \\ 0_3 & 0_3 & 0_3 & 0_3 & 0_3 & 0_3 & 0_3 & \overleftrightarrow{\omega^{(4)}(t)} & 0_3 & 0_3 \\ 0_3 & 0_3 & 0_3 & 0_3 & 0_3 & 0_3 & 0_3 & 0_3 & 0_3 & 0_3 \\ 0_3 & 0_3 & 0_3 & 0_3 & 0_3 & 0_3 & 0_3 & 0_3 & 0_3 & \overleftrightarrow{\omega^{(5)}(t)} \end{bmatrix} \quad (122)$$

3.5.2 Equations of Motion of a Ship Installed with Dual Gyroscopes

The rotational equations of motion for a ship installed with two gyroscopic stabilizers are listed below. Highlighted terms include contributions from the rotation of the rotor. The equations, for simplicity, assume the ship does not translate, thin disk rotors, and fully symmetric gimbals.

Equation of Motion: Roll

$$\dot{\omega}_1^{(1)}(t)\left(J_1^{(1)} + 2J_2^{(2)} + J_3^{(3)}\right) + \omega_2^{(1)}\omega_3^{(1)}\left(-J_2^{(1)} + J_3^{(1)} + \frac{J_3^{(3)}}{2} + \frac{J_3^{(3)}\cos\left(2\varphi^{(2)}(t)\right)}{2}\right) + \omega_1^{(1)}J_3^{(3)}\dot{\varphi}^{(2)}(t)\sin\left(2\varphi^{(2)}(t)\right) = M_1^{(w)} - 2J_3^{(3)}\dot{\psi}\dot{\varphi}^{(2)}(t)\cos\left(\varphi^{(2)}(t)\right) \quad (123)$$

Equation of Motion: Pitch

$$\dot{\omega}_2^{(1)}(t)\left(J_2^{(1)} + 2J_2^{(2)} + J_3^{(3)}\right) + \omega_1^{(1)}\omega_3^{(1)}\left(J_1^{(1)} - J_3^{(1)} - J_3^{(3)} + 2J_3^{(3)}\sin^2\left(\phi^{(2)}(t)\right)\right) + 2\omega_3^{(1)}J_3^{(3)}\dot{\psi}\sin\left(\varphi^{(2)}(t)\right) = M_2^{(w)} \quad (124)$$

Equation of Motion: Yaw

$$\dot{\omega}_3^{(1)}(t)\left(J_3^{(1)} + 2J_2^{(2)} + \frac{3J_3^{(3)}}{2} + \frac{J_3^{(3)}\cos\left(2\phi^{(2)}(t)\right)}{2}\right) + \omega_1^{(1)}\omega_2^{(1)}\left(-J_1^{(1)} + J_2^{(1)} - \frac{J_3^{(3)}}{2} + \frac{J_3^{(3)}\cos\left(2\phi^{(2)}(t)\right)}{2}\right) - 2\omega_2^{(1)}J_3^{(3)}\dot{\psi}\sin\left(\phi^{(2)}(t)\right) - \omega_3^{(1)}J_3^{(3)}\dot{\phi}^{(2)}(t)\sin\left(2\phi^{(2)}(t)\right) = M_3^{(w)} \quad (125)$$

To note in the above equations, the rotation of the rotor only appears as an excitation term in the roll equation. In the remaining equations, it appears in the coupled terms which are equal but opposite in sign.

3.5.3 Equations of Motion of a Ship Installed with a Single Gyroscope

The rotational equations of motion of a ship installed with a single gyroscope are listed below. are expressed below. Highlighted terms include contributions from the rotation of the rotor. The equations, for simplicity, assume the ship does not translate, thin disk rotors, and fully symmetric gimbals.

Equation of Motion: Roll

$$\dot{\omega}_1^{(1)}(t)\left(J_1^{(1)}+J_2^{(2)}+\frac{3J_3^{(3)}}{4}-\frac{J_3^{(3)}\cos\left(2\varphi^{(2)}(t)\right)}{4}\right)+\dot{\omega}_3^{(1)}(t)\frac{J_3^{(3)}\sin\left(2\varphi^{(2)}(t)\right)}{4}+$$
$$\omega_1^{(1)}\frac{J_3^{(3)}\dot{\varphi}^{(2)}(t)\sin\left(2\varphi^{(2)}(t)\right)}{2}+\omega_2^{(1)}J_3^{(3)}\dot{\psi}\cos\left(\varphi^{(2)}(t)\right)+\omega_3^{(1)}\dot{\varphi}^{(2)}(t)\left(-2J_2^{(2)}-\frac{J_3^{(3)}}{2}+\right.$$
$$\left.\frac{J_3^{(3)}\cos\left(2\varphi^{(2)}(t)\right)}{4}\right)+\omega_2^{(1)}\omega_3^{(1)}\left(-J_2^{(1)}+J_3^{(1)}+\frac{J_3^{(3)}}{4}+\frac{J_3^{(3)}\cos\left(2\varphi^{(2)}(t)\right)}{4}\right)+$$
$$\omega_1^{(1)}\omega_2^{(1)}\frac{J_3^{(3)}\sin\left(2\varphi^{(2)}(t)\right)}{4}=M_1^{(w)}-J_3^{(3)}\dot{\psi}\dot{\varphi}^{(2)}(t)\cos\left(\varphi^{(2)}(t)\right) \qquad (126)$$

Equation of Motion: Pitch

$$\dot{\omega}_2^{(1)}(t)\left(J_2^{(1)}+J_2^{(2)}+\frac{J_3^{(3)}}{2}\right)+\ddot{\varphi}(t)\left(J_3^{(2)}+\frac{J_3^{(3)}}{2}\right)-\left(\omega_1^{(1)}\right)^2\left(\frac{J_3^{(3)}\sin\left(2\varphi^{(2)}(t)\right)}{4}\right)+$$
$$\left(\omega_3^{(1)}\right)^2\left(\frac{J_3^{(3)}\sin\left(2\varphi^{(2)}(t)\right)}{4}\right)-\omega_1^{(1)}J_3^{(3)}\dot{\psi}\cos\left(\varphi^{(2)}(t)\right)+\omega_3^{(1)}J_3^{(3)}\dot{\psi}\sin\left(\varphi^{(2)}(t)\right)+$$
$$\omega_1^{(1)}\omega_3^{(1)}\left(J_1^{(1)}-J_3^{(1)}-\frac{J_3^{(3)}\cos\left(2\phi^{(2)}(t)\right)}{2}\right)=M_2^{(w)} \qquad (127)$$

Equation of Motion: Yaw

$$\dot{\omega}_3^{(1)}(t)\left(J_3^{(1)}+J_2^{(2)}+\frac{3J_3^{(3)}}{4}+\frac{J_3^{(3)}\cos\left(2\phi^{(2)}(t)\right)}{4}\right)+\dot{\omega}_1^{(1)}(t)\frac{J_3^{(3)}\sin\left(2\phi^{(2)}(t)\right)}{4}+$$
$$\omega_1^{(1)}\left(2J_2^{(2)}\dot{\phi}^{(2)}(t)+\frac{J_3^{(3)}\dot{\phi}^{(2)}(t)}{2}+\frac{J_3^{(3)}\dot{\phi}^{(2)}(t)\cos\left(2\phi^{(2)}(t)\right)}{4}\right)-\omega_2^{(1)}J_3^{(3)}\dot{\psi}\sin\left(\phi^{(2)}(t)\right)-$$

$$\omega_3^{(1)}\frac{J_3^{(3)}\dot{\phi}^{(2)}(t)\sin\left(2\phi^{(2)}(t)\right)}{2}+\omega_1^{(1)}\omega_2^{(1)}\left(-J_1^{(1)}+J_2^{(1)}-\frac{J_3^{(3)}}{4}+\frac{J_3^{(3)}\cos\left(2\phi^{(2)}(t)\right)}{4}\right)-$$
$$\frac{J_3^{(3)}\sin\left(2\phi^{(2)}(t)\right)}{4}\omega_2^{(1)}\omega_3^{(1)}=M_3^{(w)}+J_3^{(3)}\dot{\psi}\dot{\phi}^{(2)}(t)\sin\left(\phi^{(2)}(t)\right) \quad (128)$$

Note, the major difference between the single and dual gyroscope configurations is the coupling of the accelerations terms in the equations of motion. In other words, $\dot{\omega}_3^{(1)}(t)$ and $\dot{\omega}_1^{(1)}(t)$ appear in both the roll and yaw equations of motion. Thus, to solve the equations numerically, the yaw equation of motion must be substituted into the roll equation of motion and vice versa.

3.6 References

[1] Murakami, H., 2013, November. A Moving Frame Method for Multi-Body Dynamics. In *ASME 2013 International Mechanical Engineering Congress and Exposition*. American Society of Mechanical Engineers.

[2] Murakami, H., 2015, November. A Moving Frame Method for Multi-Body Dynamics Using SE (3). In *ASME 2015 International Mechanical Engineering Congress and Exposition*. American Society of Mechanical Engineers.

[3] Jacobson, P.T., Hagerman, G. and Scott, G., 2011. *Mapping and assessment of the United States ocean wave energy resource* (No. DOE/GO/18173-1). Electric Power Research Institute.

[4] "Home". 2016. *Ocean Power Technologies*. http://www.oceanpowertechnologies.com/.

[5] "Pelamis, World'S First Commercial Wave Energy Project, Agucadoura". 2016. *Power Technology*. http://www.power-technology.com/projects/pelamis/.

[6] Goldin, A., 2004. Autonomous Gyroscopic Ocean-Wave Powered Generator: Invention of a New Energy Conversion Technology. www.siemensfoundation.org/en/competition/ 2004-winners/aaron_goldin.htm.

[7] Bracco, G., Giorcelli, E. and Mattiazzo, G., 2011. ISWEC: A gyroscopic mechanism for wave power exploitation. *Mechanism and machine theory*, *46*(10), pp.1411-1424.

[8] Bracco, G., Giorcelli, E., Mattiazzo, G., Pastorelli, M. and Taylor, J., 2009, June. ISWEC: design of a prototype model with gyroscope. In *Clean Electrical Power, 2009 International Conference on* (pp. 57-63). IEEE.

[9] Kanki, H, Arii, S., Fukui, K., and Tsukuo, K., 2007. Ocean experiment of wave-power generation system by gyro effect. *Proceedings for the 2007 Japan Society of Mechanical Engineers Conference*, Suita, Japan, abstract 0511, 2 pages (in Japanese).

[10] Townsend, N.C. and Shenoi, R.A., 2013. Modelling and analysis of a single gimbal gyroscopic energy harvester. *Nonlinear Dynamics*, *72*(1-2), pp.285-300.

[11] Frankel, T., 2011. *The geometry of physics: an introduction*. Cambridge University Press.

[12] Miline-Thomson, L. M., 1968, *Theoretical Hydrodynamics*, 5th edition, McMillan Press, London.

[13] Kundu, P. J., Cohen, I. M., and Dowling, D. R., 2012, *Fluid Mechanics*, 5thedition, Academic Press, New York, Chap. 7.

[14] National Weather Service Ocean Prediction Center, http://www.opc.ncep.noaa.gov/index.php

[15] Jacobson, P., 2011, *Mapping and Assessment of the United States Ocean Wave Energy Resource*, Electric Power Research Institute (EPRI) report 1024637.

[16] Murakami H. & Rios O. 2013. "A Mathematical Model for a Gyroscopic Ocean-Wave Energy Converter." Proceedings of the ASME 2013 International Mechanical Engineering Congress & Exposition. Paper: IMECE2013-62834. ASME, New York.

[17] Falnes, J., 2002. *Ocean waves and oscillating systems: linear interactions including wave-energy extraction*. Cambridge university press.

[18] "Technology | Seakeeper". 2016. *Seakeeper*. https://seakeeper.com/technology/.

[19] Forbes, T., 1904,"Device for Steadying Ships", U.S. Patent No. 769,693.

[20] Schlick, E., 1904, "Device for Minimizing the Oscillatory Movements of Ships," U.S. Patent No. 769,493. 11 Copyright © 2015 by ASME

[21] Sperry, E., 1910, "The Gyroscope for Marine Purposes," Soc. Nav. Archit.Mar. Eng., Trans., 18, pp. 143–154.

[22] Townsend, N., Murphy, A., and Shenoi, R., "A new active gyro stabilizer system for ride control of marine vehicles," *Ocean Engineering*, vol. 34 no. 11-12, pp. 1607-1617, 2007.

[23] Newman, J.N., 1977. *Marine hydrodynamics*. MIT press.

CHAPTER 4: MODELING OF FLEXIBLE AND SOFT ROBOTS

4.1 Introduction

Flexibility of robots enables new modes of locomotion. Inch-worms, snakes, and eels for example possess agile capabilities allowing them to interact and maneuver in their respective environments. Flexible and soft robots have also proven to withstand many dangerous elements and scenarios that would otherwise lead to mechanical failure in traditional robots [1-2]. They have also shown the ability to grasp oblique or delicate objects that would otherwise pose problems to traditional robots [3]. Such features make flexible or soft robotics a very interesting field with a wide variety of applications in many engineering sectors. In this paper, we focus on developing active mechanical models to aid in the modeling and design of flexible or soft robots.

Using mechanical models, the internal actuation necessary for the flexible robot to duplicate the motion of a biological creature will be determined quantitatively. In addition, the flexibility of robots indicates the existence of restoring or elastic deformation. With mechanical models, it will become possible to optimize the usage of elastic deformation to achieve desired motions of flexible robots.

In this chapter, the mechanical models for slender, flexible robots are developed to quantitatively describe the internal actuation needed to duplicate the target mimicking motions of creatures. To this end, two models are developed: (i) a multi-body model consisting of discrete, jointed cylindrical segments with torsional springs, capable of modeling the snake robots by Hirose [4], and Saito et al. [5], and (ii) a continuous beam model with internal actuation. The latter model offers the limit for the discrete models as

the number of jointed segments increases. In addition, the continuous beam enables the utilization of available fluid-beam interaction, computed by G. I. Taylor [6].

The models can simulate the deformation of passive flexible slender bodies as well as the deformation induced by internal actuation. The two models will be presented in what follows and will then be applied to simulate the motion of an inchworm.

4.2 A Multi-Link Model with Elastic Springs

We first consider a jointed multi-link system consisting of identical links as shown in Fig. 1. Each joint has an elastic torsional spring with spring constant k as well as a motor. As shown in Fig.1, each link of length l has mass m with the center of mass, point C, at the center of the link, and a mass moment of inertia J_c. We employ the compact notation, introduced by Élie Cartan (1869-1951) in modern differential geometry, and presented by Frankel [7]. In rigid body dynamics, the use of the moving frames with Frankel's compact notation facilitates clear and simple kinematic computations [8].

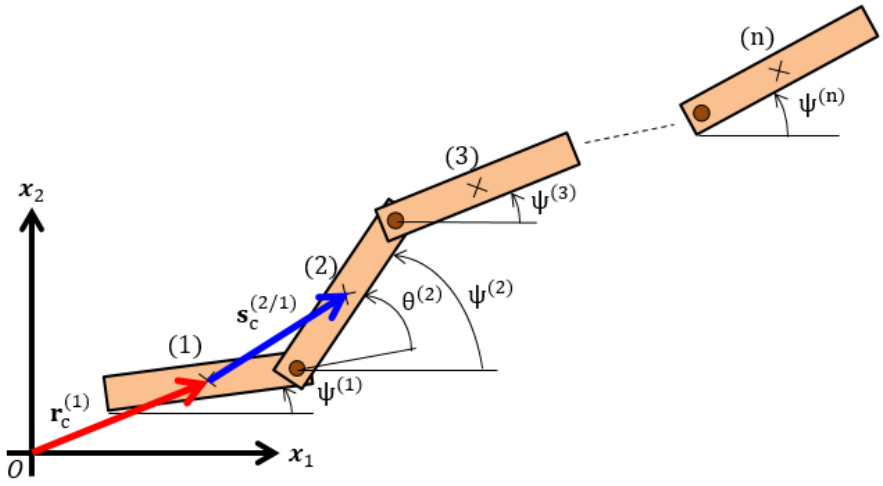

Figure 4-1: Discrete multi-link model for (n) number of links

4.2.1 Kinematic Description of a Linked System

The motion of a linked body takes place in a plane, spanned by a Cartesian coordinate system $\{x_1 \quad x_2\}$. The unit coordinate vectors of the x_1- and x_2-axes define the vector basis: $\mathbf{e}^I = (\mathbf{e}_1^I \quad \mathbf{e}_2^I)$, which is referred to as the *inertial vector basis*. Starting from the head link along the chain, link numbers are assigned starting from one. To identify a variable belonging to link-α, we use a superscript of the link number surrounded by a pair of parentheses as (α). For example, the center of mass C of link-α is expressed as $C^{(\alpha)}$.

Next a Cartesian coordinate system $\{s_1 \quad s_2\}$ with the origin at the center of mass C is attached. The s_1-axis is selected along the axis of the link and points in the direction of the increasing link number. For example, at the center of mass $C^{(\alpha)}$of link (α), the link-α Cartesian coordinate system $\{s_1^{(\alpha)} \quad s_2^{(\alpha)}\}$ is attached. Similarly, at the center of mass $C^{(\alpha+1)}$, the link-$(\alpha+1)$ coordinate system $\left\{s_1^{(\alpha+1)} \quad s_2^{(\alpha+1)}\right\}$. The $s_1^{(\alpha)}$-axis points in the distal direction of link-$(\alpha+1)$.

For each link-attached coordinate system, we define a *moving frame*, consisting of the vector basis $\mathbf{e}(t)$ and the position vector to the origin of the coordinate system, $\mathbf{r}_c(t)$. For example, for link-α, the moving frame is written as $\left(\mathbf{e}^{(\alpha)}(t) \quad \mathbf{r}_c^{(\alpha)}(t)\right)$, while for link-$(\alpha+1)$, the moving frame is expressed as $\left(\mathbf{e}^{(\alpha+1)}(t) \quad \mathbf{r}_c^{(\alpha+1)}(t)\right)$. The vector basis $\mathbf{e}^{(\alpha)}(t) = \left(\mathbf{e}_1^{(\alpha)}(t) \quad \mathbf{e}_2^{(\alpha)}(t)\right)$ consists of unit coordinate vectors of the $s_1^{(\alpha)}$-axes and $s_2^{(\alpha)}$-axes. To express moving frames with the inertial coordinate system, the *inertial frame* is defined as $(\mathbf{e}^I \quad \mathbf{0})$ where the origin of the inertial frame is expressed by the zero position-vector, $\mathbf{0}$. The moving frame of link-α is defined with respect to the inertial frame by

defining the inertial coordinates of the origin $C^{(\alpha)}$ and the attitude relation of $\mathbf{e}^{(\alpha)}(t)$measured from $\mathbf{e}^{I}$.

First, the position vector of $C^{(\alpha)}$ is expressed as:

$$\mathbf{r}_{\mathrm{c}}^{(\alpha)}(\mathrm{t}) = \mathbf{e}^{I} x_{c}^{(\alpha)}(t) = (\mathbf{e}_1^{I} \quad \mathbf{e}_2^{I}) \begin{pmatrix} x_{1c}^{(\alpha)}(t) \\ x_{2c}^{(\alpha)}(t) \end{pmatrix}, \tag{1}$$

where the compact notation $\mathbf{e}^{I}$ expresses a 1×2 row matrix of inertial vector basis $(\mathbf{e}_1^{I} \quad \mathbf{e}_2^{I})$, and $x_{c}^{(\alpha)}(t)$ denotes a 2×1 column matrix of the coordinates of $C^{(\alpha)}$.

Second, let the angle between the $s_1^{(\alpha)}$-axis and the x_1-axis, measured in the counterclockwise direction from the x_1-axis, be expressed as $\psi^{(\alpha)}(t)$. The *attitude* of $\mathbf{e}^{(\alpha)}(t)$ measured from $\mathbf{e}^{I}$ is expressed by a 2×2 *frame rotation matrix* $R^{(\alpha)}(t)$ as:

$$\mathbf{e}^{(\alpha)}(t) = \mathbf{e}^{I} R^{(\alpha)}(t) = \mathbf{e}^{I} \begin{bmatrix} \cos\psi^{(\alpha)}(t) & -\sin\psi^{(\alpha)}(t) \\ \sin\psi^{(\alpha)}(t) & \cos\psi^{(\alpha)}(t) \end{bmatrix}. \tag{2}$$

Now, the link-α moving frame is expressed by the inertial frame using a 3×3 *frame connection matrix* $E^{(\alpha)}(t)$, which includes both the frame rotation matrix $R^{(\alpha)}(t)$ and the inertial coordinate $x_{c}^{(\alpha)}(t)$ of the origin of the frame:

$$\left(\mathbf{e}^{(\alpha)}(t) \quad \mathbf{r}_{c}^{(\alpha)}(t)\right) = (\mathbf{e}^{I} \quad \mathbf{0}) E^{(\alpha)}(t) = (\mathbf{e}^{I} \quad \mathbf{0}) \begin{bmatrix} R^{(\alpha)} & x_{c}^{(\alpha)}(t) \\ 0_1^{T} & 1 \end{bmatrix}, \tag{3a}$$

where $0_1^{T} = (0 \quad 0)$ and

$$E^{(\alpha)}(t) = \begin{bmatrix} \cos\psi^{(\alpha)}(t) & -\sin\psi^{(\alpha)}(t) & x_{1c}^{(\alpha)}(t) \\ \sin\psi^{(\alpha)}(t) & \cos\psi^{(\alpha)}(t) & x_{2c}^{(\alpha)}(t) \\ 0 & 0 & 1 \end{bmatrix}. \tag{3b}$$

Similarly, the link-$(\alpha+1)$ moving frame is expressed by the inertial frame as:

$$\left(\mathbf{e}^{(\alpha+1)}(t) \quad \mathbf{r}_{c}^{(\alpha+1)}(t)\right) = (\mathbf{e}^{I} \quad \mathbf{0}) E^{(\alpha+1)}(t)$$

$$= (\mathbf{e}^I \quad \mathbf{0}) \begin{bmatrix} R^{(\alpha+1)}(t) & x_c^{(\alpha+1)}(t) \\ 0_1^T & 1 \end{bmatrix}. \tag{4}$$

To establish the connection between the link-$(\alpha+1)$ moving frame and the link-α moving frame, we first define the *relative position vector* $s_c^{(\alpha+1/\alpha)}(t)$ of the center of mass $C^{(\alpha+1)}$ of link-$(\alpha+1)$:

$$\boldsymbol{s}_c^{(\alpha+1/\alpha)}(t) = \mathbf{e}^{(\alpha)}(t) s_c^{(\alpha+1/\alpha)}(t) = \mathbf{e}^{(\alpha)}(t) \begin{pmatrix} \frac{l}{2}\left(1 + \cos\theta^{(\alpha+1)}(t)\right) \\ \frac{l}{2}\sin\theta^{(\alpha+1)}(t) \end{pmatrix}, \tag{5a}$$

where the relative rotation angle $\theta^{(\alpha+1)}(t)$ is introduced:

$$\theta^{(\alpha+1)}(t) = \psi^{(\alpha+1)}(t) - \psi^{(\alpha)}(t). \tag{5b}$$

The (absolute) position vector of the origin, $C^{(\alpha+1)}$of link-$(\alpha+1)$, is expressed as:

$$\mathbf{r}_c^{(\alpha+1)}(t) = \mathbf{r}_c^{(\alpha)}(t) + \boldsymbol{s}_c^{(\alpha+1/\alpha)}(t) = \mathbf{r}_c^{(\alpha)}(t) + \mathbf{e}^{(\alpha)}(t)\, s_c^{(\alpha+1/\alpha)}(t). \tag{6}$$

Second, we express the relative attitude of $\mathbf{e}^{(\alpha+1)}(t)$ from $\mathbf{e}^{(\alpha)}(t)$ utilizing the *relative rotation matrix* $R^{(\alpha+1)}(t)$, which is expressed by the relative rotation angle $\theta^{(\alpha+1)}(t)$, defined by Eq. (5b):

$$\mathbf{e}^{(\alpha+1)}(t) = \mathbf{e}^{(\alpha)}(t) R^{(\alpha+1)}(t) = \mathbf{e}^{(\alpha)}(t) \begin{bmatrix} \cos\theta^{(\alpha+1)}(t) & -\sin\theta^{(\alpha+1)}(t) \\ \sin\theta^{(\alpha+1)}(t) & \cos\theta^{(\alpha+1)}(t) \end{bmatrix}. \tag{7}$$

As a result, the link-$(\alpha+1)$ frame is expressed by the link-α frame by using the *relative frame-connection matrix* $E^{(\alpha+1/\alpha)}(t)$, which includes both Eqs. (6) and (7):

$$\left(\mathbf{e}^{(\alpha+1)}(t) \quad \mathbf{r}_c^{(\alpha+1)}(t)\right) = \left(\mathbf{e}^{(\alpha)}(t) \quad \mathbf{r}_c^{(\alpha)}(t)\right) E^{(\alpha+1/\alpha)}(t)$$

$$= \left(\mathbf{e}^{(\alpha)}(t) \quad \mathbf{r}_c^{(\alpha)}(t)\right) \begin{bmatrix} R^{(\alpha+1)}(t) & s_c^{(\alpha+1)}(t) \\ 0_1^T & 1 \end{bmatrix}, \tag{8a}$$

where the relative frame connection matrix is written as:

$$E^{(\alpha)}(t)=\begin{bmatrix}\cos\theta^{(\alpha+1)}(t) & -\sin\theta^{(\alpha+1)}(t) & \frac{l}{2}\left(1+\cos\theta^{(\alpha+1)}(t)\right)\\ \sin\theta^{(\alpha+1)}(t) & \cos\theta^{(\alpha+1)}(t) & \frac{l}{2}\sin\theta^{(\alpha+1)}(t)\\ 0 & 0 & 1\end{bmatrix}. \tag{8b}$$

Equations (3a), (4) and (8) yield the following recursive relation:

$$E^{(\alpha+1)}(t)=E^{(\alpha)}(t)E^{(\alpha+1/\alpha)}(t). \tag{9a}$$

Equation (9a) expressed in components, using Eqs. (3b) and (8):

$$\begin{bmatrix}\cos\psi^{(\alpha+1)}(t) & -\sin\psi^{(\alpha+1)}(t) & x_{1c}^{(\alpha+1)}(t)\\ \sin\psi^{(\alpha+1)}(t) & \cos\psi^{(\alpha+1)}(t) & x_{2c}^{(\alpha+1)}(t)\\ 0 & 0 & 1\end{bmatrix}= \tag{9b}$$

$$\begin{bmatrix}\cos\psi^{(\alpha+1)}(t) & -\sin\psi^{(\alpha+1)}(t) & x_{1c}^{(\alpha)}(t)+\frac{l}{2}\left(\cos\psi^{(\alpha)}(t)+\cos\psi^{(\alpha+1)}(t)\right)\\ \sin\psi^{(\alpha+1)}(t) & \cos\psi^{(\alpha+1)}(t) & x_{2c}^{(\alpha)}(t)+\frac{l}{2}\left(\sin\psi^{(\alpha)}(t)+\sin\psi^{(\alpha+1)}(t)\right)\\ 0 & 0 & 1\end{bmatrix}.$$

Equation (9b) gives the recursive relation for the link-$(\alpha+1)$ coordinates, $x_{1c}^{(\alpha+1)}(t)$ and $x_{2c}^{(\alpha+1)}(t)$ as:

$$x_{1c}^{(\alpha+1)}(t)=x_{1c}^{(\alpha)}(t)+\frac{l}{2}\left(\cos\psi^{(\alpha)}(t)+\cos\psi^{(\alpha+1)}(t)\right), \tag{10a}$$

$$x_{2c}^{(\alpha+1)}(t)=x_{2c}^{(\alpha)}(t)+\frac{l}{2}\left(\sin\psi^{(\alpha)}(t)+\sin\psi^{(\alpha+1)}(t)\right). \tag{10b}$$

We start from $E^{(1)}(t)$ defined in Eq. (1) for $\alpha=1$:

$$E^{(1)}(t)=\begin{bmatrix}\cos\theta^{(1)}(t) & -\sin\theta^{(1)}(t) & x_{1c}^{(1)}(t)\\ \sin\theta^{(1)}(t) & \cos\theta^{(1)}(t) & x_{2c}^{(1)}(t)\\ 0 & 0 & 1\end{bmatrix}. \tag{11}$$

and use Eq. (9a) recursively to compute $E^{(\alpha)}(t)$ for $\alpha=1,2,\cdots,n-1$. In this manner, the frame connection matrices are expressed analytically as:

$$\left(\mathbf{e}^{(\beta)}(t)\quad \mathbf{r}_c^{(\beta)}(t)\right)=(\mathbf{e}^{I}\quad \mathbf{0})E^{(\beta)}(t)\text{ for }\beta=1,2,\cdots,n, \tag{12a}$$

in which

$$E^{(\beta)}(t) = \begin{bmatrix} \cos\theta^{(\beta)}(t) & -\sin\theta^{(\beta)}(t) & x_{1c}^{(\beta)}(t) \\ \sin\theta^{(\beta)}(t) & \cos\theta^{(\beta)}(t) & x_{2c}^{(\beta)}(t) \\ 0 & 0 & 1 \end{bmatrix}. \tag{12b}$$

In Eq. (12b), $x_{1c}^{(\beta)}(t)$ and $x_{2c}^{(\beta)}(t)$ are computed recursively using Eqs. (10a, b). The results for $\beta = 2$:

$$x_{1c}^{(2)}(t) = x_{1c}^{(1)}(t) + \frac{l}{2}\left(\cos\psi^{(1)}(t) + \cos\psi^{(2)}(t)\right), \tag{13a}$$

$$x_{2c}^{(2)}(t) = x_{2c}^{(1)}(t) + \frac{l}{2}\left(\sin\psi^{(1)}(t) + \sin\psi^{(2)}(t)\right), \tag{13b}$$

and for $\beta = 3,4,\cdots,n$

$$x_{1c}^{(\beta)}(t) = x_{1c}^{(1)}(t) + \frac{l}{2}\cos\psi^{(1)}(t) + \sum_{\alpha=2}^{\beta-1} l\cos\psi^{(\alpha)}(t) + \frac{l}{2}\cos\psi^{(\beta)}(t), \tag{13c}$$

$$x_{2c}^{(\beta)}(t) = x_{2c}^{(1)}(t) + \frac{l}{2}\sin\psi^{(1)}(t) + \sum_{\alpha=2}^{\beta-1} l\sin\psi^{(\alpha)}(t) + \frac{l}{2}\sin\psi^{(\beta)}(t). \tag{13d}$$

Equations (13a-d) reveal that the system configuration is completely determined by the three link-1 coordinates $\left\{x_{1c}^{(1)}(t),\ x_{2c}^{(1)}(t),\ \psi^{(1)}(t)\right\}$ and the angular coordinates: $\psi^{(\alpha)}(t)$ for $\alpha = 2,\cdots,n$. These coordinates are referred to as the *essential system coordinates* $\{q(t)\}$:

$$\{q(t)\} = \left(x_{1c}^{(1)}(t)\ \ x_{2c}^{(1)}(t)\ \ \psi^{(1)}(t)\ \ \psi^{(2)}(t)\ \ \cdots\ \ \psi^{(n)}(t)\right)^{T}. \tag{14}$$

where $()^{T}$ denotes the transposition of the matrix (). An alternative selection is also acceptable, in which the angular coordinates are replaced by the relative angular coordinates: $\theta^{(1)}(t) = \psi^{(1)}(t)$ and $\theta^{(\alpha)}(t)$ for $\alpha = 2,\cdots,n$. Therefore, the n-link system has $n+2$ degrees-of-freedom. Since we use *Hamilton's principle* to derive equations of motion analytically, the internal energy of torsional springs is considered next.

4.2.2 Potential Energy of Torsional Springs at Actuation Joints

At time $t = 0$, a flexible rigid-link system takes a straight reference configuration without any joint actuations and any external loads. The multi-rigid-link model must behave like a passive flexible beam or rod without internal actuation when it is subjected to external loads. To endow the rigid-link system with flexibility, torsional springs of spring constant *k* are considered at all joints. At each joint, two types of relative angular velocities take place.

At the α^{th} joint between link-α and link-$(\alpha + 1)$, the relative angular displacement $\theta^{(\alpha+1)}(t)$ was defined in Eq. (5b). Observing that two types of relative angular deformation take place, we decompose the angular velocity into the elastic angular velocity $\dot{\theta}^{el(\alpha+1)}(t)$ and actuation angular velocity: $\dot{\theta}^{\#(\alpha+1)}(t)$.

$$\dot{\theta}^{(\alpha+1)}(t) = \dot{\theta}^{el(\alpha+1)}(t) + \dot{\theta}^{\#(\alpha+1)}(t), \tag{15a}$$

Since a joint motor has a unique one-to-one relationship between the motor torque T_{mo} and the actuation angular velocity $\dot{\theta}^{\#(\alpha+1)}(t)$, it is assumed that the actuation angular velocity can be specified.

Knowing that the total angular velocity $\dot{\theta}^{(\alpha+1)}(t)$ is measured and $\dot{\theta}^{\#(\alpha+1)}(t)$ is prescribed, Eq. (15a) is used to define $\dot{\theta}^{el(\alpha+1)}(t)$ from those two known rates:

$$\dot{\theta}^{el(\alpha+1)}(t) = \dot{\theta}^{(\alpha+1)}(t) - \dot{\theta}^{\#(\alpha+1)}(t), \tag{15b}$$

The time integration of Eq. (15b) defines the elastic angular displacement as the difference between the angular displacement $\theta^{(\alpha+1)}(t)$ and the prescribed actuation angular-displacement $\theta^{\#(\alpha+1)}(t)$:

$$\theta^{el(\alpha+1)}(t) = \theta^{(\alpha+1)}(t) - \theta^{\#(\alpha+1)}(t). \tag{15c}$$

It is assumed that the torsional spring is installed with an attachment mechanism so that spring torque is only induced by the elastic part of angular displacement $\theta^{el(\alpha+1)}(t)$. With this assumption, the strain energy or internal energy $U(t)$ of the multi-link system is expressed as

$$U(t) = \frac{1}{2}\sum_{\alpha=1}^{n-1} k\left\{\theta^{(\alpha+1)}(t) - \theta^{\#(\alpha+1)}(t)\right\}^2. \tag{16a}$$

Noting that the actuation angular displacement is prescribed at each time step, $\delta\theta^{\#(\alpha+1)} = 0$, the variation of the internal energy is expressed as:

$$\delta U(t) = \sum_{\alpha=1}^{n-1} \delta\theta^{(\alpha+1)}(t)\; k\left\{\theta^{(\alpha+1)}(t) - \theta^{\#(\alpha+1)}(t)\right\}$$

$$= \sum_{\alpha=1}^{n-1}\left\{\delta\psi^{(\alpha+1)}(t) - \delta\psi^{(\alpha)}(t)\right\}k\left\{\psi^{(\alpha+1)}(t) - \psi^{(\alpha)}(t) - \theta^{\#(\alpha+1)}(t)\right\}. \tag{16b}$$

In matrix form, Eq. (16b) is written as follows:

$$\delta U(t) = \sum_{\alpha=1}^{n-1} \begin{pmatrix} \delta\psi^{(\alpha)}(t) \\ \delta\psi^{(\alpha+1)}(t) \end{pmatrix}^T \left\{ \begin{bmatrix} k & -k \\ -k & k \end{bmatrix} \begin{pmatrix} \psi^{(\alpha)}(t) \\ \psi^{(\alpha+1)}(t) \end{pmatrix} - \begin{pmatrix} -k \\ k \end{pmatrix} \theta^{\#(\alpha+1)}(t) \right\}. \tag{16c}$$

We express the variation of internal energy using the essential generalized displacements $\{q(t)\}$ in Eq. (14) and its variation $\{\delta q(t)\}$ to define the system stiffness matrix $[K^*]$ and the virtual force $\{F^{\#}(t)\}$ due to the actuation as:

$$\delta U(t) = \{\delta q(t)\}^T\left\{[K^*]\{q(t)\} - \{F^{\#}(t)\}\right\}, \tag{17a}$$

where

$$[K^*] = \begin{bmatrix} 0 & 0 & 0 & 0 & 0 & \cdots & \cdots & 0 & 0 \\ 0 & 0 & 0 & 0 & 0 & \cdots & \cdots & 0 & 0 \\ 0 & 0 & k & -k & 0 & \cdots & \cdots & 0 & 0 \\ 0 & 0 & -k & 2k & -k & 0 & \cdots & 0 & 0 \\ 0 & 0 & 0 & -k & 2k & k & \cdots & 0 & 0 \\ 0 & 0 & 0 & 0 & -k & 2k & -k & 0 & 0 \\ \vdots & \vdots & \vdots & \vdots & \vdots & \vdots & \vdots & \vdots & \vdots \\ 0 & 0 & 0 & 0 & 0 & 0 & -k & 2k & -k \\ 0 & 0 & 0 & 0 & 0 & 0 & 0 & -k & k \end{bmatrix}, \tag{17b}$$

$$\{F^{\#}(t)\} = \begin{pmatrix} 0 \\ 0 \\ -k\theta^{\#(2)}(t) \\ k\left(\theta^{\#(2)}(t) - \theta^{\#(3)}(t)\right) \\ k\left(\theta^{\#(3)}(t) - \theta^{\#(4)}(t)\right) \\ \vdots \\ k\left(\theta^{\#(n-1)}(t) - \theta^{\#(n)}(t)\right) \\ k\,\theta^{\#(n)}(t) \end{pmatrix}. \tag{17c}$$

It is noted here that $\{F^{\#}(t)\}$ is not the motor torque, but the residual torques due to the off-set angle $\theta^{\#(\alpha)}$.

When we compare the deflection of the discrete rigid link model with that of a continuous beam, the spring constant *k* will be determined to have the same bending strain energy as the continuous beam counterpart.

4.2.3 Velocities and Kinetic Energy of the System

We next define the kinetic energy of the linked system to prepare for the use of Hamilton's principle to derive equations of motion. The kinetic energy $K^{(\alpha)}(t)$ of link-α consists of: (i) the translational kinetic energy computed by using the velocity at the center of mass, $\dot{\mathbf{r}}^{(\alpha)}(t) \equiv d\mathbf{r}_C^{(\alpha)}(t)/dt$ and (ii) the rotational energy computed by using the angular velocity of the link $\dot{\psi}^{(\alpha)}(t)$:

$$K^{(\alpha)}(t) = \frac{1}{2}\begin{pmatrix} \dot{x}_c^{(\alpha)}(t) \\ \dot{\psi}^{(\alpha)}(t) \end{pmatrix}^T \begin{bmatrix} mI_2 & 0 \\ 0 & J_c \end{bmatrix} \begin{pmatrix} \dot{x}_c^{(\alpha)}(t) \\ \dot{\psi}^{(\alpha)}(t) \end{pmatrix}$$

$$= \frac{1}{2}\begin{pmatrix} \dot{x}_{1c}^{(\alpha)}(t) \\ \dot{x}_{2c}^{(\alpha)}(t) \\ \dot{\psi}^{(\alpha)}(t) \end{pmatrix}^T \begin{bmatrix} m & 0 & 0 \\ 0 & m & 0 \\ 0 & 0 & J_c \end{bmatrix} \begin{pmatrix} \dot{x}_{1c}^{(\alpha)}(t) \\ \dot{x}_{2c}^{(\alpha)}(t) \\ \dot{\psi}^{(\alpha)}(t) \end{pmatrix}. \quad (18)$$

where I_2 denotes a 2×2 identity matrix.

The system kinetic energy $K(t)$ is obtained by accumulating the kinetic energy of the link system. We express it in matrix form in terms of the *system generalized velocities* $\{\dot{X}(t)\}$ and the system mass matrix $[M]$ as:

$$K(t) = \frac{1}{2}\{\dot{X}(t)\}^T [M]\{\dot{X}(t)\}, \quad (19a)$$

where the generalized velocities are stored in 3n×1 column matrix as:

$$\{\dot{X}(t)\} = \left\{\left(\dot{x}_c^{(1)}(t)\right)^T \ \dot{\psi}^{(1)}(t) \ \left(\dot{x}_c^{(2)}(t)\right)^T \ \dot{\psi}^{(2)}(t) \cdots \left(\dot{x}_c^{(n)}(t)\right)^T \ \dot{\psi}^{(n)}(t)\right\}^T, \quad (19b)$$

and the system mass matrix becomes a 3n×3n diagonal matrix:

$$[M] = \text{diag}(m \ \ m \ \ J_c \ \ m \ \ m \ \ J_c \ \ \cdots \ \ m \ \ m \ \ J_c). \quad (19c)$$

4.2.4 Computation of System Velocities

It is necessary to express the system generalized velocities $\{\dot{X}(t)\}$ *in* terms of the *essential system generalized velocities* $\{\dot{q}(t)\}$. We express the linear relation in matrix form as

$$\{\dot{X}(t)\} = [B(t)]\{\dot{q}(t)\}, \quad (20a)$$

where the essential generalized velocities are defined from Eq. (14) as:

$$\{\dot{q}(t)\} = \left(\dot{x}_{1c}^{(1)}(t) \ \ \dot{x}_{2c}^{(1)}(t) \ \ \dot{\psi}^{(1)}(t) \ \ \dot{\psi}^{(2)}(t) \ \ \cdots \ \ \dot{\psi}^{(n)}(t)\right)^T. \quad (20b)$$

To obtain $[B(t)]$, we compute the time derivatives of Eqs. (13a-d). The results for $\beta = 1$ are identity relations:

$$\dot{x}_{1c}^{(1)}(t) = \dot{x}_{1c}^{(1)}(t), \tag{21a}$$

$$\dot{x}_{2c}^{(1)}(t) = \dot{x}_{2c}^{(1)}(t), \tag{21b}$$

$$\dot{\psi}^{(1)}(t) = \dot{\psi}^{(1)}(t). \tag{21c}$$

The results for $\beta = 2$ are

$$\dot{x}_{1c}^{(2)}(t) = \dot{x}_{1c}^{(1)}(t) - \frac{l}{2}\dot{\psi}^{(1)}(t)\sin\psi^{(1)}(t) - \frac{l}{2}\dot{\psi}^{(2)}(t)\sin\psi^{(2)}(t), \tag{21d}$$

$$\dot{x}_{2c}^{(2)}(t) = \dot{x}_{2c}^{(1)}(t) - \frac{l}{2}\dot{\psi}^{(1)}(t)\cos\psi^{(1)}(t) - \frac{l}{2}\dot{\psi}^{(2)}(t)\cos\psi^{(2)}(t), \tag{21e}$$

$$\dot{\psi}^{(2)}(t) = \dot{\psi}^{(2)}(t), \tag{21f}$$

and for $\beta = 3,4,\cdots,n$,

$$\dot{x}_{1c}^{(\beta)}(t) = \dot{x}_{1c}^{(1)}(t) - \frac{l}{2}\dot{\psi}^{(1)}(t)\sin\psi^{(1)}(t) - \tag{21g}$$

$$\sum_{\alpha=2}^{\beta-1} l\,\dot{\psi}^{(\alpha)}(t)\sin\psi^{(\alpha)}(t) - \frac{l}{2}\dot{\psi}^{(\beta)}(t)\sin\psi^{(\beta)}(t)$$

$$\dot{x}_{2c}^{(\beta)}(t) = \dot{x}_{2c}^{(1)}(t) - \frac{l}{2}\dot{\psi}^{(1)}(t)\cos\psi^{(1)}(t) - \tag{21h}$$

$$\sum_{\alpha=2}^{\beta-1} l\,\dot{\psi}^{(\alpha)}(t)\cos\psi^{(\alpha)}(t) - \frac{l}{2}\dot{\psi}^{(\beta)}(t)\cos\psi^{(\beta)}(t)$$

$$\dot{\psi}^{(\beta)}(t) = \dot{\psi}^{(\beta)}(t). \tag{21i}$$

Equations (21a-i) can be expressed in matrix form in Eq. (20a) to analytically define the matrix $[B(t)]$. It is observed that the columns corresponding proximal velocities can take nonzero values.

4.2.5 Hamilton's Principle and Equations of Motion

For multi-body systems, Hamilton's principle is written for an arbitrary duration $t_0 \le t \le t_1$ as

$$\int_{t_0}^{t_1}\{\delta K(t) - \delta U(t) + \delta W(t)\}dt = 0, \tag{22a}$$

assuming that virtual displacements vanish at $t = t_0$ and t_1:

$$\{q(t_0)\} = \{q(t_1)\} = \{0\}. \tag{22b}$$

In Eq. (22a) δW denotes the virtual work done by external forces, illustrated in Fig. 1:

$$\delta W(t) = \sum_{\alpha=1}^{n} \begin{pmatrix} \delta x_{1c}^{(\alpha)}(t) \\ \delta x_{2c}^{(\alpha)}(t) \\ \delta \psi^{(\alpha)}(t) \end{pmatrix}^T \begin{pmatrix} \hat{n}_1^{(\alpha)}(t) \\ \hat{n}_2^{(\alpha)}(t) \\ \hat{m}_3^{(\alpha)}(t) \end{pmatrix} = \{\delta X(t)\}^T \{\hat{F}_{ex}(t)\}. \tag{23}$$

We observe that for planar dynamics the $\delta -$ and $t -$ derivatives commute:

$$\delta\{\dot{X}(t)\} = \frac{d}{dt}\{\delta X(t)\}, \tag{24a}$$

and the same $[B(t)]$ matrix in Eq. (20a) expresses the linear relation between $\{\delta X(t)\}$ and $\{\delta q(t)\}$:

$$\{\delta X(t)\} = [B(t)]\{\delta q(t)\}. \tag{24b}$$

As preparation, we take the variation of Eq. (19a) and use Eq. (24a):

$$\delta K(t) = \left(\delta\{\dot{X}(t)\}\right)^T [M]\{\dot{X}(t)\} = \left(\frac{d}{dt}\{\delta X(t)\}\right)^T [M]\{\dot{X}(t)\}$$

$$= \frac{d}{dt}\left(\{\delta X(t)\}^T [M]\{\dot{X}(t)\}\right) - \{\delta X(t)\}^T \frac{d}{dt}\left([M]\{\dot{X}(t)\}\right). \tag{25a}$$

We rewrite the above using Eq. (24b):

$$\delta K(t) = \frac{d}{dt}\left(\{\delta q(t)\}^T [B(t)]^T [M][B(t)]\{\dot{q}(t)\}\right)$$

$$-\{\delta q(t)\}^T [B(t)]^T \frac{d}{dt}\left([M][B(t)]\{\dot{q}(t)\}\right). \tag{25b}$$

Equation (23) is also rewritten using Eq. (24b) as:

$$\delta W(t) = \{\delta q(t)\}^T [B(t)]^T \{\hat{F}_{ex}(t)\}. \quad (26)$$

To obtain the equations of motion, we substitute Eqs. (25b), (17a), and (26) into Eq. (22a) using Eq. (22b):

$$-\int_{t_0}^{t_1} \{\delta q(t)\}^T \left[[B(t)]^T \frac{d}{dt}([M][B(t)]\{\dot{q}(t)\}) + [K^*]\{q(t)\} - \{F^{\#}(t)\} - [B(t)]\{\hat{F}_{ex}(t)\} \right] dt = 0. \quad (27)$$

The resulting equations of motion are

$$[M^*(t)]\{\ddot{q}(t)\} + [N^*(t)]\{\dot{q}(t)\} + [K^*]\{q(t)\} = \{F^{\#}(t)\} + \{\hat{F}_{ex}^*(t)\}, \quad (28a)$$

where $[M^*(t)]$ is symmetric and referred to as the reduced mass matrix:

$$[M^*(t)] = [B(t)]^T [M][B(t)], \quad (28b)$$

$$[N^*(t)] = [B(t)]^T [M]\left[\dot{B}(t)\right], \quad (28c)$$

$$\{\hat{F}_{ex}^*(t)\} = [B(t)]\{\hat{F}_{ex}(t)\}. \quad (28d)$$

In Eq. (28a), the term $[N^*(t)]\{\dot{q}(t)\}$ represents the nonlinear velocity terms including the centripetal and Coriolis accelerations, and $\{\hat{F}_{ex}^*(t)\}$ expresses the reduced external forces.

Equation (28a) indicates that the system deforms without external forces by motor actuation, which induces the actuation forces $\{F^{\#}(t)\}$. Furthermore, Eq. (28a) reduces to the equations of a multi-body system without flexibility [5] by eliminating the stiffness matrix $[K^*]$ and the actuation forces $\{F^{\#}(t)\}$. Without flexibility, a multi-body system moves by motors or other actuators. They are included in the reduced external force vector $\{\hat{F}_{ex}^*(t)\}$. Next, we derive a continuous beam model with internal actuation.

4.3 A Large-Deformation Planar Beam Model

An active spatial beam model was developed employing the assumption of rigid cross-sections during deformation and Élie Cartan's moving frame method [9]. In this

section, the planar equations of motion and the beam principle of virtual work, which are reduced from the spatial equations, will be summarized first. The internal actuation will be discussed in the next section.

Let the ambient Euclidean 3-space be described by a fixed Cartesian coordinate system $\{z^1 \quad z^2 \quad z^3\}$. We consider planar motions of an active beam in the z^1, z^2 -plane so that all rotations are expressed with respect to the z^3-axis with unit coordinate vector $\mathbf{e}_3^I = \frac{\vec{\partial}}{\partial z^3}$.

The inertial-coordinate basis vectors are expressed as:

$$\tilde{\mathbf{e}}^I = (\mathbf{e}_1^I \quad \mathbf{e}_2^I) = \left(\frac{\vec{\partial}}{\partial z^1} \quad \frac{\vec{\partial}}{\partial z^2}\right), \tag{29}$$

where the coordinate tangent vectors are expressed as differential operators utilizing the notation of modern differential geometry [7,10].

As shown in Fig. 2, at time $t = 0$ in the reference configuration $B(0)$, the beam of length L with uniform cross section is straight. To identify a point on the body, a Cartesian coordinate system $\{S = X^1, X^2\}$ is defined with the $S = X^1$-axis along the *line of centroids* and the X^2-axis on the plane of the cross section with the centroid at $X^2 = 0$. These axes are parallel to the fixed z^1, z^2-coordinate axes. The reference line of centroids is expressed as $\mathbf{r}_c(S, 0) = \mathbf{e}_1^I S$. On the line of centroids at $t = 0$, using X^1, X^2-coordinates, we form the coordinate vector basis to define an orthonormal frame attached at each point on the line:

$$\tilde{\mathbf{e}}(S, 0) \equiv \big(\mathbf{e}_1(S, 0) \quad \mathbf{e}_2(S, 0)\big) = \left(\frac{\vec{\partial}}{\partial X^1} \quad \frac{\vec{\partial}}{\partial X^2}\right). \tag{30}$$

This frame $\tilde{\mathbf{e}}(S, 0)$ is parallel to the inertial frame $\tilde{\mathbf{e}}^I$.

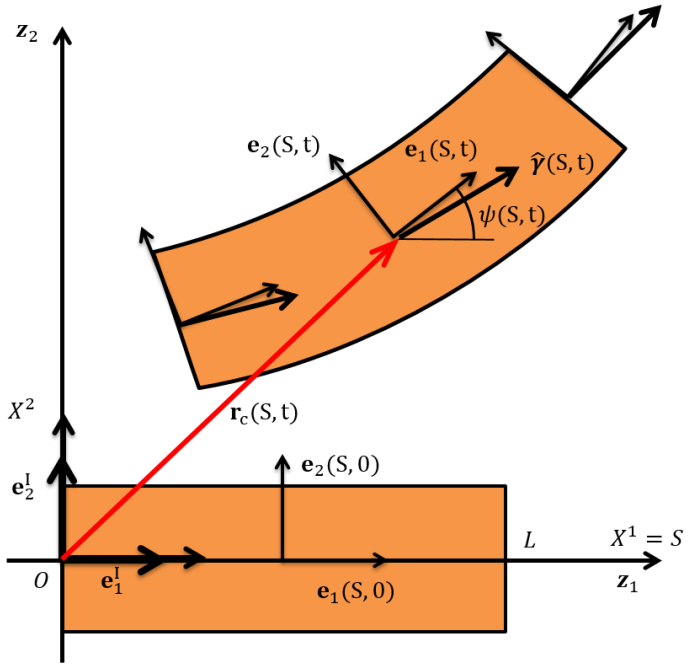

Figure 4-2: Reference and current beam configuration demonstrating the coordinate frames

The material coordinates $S = X^1, X^2$ are virtually inscribed to the body at $t = 0$ to form the *convected curvilinear coordinates* $S = X^1$ and X^2 during deformation. At time *t* due to deformation, the line of centroids becomes the *curve of centroids*, expressed by $\mathbf{r}_c(S,t)$, where the reference arc length S is used to parameterize the curve. Therefore, S is no longer the arc length in the deformed curve of centroids.

By using the inertial frame and employing the abbreviated notation in Eq. (29), the position vector of the curve of centroids is expresses as:

$$\mathbf{r}_c(S,t) = \mathbf{e}^I \begin{pmatrix} z_c^1(S,t) \\ z_c^2(S,t) \end{pmatrix}. \tag{31}$$

Due to the assumption of rigid cross-sections during the deformation of a beam, the tangent vector $\vec{\partial}/\partial X^2$ to the convected X^2-axis remains the unit vector. Utilizing this unit

coordinate vector as $\mathbf{e}_2(S,t)$ and defining the unit normal vector $\mathbf{e}_1(S,t)$ to the cross section, we define a moving frame on the curve of centroids $\mathbf{r_c}(S,t)$, as shown in Fig. 2:

$$\tilde{\mathbf{e}}(S,t) \equiv \big(\mathbf{e}_1(S,t) \quad \mathbf{e}_2(S,t)\big), \tag{32a}$$

where

$$\mathbf{e}_2(S,t) = \frac{\vec{\partial}}{\partial X^2}. \tag{32b}$$

The attitude of the moving frame is expressed by the rotation matrix using the angle of rotation $\psi(S,t)$ with the z^3-axis, which is normal to the plane:

$$\big(\mathbf{e}_1(S,t) \quad \mathbf{e}_2(S,t)\big) = (\mathbf{e}_1^I \quad \mathbf{e}_2^I)\begin{bmatrix}\cos\psi(S,t) & -\sin\psi(S,t)\\ \sin\psi(S,t) & \cos\psi(S,t)\end{bmatrix}. \tag{33a}$$

For brevity, Eq. (33a) is written as:

$$\tilde{\mathbf{e}}(S,t) = \mathbf{e}^I R_3\big(\psi(S,t)\big). \tag{33b}$$

The inverse attitude relation is expressed as:

$$\mathbf{e}^I = \tilde{\mathbf{e}}(S,t)R_3^T\big(\psi(S,t)\big) = \tilde{\mathbf{e}}(S,t)R_3\big(-\psi(S,t)\big). \tag{33c}$$

The time-rate of the frame rotation is obtained by taking the time derivative of Eq. (33b) at a fixed S and using Eq. (33c).

$$\frac{\partial}{\partial t}\tilde{\mathbf{e}}(S,t) = \mathbf{e}^I \frac{\partial R_3(\psi)}{\partial \psi}\frac{\partial \psi}{\partial t} = \tilde{\mathbf{e}}(S,t)\left(R_3^T(\psi)\frac{\partial R_3(\psi)}{\partial \psi}\right)\frac{\partial \psi}{\partial t}. \tag{34a}$$

The above is further simplified by performing the $R_3^T(\psi)(\partial R_3(\psi)/\partial\psi)$ operation as:

$$\frac{\partial}{\partial t}\tilde{\mathbf{e}}(S,t) = \tilde{\mathbf{e}}(S,t)\begin{bmatrix}0 & -1\\ 1 & 0\end{bmatrix}\frac{\partial\psi(S,t)}{\partial t}. \tag{34b}$$

At a fixed time *t* moving along the curve of centroids, *i.e.*, taking the S-derivative of Eq. (32a) and using Eq. (33c), the frame connection is expressed by the curvature parameter, $\partial\psi(S,t)/\partial s$ as:

$$\frac{\partial}{\partial S}\tilde{\mathbf{e}}(S,t) = \mathbf{e}^I \frac{\partial R_3(\psi)}{\partial \psi}\frac{\partial \psi}{\partial S} = \tilde{\mathbf{e}}(S,t)\left(R_3^T(\psi)\frac{\partial R_3(\psi)}{\partial \psi}\right)\frac{\partial \psi}{\partial S}, \tag{35a}$$

$$\frac{\partial}{\partial S}\tilde{\mathbf{e}}(S,t) = \tilde{\mathbf{e}}(S,t)\begin{bmatrix}0 & -1\\ 1 & 0\end{bmatrix}\frac{\partial \psi(S,t)}{\partial S}. \tag{35b}$$

The tangent vector $\hat{\boldsymbol{\gamma}}(S,t)$ to the centroidal curve, Eq. (31), is expressed by both the inertial and the moving frames as:

$$\hat{\boldsymbol{\gamma}}(S,t) = \frac{\partial}{\partial S}\mathbf{r}_c(S,t) = \mathbf{e}^I\begin{pmatrix}\frac{\partial z_c^1(S,t)}{\partial S}\\ \frac{\partial z_c^2(S,t)}{\partial S}\end{pmatrix} = \tilde{\mathbf{e}}(S,t)\begin{pmatrix}\hat{\gamma}_1(S,t)\\ \hat{\gamma}_2(S,t)\end{pmatrix}. \tag{36}$$

In the following, without showing the reduction processes, we present the resulting equations of motion from the spatial beam equations [9]. In addition, we present the reduced d'Alembert principle of virtual work for finite element implementation of the active beam model. It is intended to present a more geometrical interpretation of the equations. At the same time, for passive beams, the results are compared with those published previously.

4.3.1 Beam Equations of Motion

Beam stress $\boldsymbol{N}(S,t)$ represents the resultant stress forces acting on the cross section at *S* on the curve of centroids. Using the notation in Eq. (31), $\boldsymbol{N}(S,t)$ consists of the normal force (tensile or compressive) $N_1(S,t)$ and the *transverse shear force* $N_2(S,t)$:

$$\boldsymbol{N}(S,t) = \tilde{\mathbf{e}}(S,t)\begin{pmatrix}N_1(S,t)\\ N_2(S,t)\end{pmatrix}. \tag{37}$$

The bending moment acting on the cross section at *S* is denoted by $M_3(S,t)$.

To represent the effect of gravitational body forces and distributed surface tractions, external distributed force $\hat{\boldsymbol{n}}(S,t)$ and distributed couple $\hat{m}_3(S,t)$ are also defined per unit

reference line of centroids. They act on the infinitesimal beam element. The components of the distributed force $\hat{\boldsymbol{n}}(S,t)$ are expressed with the moving frame as:

$$\hat{\boldsymbol{n}}(S,t) = \tilde{\mathbf{e}}(S,t)\begin{pmatrix}\hat{n}_1(S,t)\\ n_2(S,t)\end{pmatrix}. \tag{38}$$

To acquire a geometrical picture, the free-body diagram of an infinitesimal beam element is shown, between the arc parameter S and $S+\Delta S$ in Fig. 3. The element is subjected to the stress vector $\boldsymbol{N}(S,t)$, moment $M_3(S,t)$, the distributed force $\hat{\boldsymbol{n}}(S,t)$, and distributed couple $\hat{m}_3(S,t)$. In Fig. 3, the tangent vector $\hat{\boldsymbol{\gamma}}(S,t)$ to the curve of centroids is also shown.

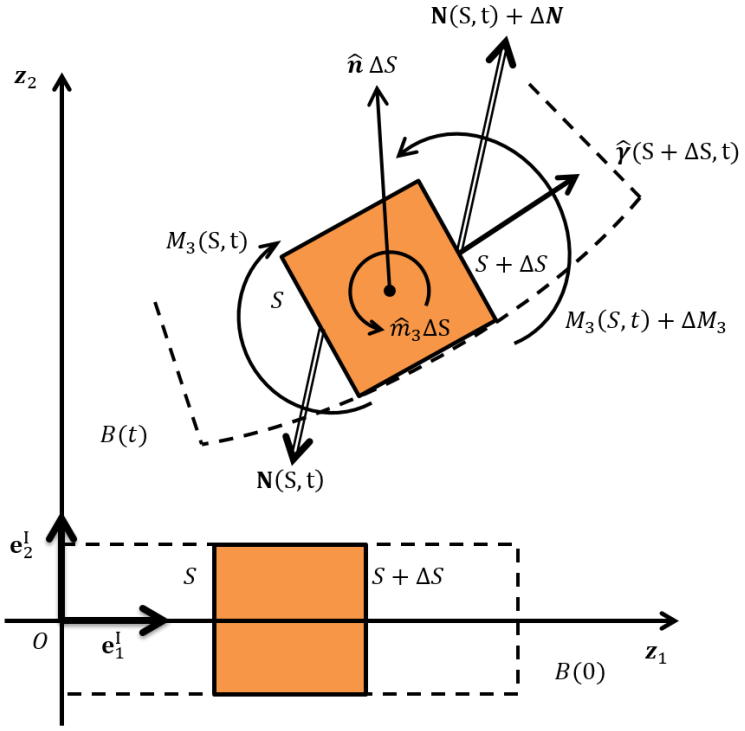

Figure 4-3: A free-body diagram of an infinitesimal beam element to derive the equations of motion

Let the mass per unit length of the reference line of centroids be expressed by m_0, and the moment of inertia of the cross section be denoted by J_3. The free-body-diagram

enables the derivation of the equations of motion for the dynamic loading case. The figure was also utilized by Reissner to derive the beam equilibrium equations [11].

For translational motion, Newton's second law applies:

$$\lim_{\Delta S\to 0}\frac{1}{\Delta S}\left(\Delta \boldsymbol{N}(S,t)+\hat{\boldsymbol{n}}(S,t)\Delta S-m_0\Delta S\frac{\partial^2}{\partial t^2}\mathbf{r}_C(S,t)\right)=0\ . \tag{39a}$$

For the rotational motion of the cross section, time rate of angular momentum becomes the external torque applied to the element. Considering the moment with the z^3-axis, one finds

$$\lim_{\Delta S\to 0}\frac{1}{\Delta S}\left(\Delta M_3(S,t)+\left(\hat{\boldsymbol{\gamma}}(S,t)\Delta S\times\boldsymbol{N}(S,t)\right)_3+\ \hat{m}_3(S,t)\Delta S-J_3\Delta S\frac{\partial^2}{\partial t^2}\psi(S,t)\right)=0. \tag{39b}$$

We evaluate the cross product in Eq. (39b) with respect to $\tilde{\mathbf{e}}(S,t)$ using Eqs. (36) and (37) and find

$$\left(\hat{\boldsymbol{\gamma}}(S,t)\Delta S\times\boldsymbol{N}(S,t)\right)_3=\Delta S\{-\hat{\gamma}_2(S,t)N_1(S,t)+\hat{\gamma}_1(S,t)N_2(S,t)\}. \tag{39c}$$

From Eq. (39a), the beam equation in vector form for translational motion is

$$\frac{\partial}{\partial S}\boldsymbol{N}(S,t)+\hat{\boldsymbol{n}}(S,t)=m_0\frac{\partial^2}{\partial t^2}\mathbf{r}_C(S,t). \tag{40}$$

From Eqs. (39b, c), the beam rotational equation of motion becomes

$$\frac{\partial}{\partial S}M_3(S,t)-\hat{\gamma}_2(S,t)N_1(S,t)+\hat{\gamma}_1(S,t)N_2(S,t)$$

$$+\hat{m}_3(S,t)=J_3\frac{\partial^2}{\partial t^2}\psi(S,t). \tag{41}$$

A geometrically-exact finite element (FE) implementation of the above equations was presented by Simo and Vu-Quoc [12, 13].

The component expression is obtained by substituting Eqs. (37) and (38) into the left-hand side of Eq. (40) and using Eq. (35):

$$\text{LHS} = \frac{\partial}{\partial S}(\tilde{\mathbf{e}}\, N) + \tilde{\mathbf{e}}\, \hat{n} = \frac{\partial \tilde{\mathbf{e}}}{\partial S} N + \tilde{\mathbf{e}} \frac{\partial N}{\partial S} + \tilde{\mathbf{e}}\, \hat{n}$$

$$= \tilde{\mathbf{e}} \left(\frac{\partial \psi}{\partial s} \begin{bmatrix} 0 & -1 \\ 1 & 0 \end{bmatrix} \begin{pmatrix} N_1 \\ N_2 \end{pmatrix} + \frac{\partial}{\partial S} \begin{pmatrix} N_1 \\ N_2 \end{pmatrix} + \begin{pmatrix} \hat{n}_1 \\ \hat{n}_2 \end{pmatrix} \right), \tag{42a}$$

The right-hand side of Eq. (40) is rewritten with respect to the moving frame using Eq. (33c) as:

$$\text{RHS} = \mathbf{e}^I\, m_0 \frac{\partial^2 z_c}{\partial t^2}. \tag{42b}$$

The resulting translational equations of motion expressed are expressed with respect to the inertial frame as follows:

$$\begin{bmatrix} \cos\psi(S,t) & -\sin\psi(S,t) \\ \sin\psi(S,t) & \cos\psi(S,t) \end{bmatrix} \begin{pmatrix} \frac{\partial}{\partial S} N_1(S,t) - \frac{\partial \psi(S,t)}{\partial S} N_2(S,t) + \hat{n}_1(S,t) \\ \frac{\partial}{\partial S} N_2(S,t) - \frac{\partial \psi(S,t)}{\partial S} N_2(S,t) + \hat{n}_2(S,t) \end{pmatrix}$$

$$= \begin{pmatrix} m_0 \frac{\partial^2 z_{1c}(S,t)}{\partial t^2} \\ m_0 \frac{\partial^2 z_{2c}(S,t)}{\partial t^2} \end{pmatrix}. \tag{43}$$

For static problems, Eqs. (40), (41) and (43) reduce to the equilibrium equations presented by Reissner [11].

4.3.2 Beam Principle of Virtual Work

The principle of virtual work was derived for a spatial beam from Hamilton's principle [9]. Here, the spatial result is specialized for a planar beam. The virtual displacements of the curve of centroids $\delta \mathbf{r}_c(S,t)$ is expressed as follows:

$$\delta \mathbf{r}_c(S,t) = \mathbf{e}^I \begin{pmatrix} \delta z_c^1(S,t) \\ \delta z_c^1(S,t) \end{pmatrix}, \tag{44}$$

and the virtual angular displacement $\delta\psi(S,t)$ is considered. The virtual displacements vanish at the boundary of the beam at $S = 0$ and/or L, when $\mathbf{r}_c$ is specified at time t. The same rule applies to the virtual angular displacement.

The virtual angular displacement represents the virtual rotation of the moving frame. This is observed by taking the variation of Eq. (33b) and using Eq. (33c) to express the variation by its own frame:

$$\delta\tilde{\mathbf{e}}(S,t) = \mathbf{e}^I \delta R_3\big(\psi(S,t)\big) = \mathbf{e}^I \frac{\partial R_3}{\partial \psi}\delta\psi(S,t)$$

$$= \tilde{\mathbf{e}}(S,t)\left(R_3^T(\psi)\frac{\partial R_3}{\partial \psi}\right)\delta\psi(S,t). \tag{45a}$$

The result indicates that the variation of the frame is expressed by the virtual angular displacement $\delta\psi(S,t)$:

$$\delta\tilde{\mathbf{e}}(S,t) = \tilde{\mathbf{e}}(S,t)\begin{bmatrix}0 & -1\\ 1 & 0\end{bmatrix}\delta\psi(S,t). \tag{45b}$$

The principle of virtual work for planar beams is written as:

$$\int_0^L \left\{\begin{pmatrix}\delta\hat{\gamma}_1(S,t) & \delta\hat{\gamma}_2(S,t)\end{pmatrix}\begin{pmatrix}N_1(S,t)\\ N_2(S,t)\end{pmatrix} + \delta\left(\frac{\partial\psi(S,t)}{\partial S}\right)M_3(S,t)\right\}dS =$$

$$\int_0^L \left\{\delta\mathbf{r}_c(S,t)\left(\hat{\boldsymbol{n}}(S,t) - m_0\frac{\partial^2\mathbf{r}_c(S,t)}{\partial t^2}\right) + \delta\psi(S,t)\left(\hat{m}_3(S,t) - J_3\frac{\partial^2\psi(S,t)}{\partial t^2}\right)\right\}dS$$

$$+\{\delta\mathbf{r}_C(L,t)\cdot\hat{\boldsymbol{n}}_E(L,t) + \delta\psi(L,t)\hat{m}_E(L,t)\}$$

$$-\{\delta\mathbf{r}_C(0,t)\cdot\hat{\boldsymbol{n}}_E(0,t) + \delta\psi(0,t)\hat{m}_E(0,t)\}. \tag{46}$$

The left-hand side represents the virtual strain energies of the beam, induced by the resultant stress vector $\boldsymbol{N}(S,t)$ working on the components of the virtual normal and shear strains and moment $M_3(S,t)$ on the virtual angular displacement.

On the right-hand side of Eq. (46), the two integrals show, respectively, the virtual work done by the distributed force and the inertial force on the virtual displacements $\delta\mathbf{r}_C(S,t)$ and the virtual work of the distributed torque and the inertial torque on the virtual angular displacement $\delta\psi(S,t)$.

On the right-hand side, the last two terns in the pair of braces denote, respectively, the virtual work at $S=L$ and that at $S=0$. At each end, the virtual work consists of the prescribed traction force vector $\hat{\boldsymbol{n}}_E$ on the virtual displacement $\delta\mathbf{r}_C(S,t)$ and the prescribed torque $\hat{m}_E$ on the virtual angular displacement $\delta\psi$.

One of the advantages of the principle of virtual work is that it gives a consistent set of boundary conditions. At each end, the boundary conditions are: (i) for each component either displacement $\mathbf{r}_C(t)$ or the corresponding component of traction $\hat{\boldsymbol{n}}_E$ is specified and (ii) either angular displacement ψ or couple $\hat{m}_E$ is specified.

The Euler-Lagrange equations of Eq. (46) yield the beam equations of motion, Eqs. (40) and (41). Here, we first prepare for the computation: (i) the commutativity relation:

$$\partial(\delta\psi/\partial S)=\delta(\partial\psi/\partial S). \tag{47}$$

and (ii) the rewriting of the following term:

$$\begin{aligned}\begin{pmatrix}\delta\hat{\gamma}_1(S,t) & \delta\hat{\gamma}_2(S,t)\end{pmatrix}\begin{pmatrix}N_1(S,t)\\N_2(S,t)\end{pmatrix}&=\tilde{\mathbf{e}}(S,t)\begin{pmatrix}\delta\hat{\gamma}_1(S,t)\\\delta\hat{\gamma}_2(S,t)\end{pmatrix}\cdot\tilde{\mathbf{e}}(S,t)\begin{pmatrix}N_1(S,t)\\N_2(S,t)\end{pmatrix}\\&=\tilde{\mathbf{e}}(S,t)\,\delta\hat{\gamma}\cdot\boldsymbol{N}(S,t).\end{aligned} \tag{48a}$$

Here, we note that $\tilde{\mathbf{e}}(S,t)\,\delta\hat{\gamma}\neq\delta\hat{\boldsymbol{\gamma}}$.

$$\delta\hat{\boldsymbol{\gamma}}(S,t)=\delta\big(\tilde{\mathbf{e}}(S,t)\,\hat{\gamma}(S,t)\big)=\big(\delta\tilde{\mathbf{e}}(S,t)\big)\hat{\gamma}(S,t)+\tilde{\mathbf{e}}(S,t)\delta\hat{\gamma}(S,t)$$

$$\delta\hat{\boldsymbol{\gamma}}(S,t)=\tilde{\mathbf{e}}(S,t)\begin{bmatrix}0 & -\delta\psi\\\delta\psi & 0\end{bmatrix}\begin{pmatrix}\hat{\gamma}_1\\\hat{\gamma}_2\end{pmatrix}+\tilde{\mathbf{e}}(S,t)\delta\hat{\gamma}(S,t). \tag{48b}$$

We next use the definition of $\hat{\boldsymbol{\gamma}}(S,t)$ from Eq. (36) and use the commutativity of the δ- and S-derivatives of $\mathbf{r}_C(S,t)$

$$\delta\hat{\boldsymbol{\gamma}}(S,t) = \delta\left(\frac{\partial \mathbf{r}_C(S,t)}{\partial S}\right) = \frac{\partial \delta\mathbf{r}_C(S,t)}{\partial S}. \tag{48c}$$

Equations (48b, c) yield

$$\tilde{\mathbf{e}}(S,t)\,\delta\hat{\gamma}(S,t) = \frac{\partial \delta\mathbf{r}_C(S,t)}{\partial S} - \tilde{\mathbf{e}}(S,t)\begin{bmatrix} 0 & -\delta\psi \\ \delta\psi & 0 \end{bmatrix}\begin{pmatrix}\hat{\gamma}_1 \\ \hat{\gamma}_2\end{pmatrix}. \tag{49}$$

Equation (48a) is rewritten using Eq. (49), as:

$$\begin{pmatrix}\delta\hat{\gamma}_1(S,t) & \delta\hat{\gamma}_2(S,t)\end{pmatrix}\begin{pmatrix}N_1(S,t) \\ N_2(S,t)\end{pmatrix}$$

$$= \frac{\partial \delta\mathbf{r}_C(S,t)}{\partial S}\cdot \boldsymbol{N}(S,t) - \tilde{\boldsymbol{e}}(S,t)\begin{bmatrix} 0 & -\delta\psi \\ \delta\psi & 0 \end{bmatrix}\begin{pmatrix}\hat{\gamma}_1 \\ \hat{\gamma}_2\end{pmatrix}\cdot \boldsymbol{N}(S,t)$$

$$= \frac{\partial \delta\mathbf{r}_C(S,t)}{\partial S}\cdot \boldsymbol{N}(S,t) - \delta\psi(S,t)\{-\hat{\gamma}_2(S,t)N_1(S,t) + \hat{\gamma}_1(S,t)N_2(S,t)\}. \tag{50}$$

Using Eqs. (48) and (50), integration by parts is performed on Eq. (46) to obtain the Euler-Lagrange equations, Eqs. (40) and (41).

Beam equations, Eqs. (40), (41), (43), and (46) describe the motion of both passive and active beams. What distinguish active beams from passive beams are the constitutive relations discussed in the following section.

4.4 Active Beam Constitutive Relations

In this section, beam constitutive relations are discussed. To present the effect of internal actuation, simple isotropic relations are assumed for passive beams under small strains (but experiencing large deformation).

4.4.1 Passive Beam Constitutive Relations

The principle of virtual work indicates the conjugate pairs of beam stress and strain variables. In Fig. 2, the vector $\hat{\boldsymbol{\gamma}}$ is tangent to the curve of centroids. Therefore, its

projection to $\mathbf{e}_2$ represents the shear strain $\hat{\gamma}_2$ and its projection to $\mathbf{e}_1$ shows the ratio between the deformed infinitesimal arc length and the reference arc length. Therefore, $\hat{\gamma}_1 - 1$ denotes the axial strain along the curve of centroids. These stains are conjugate to the resultant normal stress force N_1 and resultant shear force N_2 per unit reference line of centroids.

For isotropic beams, the linear relations between the conjugate pairs are expressed as follows:

$$N_1 = EA(\hat{\gamma}_1 - 1), \tag{51a}$$

$$N_2 = GA_s\hat{\gamma}_2, \tag{51b}$$

where *E* and *G* denote Young's modulus and shear modulus, respectively, A is the area of cross section, and $A_s(< A)$ represents the area of the cross section for shear deformation, which is introduced to account for the shear correction factor for shear deformable Timoshenko-type beams.

The curvature $\kappa_3 = \partial\psi/\partial S$ is the conjugate strain to bending moment M_3, and their linear relation is expressed by using the flexural rigidity EI_3 as:

$$M_3 = EI_3\kappa_3. \tag{52}$$

4.4.2 Active Beam Constitutive Relations Under Fixed Internal Actuation

Next, we actuate the beam from the straight reference configuration without external loads. Let the beam strains induced by the internal actuation be expressed by superscript '#'. With this notation, the curvature, shear strain, and axial strain are written as $\kappa_3^{\#}$, $\hat{\gamma}_2^{\#}$, and $\hat{\gamma}_1^{\#} - 1$, respectively.

During the internal actuation, we assume that (i) the curve of centroids remains inextensible, $\hat{\gamma}_1^{\#} = 1$, and (ii) shear strain remains zero, $\hat{\gamma}_2^{\#} = 0$. In other words, the

bending deformation by internal actuation takes place so that the normal cross section to the line of centroids remain normal during the bending-type internal actuation. This type of bending deformation has been assumed in the Euler-Bernoulli beam model. Therefore, the beam under fixed actuation is the same as the elastic deformation of an initially curved beam.

For resultant normal and shear forces, the constitutive relations remain the same as those for a passive beam: Eqs. (51a, b). However, the bending constitutive relation accounts for the preexisting curvature $\kappa_3^{\#}$ in computing the elastic curvature.

$$M_3 = EI_3(\kappa_3 - \kappa_3^{\#}). \tag{53}$$

4.4.3 Active Beam Constitutive Relations During Internal Actuation

During internal actuation, $\dot{\kappa}_3^{\#} \neq 0$, the constitutive relations are all expressed in rate-form using a superposed dot for the (material) time derivative:

$$\dot{N}_1 = \frac{\partial N_1}{\partial t} = EA\dot{\hat{\gamma}}_1, \tag{54a}$$

$$\dot{N}_2 = \frac{\partial N_2}{\partial t} = GA_s\dot{\hat{\gamma}}_2, \tag{54b}$$

$$\dot{M}_3 = \frac{\partial M_3(S,t)}{\partial t} = EI_3(\dot{\kappa}_3 - \dot{\kappa}_3^{\#}). \tag{55}$$

Unloading of external loads brings the beam to a fixed actuation state without any beam stresses and vanishing shear and axial strains.

4.5 Interaction with the Environment

The planar active beam model may be used to simulate the interaction forces with operational environments. Here, we list several example cases to describe the incorporation of the interaction forces with environments.

I. Swimming long animals like snakes, eels and marine worms in the z^1, z^2-plane may be simulated by the equations of motion (40) and (41). Fluid-slender body interaction forces were computed by G. I. Taylor [6] and Lighthill [14]. The fluid interaction forces are incorporated into Eq. (40) as the distributed external force $\hat{\boldsymbol{n}}(S,t)$ along the curve of centroids, while the distributed couple in Eq. (41) may be neglected, $\hat{m}_3(S,t) = 0$.

II. Serpentines, which move on the flat z^1, z^2-plane, can be simulated by Eqs. (40) and (41). Past work by Onal has demonstrated a soft functioning serpentine robot, but it lacked a model showing the interaction with the environment [15]. The interaction forces at the contacting belly on the flat terrain are expressed by $\hat{\boldsymbol{n}}(S,t)$ in Eq. (40), while neglecting the distributed couple, $\hat{m}_3(S,t) = 0$, in Eq. (41). The interaction shear force can also be modeled as a function of the contacting pressure. Saito, et al. [5] described the shear interaction as dry friction or viscous damping.

III. The locomotion of an inchworm on the flat surface, $z^3 = 0$, or general terrain, whose elevation is described by $z^2 = h(z^1)$, may be modeled if the motion is constrained in the z^1, z^2-plane. In this case, the changing contact region during locomotion and the contact normal force as well as the shear force must be incorporated in $\hat{\boldsymbol{n}}(S,t)$ of Eq. (40) along with the gravitational force. The distributed external couple may be neglected, $\hat{m}_3(S,t) = 0$ in Eq. (41). To model the interaction forces with reasonable fidelity, we utilize the description of interaction forces, employed in vehicle dynamics [16, 17]

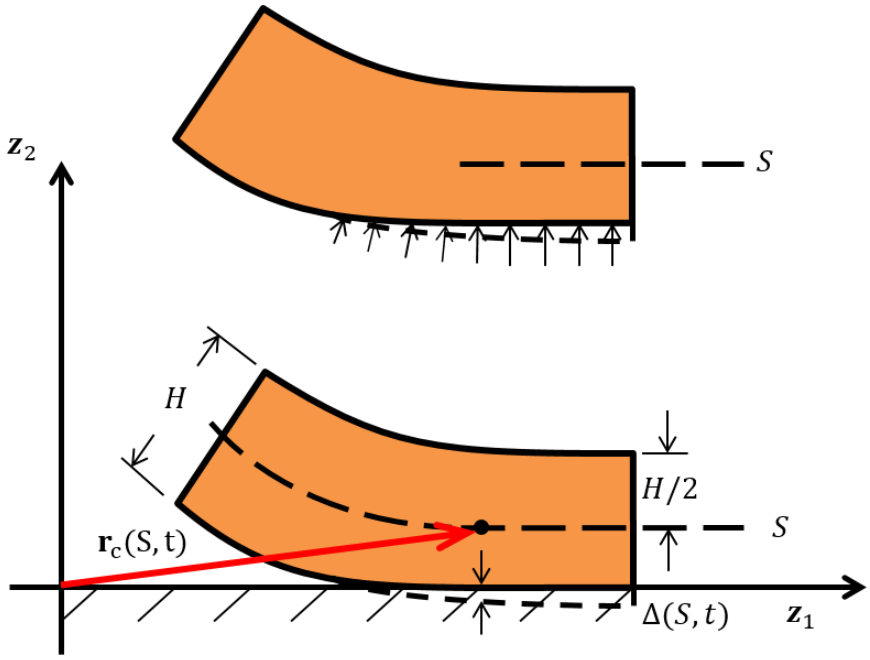

Figure 4-4: Terrain interaction forces including pressure-sinkage and shear-slippage relations

Figure 4 illustrates the tip of a beam, with a thickness of H, in contact with a flat terrain surface. In the contact region, the pressure $p(S,t)$ and shear force $\tau(S,t)$ acting on the beam, which will be expressed in the equation of motion as the external distributed force $\hat{\boldsymbol{n}}(S,t)$ with components: $\hat{n}_2(S,t) = p(S,t)$ and $\hat{n}_1(S,t) = \tau(S,t)$.

We intend to develop a terrain-beam interaction model incorporating Bekker's pressure-sinkage relation [16, 17, 18] and Janosi's shear slippage relation [19]. Bekker's pressure sinkage relation reduces to a Winkler beam model on an elastic foundation on a rigid flat plane [20].

In Bekker's relation, the contact pressure force p and the sinkage Δ are related nonlinearly as:

$$p = \left(\frac{k_c}{b} + k_\phi\right)\Delta^n, \tag{56}$$

where b, k_c, k_ϕ, and n are parameters determined from experiments. The exponent *n* in Eq. (56) essentially describes the mechanical property of the soil under the contact patch. When $n = 1$, Bekker's pressure-sinkage relation incorporates Winkler's beam on an elastic foundation model.

Janosi's relation relates the contact shear force τ and the slippage $[u]$ by using an exponential function as:

$$\tau = \tau_y(p)\{1 - exp(-\beta[u])\}, \tag{57}$$

where β is a positive constant, and $\tau_y(p)$ denotes the critical shear force, which usually increases with confining pressure p.

4.6 Application: Linear Cantilever Beam with Internal Actuation

In this section, we present an example of a beam with internal actuation. We will consider a linear cantilever beam with internal actuation to present the effect of actuation analytically before going over the development of the nonlinear finite element code and simulation [21].

4.6.1 Small Deformation of an Internally Actuated Beam

The linearized equilibrium equations are obtained from Eqs. (41) and (43) by keeping only linear terms of unknowns:

$$\frac{dN_1(S)}{dS} + \hat{n}_1(S) = 0, \tag{58a}$$

$$\frac{dN_2(S)}{dS} + \hat{n}_2(S) = 0, \tag{58b}$$

$$\frac{dM_3(S)}{dS} + N_2(s) + \hat{m}_3(S) = 0. \tag{59}$$

We consider the deformation of the beam from the straight reference configuration. For small axial and transverse displacements $u(S)$ and $v(S)$, respectively, the deformed position of the curve of centroids is expressed as:

$$\mathbf{r}_C(S) = \mathbf{e}^I \begin{pmatrix} S + u(S) \\ v(S) \end{pmatrix}. \tag{60a}$$

The linearized tangent vector is computed by neglecting all nonlinear terms as:

$$\widehat{\boldsymbol{\gamma}}(S) = \mathbf{e}(S) \begin{pmatrix} \hat{\gamma}_1(S) \\ \hat{\gamma}_2(S) \end{pmatrix} = \frac{d\mathbf{r}_C(S)}{dS}, \tag{60b}$$

$$\frac{d\mathbf{r}_C(S)}{dS} = \mathbf{e}^I \begin{pmatrix} 1 + \dfrac{du(S)}{dS} \\ \dfrac{dv(S)}{dS} \end{pmatrix} = \mathbf{e}(S) \begin{bmatrix} \cos\psi(S) & \sin\psi(S) \\ -\sin\psi(S) & \cos\psi(S) \end{bmatrix} \begin{pmatrix} 1 + \dfrac{du(S)}{dS} \\ \dfrac{dv(S)}{dS} \end{pmatrix}$$

$$= \mathbf{e}(S) \begin{bmatrix} 1 & \psi(S) \\ -\psi(S) & 1 \end{bmatrix} \begin{pmatrix} 1 + \frac{du(S)}{dS} \\ \frac{dv(S)}{dS} \end{pmatrix} = \mathbf{e}(S) \begin{pmatrix} 1 + \frac{du(S)}{dS} \\ \frac{dv(S)}{dS} - \psi(S) \end{pmatrix}, \tag{60c}$$

Equations (60b, c) yield

$$\begin{pmatrix} \hat{\gamma}_1(S) \\ \hat{\gamma}_2(S) \end{pmatrix} = \begin{pmatrix} 1 + \frac{du(S)}{dS} \\ \frac{dv(S)}{dS} - \psi(S) \end{pmatrix}. \tag{60d}$$

The beam constitutive relations, Eqs. (51a, b) with Eq. (60d) become

$$N_1(S) = EA \frac{du(S)}{dS}, \tag{61a}$$

$$N_2(S) = GA_s \left(\frac{dv(S)}{dS} - \psi(S) \right). \tag{61b}$$

The moment constitutive relation is obtained from Eq. (52) as

$$M_3 = EI_3 \frac{d\psi(S)}{dS}. \tag{62}$$

The beam equilibrium Eqs. (58b) and (59) with the constitutive equation (61b) and Eq. (62) define the *Timoshenko beam theory* [22, 23], which incorporate the effect of

transverse shear deformation, $\hat{\gamma}_2 \neq 0$, for passive thick beams. However, for passive thin beams, it has been observed that the transverse shear deformation is negligible. This indicates that the normal plane to the line of centroids remain normal during deformation, $\hat{\gamma}_2 = 0$. As a result, the angle of frame rotation is expressed by the derivative of the deflection: $\psi(S) = dv/dS$. The resulting beam equations reduce to those of the *Euler-Bernoulli beam theory*.

Using the active Timoshenko beam equations, we consider a cantilever beam, which is fixed at $S = 0$ and free at $S = L$, as shown in Fig. 3a. The boundary conditions are

$$u = v = \psi = 0 \text{ at } S = 0. \tag{63}$$

$$N_1 = N_2 = M_3 = 0 \text{ at } S = L. \tag{64}$$

The beam is subjected to a uniform transverse load, expressed as: $\hat{n}_2(S) = -q_0$, $\hat{n}_1(S) = 0$, and $\hat{m}_3(S) = 0$ in Eqs. (58a-b) and Eq. (59). We then actuate the beam with constant actuation-curvature $\kappa^{\#}$ and illustrate the loaded beam being lifted as one incrementally increases the value of $\kappa^{\#}$.

Taking advantage of the linearity of the problem, we superpose the two solutions: (i) $\{u_p(S) \quad v_P(S) \quad \psi_P(S)\}$ for a passive beam under uniformly distributed load $\hat{n}_2 = -q_0$, and (ii) $\{u_A(S) \quad v_A(S) \quad \psi_A(S)\}$ for an actuated beam with constant actuation curvature $\kappa_0^{\#}$. The passive beam solution is

$$\big(N_1(S)\big)_P = 0, \tag{65a}$$

$$\big(N_2(S)\big)_P = q_0(S - L), \tag{65b}$$

$$\big(M_3(S)\big)_P = -\tfrac{q_0}{2}(S - L)^2, \tag{65c}$$

$$\big(u(S)\big)_P = 0, \tag{65d}$$

$$\big(v(S)\big)_P = -\frac{q_0}{6EI_3}\left\{\frac{1}{4}(S-L)^4 + L^3S - \frac{1}{4}L^4\right\} + \frac{q_0}{2GA_s}\{(S-L)^2 - L^2\}, \tag{65e}$$

$$\big(\psi(S)\big)_P = -\frac{q_0}{6EI_3}\{(S-L)^3 + L^3\}, \tag{65f}$$

The transverse displacement of the passive beam solution is shown as the black line in Fig. 5b. The material properties used were $E = 30e6$ psi, $G = 12e6$ psi, and a distributed load of $q_0 = 200$ lb/in. The active solution is:

$$\big(N_1(S)\big)_A = \big(N_2(S)\big)_A = \big(M_3(S)\big)_A = 0, \tag{66a-c}$$

$$\big(u(S)\big)_A = 0, \tag{66d}$$

$$\big(v(S)\big)_A = \frac{1}{2}\kappa_0^{\#}S^2, \tag{66e}$$

$$\big(\psi(S)\big)_A = \kappa_0^{\#}S. \tag{66f}$$

To express the incremental actuation on the passively loaded beam, the superposed solutions are expressed as:

$$\begin{pmatrix} u(S) \\ v(S) \\ \psi(S) \end{pmatrix} = \begin{pmatrix} \big(u(S)\big)_P \\ \big(v(S)\big)_P \\ \big(\psi(S)\big)_P \end{pmatrix} + \alpha \begin{pmatrix} \big(u(S)\big)_A \\ \big(v(S)\big)_A \\ \big(\psi(S)\big)_A \end{pmatrix}, \tag{67}$$

where the actuation parameter is incrementally increased from $\alpha = 0$ to 1. The deformed configurations of the incrementally activated beam with an actuation constant of $\kappa_0^{\#} = 0.0002$ are demonstrated by the green lines shown in Fig. 5b.

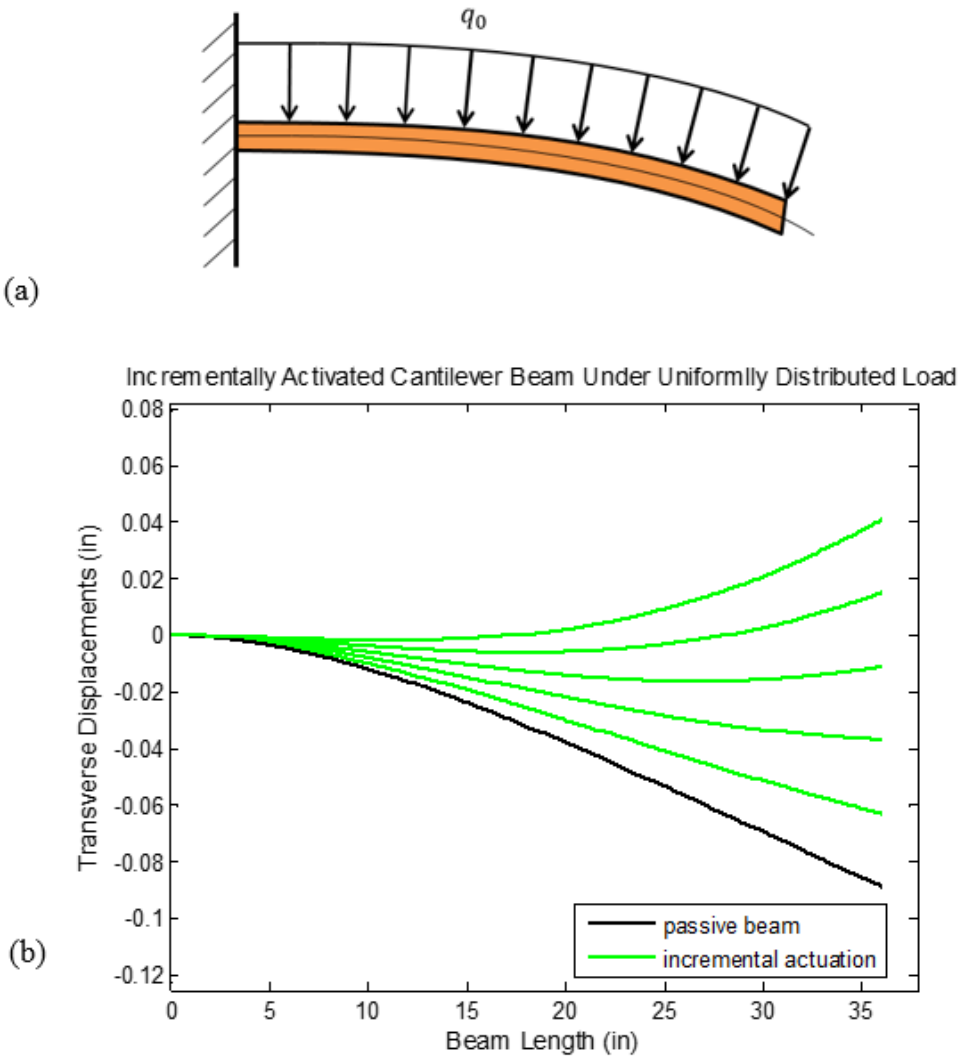

Figure 4-5: (a) Passive cantilever beam under a uniformly distributed load and (b) Transverse displacement of an incrementally activated linear cantilever beam under a uniformly distributed load

In the sections to follow, the nonlinear finite element equations of motion will be derived and applied to simulate the motion of an inchworm.

4.7 Development of Active $C^{(1)}$-Beam Elements

The configuration of a curved beam at time *t* is described by $\mathbf{r}_C(S,t) = \mathbf{e}^I z_C(S,t)$ in Eq. (31), and the attitude of the moving frame $\mathbf{e}(S,t)$ in Eq. (33a), expressed by $\psi(S,t)$

. Both $z_C(S,t)$ and $\psi(S,t)$ are smooth functions. However, after FE discretization of the curve of centroids by using beam elements, those values in each element are interpolated by their nodal values, z_C and ψ. As a result, on the discretized curve of centroids, $z_C(S,t)$ and $\psi(S,t)$ become contiguous functions, *i.e.*, the continuity of their *S*-derivatives are not satisfied. This yields C^0-beam elements, which does not satisfy the continuity of the tangent vector to the curve of centroids [26,27]. In active beams, actuation curvatures, without transverse shear deformation, are represented by the second *S*-derivatives of $z_C(S,t)$. Therefore, C^0-beam elements are not satisfactory for describing internal actuation curvature of active beams.

In the proposed active C^1-beam element, the nodal displacements and their shape functions employed to approximate $z_C(S,t)$ and $\psi(S,t)$, are selected to satisfy the following two criteria: (i) after FE discretization, the curve of centroids of a beam under investigation is expressed by a C^1-curve, and (ii) the shape functions used for the interpolation of $\psi(S,t)$ are consistent with the shape functions adopted for $z_C(S,t)$ so that analytical solutions are obtained for a cantilever beam subjected to an end load [28] and for a simply supported beam with a mid-span load [29].

First, to facilitate the C^1-continuity of the curve of centroids, the components $z_C' \equiv \partial z_C / \partial S$ of the tangent vector, $\hat{\gamma}$ in Eq. (36), are included in the nodal displacements in addition to z_C and ψ. As a matter of fact, in linear Euler-Bernoulli beam elements, C^1-interpolation of transverse displacements has been achieved by using cubic shape functions

[30]. In the present active C^1-beam element, a cubic C^1-interpolation is employed for both $z_{1C}(S,t)$ and $z_{2C}(S,t)$.

Second, to achieve a consistent interpolation of $\psi(S,t)$ with that used for $z_C(S,t)$, the analytical solutions of active Timoshenko-beam equations for a cantilever beam [28] and a simply supported beam [29] were closely investigated. It was found that the shape functions of $\psi(S,t)$ must be quadratic since both z_{1C} and z_{2C} are interpolated by cubic shape functions. To achieve the quadratic interpolation, a mid-point node with the nodal value of ψ is introduced for the interpolation of $\psi(S,t)$. Using this set of interpolations for $z_C(S,t)$ and $\psi(S,t)$, the analytical solution for an active cantilever beam loaded at its tip is reproduced by a single beam element, and that of a simply supported beam loaded by a mid-span load is obtained by a two-element model.

4.7.1 FE Representation of the Curve of Centroids and the Moving Frame

At time *t*=0, a beam is considered to be in a straight configuration. Its reference line of centroids is discretized into N_{el} elements, whereby the element numbers range from (*e*) =1 to N_{el}. In element (*e*), arc length increases from $S^{(e)}$=0 to the element length $L_0^{(e)}$, i.e., $0 \le S^{(e)} \le L_0^{(e)}$ after translating the origin of *S* to node $\hat{1}$. At time *t*, the same $S^{(e)}$ is used as an arc-parameter in element (*e*).

A representative, three-node C^1-beam element (*e*) is defined by two end nodes, node $\hat{1}$ and node $\hat{2}$, and a middle node $\hat{3}$, as shown in Fig. 6.

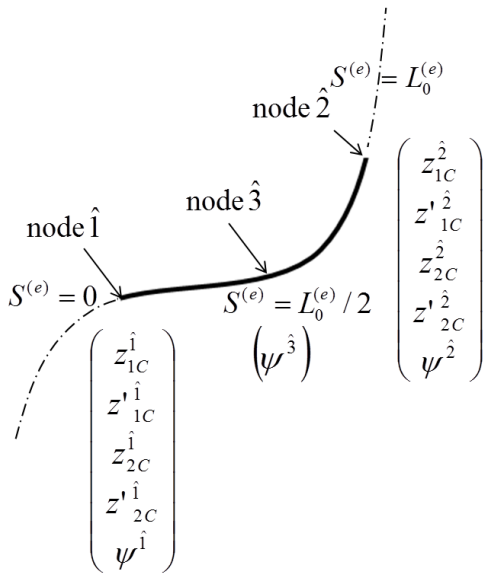

Figure 4-6: A three-node C^1-beam element with 11 nodal displacements

First, to accomplish C^1-connection of the curve of centroids at each shared node by adjacent elements, four nodal displacements: $\left(z_{1C}^{\hat{j}} \quad z'^{\hat{j}}_{1C} \quad z_{2C}^{\hat{j}} \quad z'^{\hat{j}}_{2C}\right)^T$ for nodes $\hat{j}=\hat{1}$ and $\hat{2}$ are used, where the prime denotes the *S*-derivative of the primed variable, such as $z'^{\hat{j}}_{1C} \equiv \partial z_{1C}^{\hat{j}} / \partial S$ at node $\hat{j}$. It can be observed that due to the simple translational relation of the origin, $\partial S^{(e)} / \partial S \equiv 1$. In element (*e*) with the element length $L_0^{(e)}$ at *t*=0, the *z*-coordinates of the position vector, $\mathbf{r}_C(S,t) = \mathbf{e}^I z_C(S,t)$ are interpolated by using the elemental *z*-nodal displacements $\left(\hat{d}_z^{(e)}(t)\right)$ through the matrix of z-shape functions $\left[\overline{N_z}\right]$ as:

$$\underset{2\times 1}{z_C^{(e)}}(S^{(e)},t) \equiv \begin{pmatrix} z_{1C}^{(e)} \\ z_{2C}^{(e)} \end{pmatrix}(S^{(e)},t) = \left[\underset{2\times 8}{\overline{N_z}}(S^{(e)},L_0^{(e)})\right]\left(\underset{8\times 1}{\hat{d}_z^{(e)}(t)}\right). \tag{68a}$$

The elemental nodal z-displacements $\left(\hat{d}_z^{(e)}(t)\right)$ are grouped for each *z*-component as:

$$\underset{8\times1}{\left(\hat{d}_{z}^{(e)}(t)\right)}\equiv\begin{pmatrix}\underset{4\times1}{\hat{d}_{1z}^{(e)}(t)}\\ \underset{4\times1}{\hat{d}_{2z}^{(e)}(t)}\end{pmatrix}, \tag{68b}$$

$$\underset{4\times1}{\left(\hat{d}_{1z}^{(e)}(t)\right)}\equiv\begin{pmatrix}\hat{z}_{1C}^{1}(t)\\ \hat{z'}_{1C}^{1}(t)\\ \hat{z}_{1C}^{2}(t)\\ \hat{z'}_{1C}^{2}(t)\end{pmatrix}, \tag{68c}$$

$$\underset{4\times1}{\left(\hat{d}_{2z}^{(e)}(t)\right)}\equiv\begin{pmatrix}\hat{z}_{2C}^{1}(t)\\ \hat{z'}_{2C}^{1}(t)\\ \hat{z}_{2C}^{2}(t)\\ \hat{z'}_{2C}^{2}(t)\end{pmatrix}, \tag{68d}$$

The matrix of z-shape functions for the curve of centroids, $\left[\overline{N_z}\right]$, is defined as:

$$\underset{2\times8}{\left[\overline{N_z}(S^{(e)},L_0^{(e)})\right]}\equiv\begin{bmatrix}\underset{1\times4}{\tilde{N}(S^{(e)},L_0^{(e)})} & \underset{1\times4}{0}\\ \underset{1\times4}{0} & \underset{1\times4}{\tilde{N}(S^{(e)},L_0^{(e)})}\end{bmatrix}. \tag{69a}$$

The sub-matrix of shape functions $\left[\tilde{N}(S^{(e)},L_0^{(e)})\right]$ in Eq. (69a) is defined as:

$$\underset{1\times4}{\tilde{N}(S^{(e)},L_0^{(e)})}\equiv\left[\tilde{N}_1(S^{(e)},L_0^{(e)})\quad\tilde{N}_2(S^{(e)},L_0^{(e)})\quad\tilde{N}_3(S^{(e)},L_0^{(e)})\quad\tilde{N}_4(S^{(e)},L_0^{(e)})\right], \tag{69b}$$

and the four shape functions, which enable C^1-interpolation of the curve of centroids are

$$\tilde{N}_1(S^{(e)},L_0^{(e)})=1-3\left(\frac{S^{(e)}}{L_0^{(e)}}\right)^2+2\left(\frac{S^{(e)}}{L_0^{(e)}}\right)^3, \tag{69c}$$

$$\tilde{N}_2(S^{(e)},L_0^{(e)})=S^{(e)}\left\{\left(\frac{S^{(e)}}{L_0^{(e)}}\right)-1\right\}^2, \tag{69d}$$

$$\tilde{N}_3(S^{(e)},L_0^{(e)})=\left(\frac{S^{(e)}}{L_0^{(e)}}\right)^2\left\{3-2\left(\frac{S^{(e)}}{L_0^{(e)}}\right)\right\}, \tag{69e}$$

$$\tilde{N}_4(S^{(e)}, L_0^{(e)}) = \frac{\left(S^{(e)}\right)^2}{L_0^{(e)}} \left\{ \left(\frac{S^{(e)}}{L_0^{(e)}} \right) - 1 \right\}. \tag{69f}$$

Second, the attitude angle $\psi(S,t)$ of the moving frame $\mathbf{e}(S,t)$ is interpolated by using the nodal values at both end-nodes and the middle node:

$$\psi(S^{(e)}, t) = \left[\underset{1\times 3}{\overline{N_\psi}}(S^{(e)}, L_0^{(e)}) \right] \left(\Psi^{(e)}(t) \right), \tag{70a}$$

where the nodal ψ-displacements $(\Psi^{(e)})$ and the matrix of ψ-shape functions $\left[\overline{N_\psi}\right]$ are defined, respectively,

$$\left(\Psi^{(e)}(t) \right) \equiv \begin{pmatrix} \psi^{\hat{1}}(t) \\ \psi^{\hat{2}}(t) \\ \psi^{\hat{3}}(t) \end{pmatrix}, \tag{70b}$$

$$\left[\underset{1\times 3}{\overline{N_\psi}}(S^{(e)}, L_0^{(e)}) \right] \equiv \left[\breve{N}^{\hat{1}}(S^{(e)}, L_0^{(e)}) \quad \breve{N}^{\hat{2}}(S^{(e)}, L_0^{(e)}) \quad \breve{N}^{\hat{3}}(S^{(e)}, L_0^{(e)}) \right], \tag{70c}$$

and the quadratic shape functions are

$$\breve{N}^{\hat{1}}(S^{(e)}, L_0^{(e)}) = \left(2\frac{S^{(e)}}{L_0^{(e)}} - 1 \right) \left(\frac{S^{(e)}}{L_0^{(e)}} - 1 \right), \tag{70d}$$

$$\breve{N}^{\hat{2}}(S^{(e)}, L_0^{(e)}) = \frac{S^{(e)}}{L_0^{(e)}} \left(2\frac{S^{(e)}}{L_0^{(e)}} - 1 \right), \tag{70e}$$

$$\breve{N}^{\hat{3}}(S^{(e)}, L_0^{(e)}) = 4\frac{S^{(e)}}{L_0^{(e)}} \left(1 - \frac{S^{(e)}}{L_0^{(e)}} \right). \tag{70f}$$

In summary, $z_C(S,t)$ in each element is interpolated by using 8 nodal z-coordinates in Eq. (68a), and $\psi(S,t)$ is interpolated by using three nodal ψ-coordinates in

Eq. (70a). Their interpolations are collectively expressed by using 11 nodal displacements $\left(\hat{d}^{(e)}(t)\right)$ and the matrix of shape functions $\left[\overline{\overline{N}}\right]$ as:

$$\begin{pmatrix} z_C(S^{(e)},t) \\ {\scriptstyle 2\times 1} \\ \psi(S^{(e)},t) \\ {\scriptstyle 1\times 1} \end{pmatrix} = \left[\underset{3\times 11}{\overline{\overline{N}}}(S^{(e)},L_0^{(e)}) \right] \left(\underset{11\times 1}{\hat{d}^{(e)}(t)} \right), \tag{71a}$$

where the matrix of shape functions $\left[\overline{\overline{N}}\right]$ is defined as

$$\left[\underset{3\times 11}{\overline{\overline{N}}}(S^{(e)},L_0^{(e)}) \right] = \begin{bmatrix} \underset{2\times 8}{\overline{N_z}}(S^{(e)},L_0^{(e)}) & \underset{2\times 3}{0} \\ \underset{1\times 8}{0} & \underset{1\times 3}{\overline{N_\psi}}(S^{(e)},L_0^{(e)}) \end{bmatrix}, \tag{71b}$$

and the nodal displacements, $\left(\hat{d}^{(e)}(t)\right)$, are defined as

$$\left(\underset{11\times 1}{\hat{d}^{(e)}(t)} \right) \equiv \begin{pmatrix} \underset{8\times 1}{\hat{d}_z^{(e)}(t)} \\ \underset{3\times 1}{\Psi^{(e)}(t)} \end{pmatrix} \equiv \begin{pmatrix} \underset{4\times 1}{\hat{d}_{1z}^{(e)}(t)} \\ \underset{4\times 1}{\hat{d}_{2z}^{(e)}(t)} \\ \underset{3\times 1}{\Psi^{(e)}(t)} \end{pmatrix}. \tag{71c}$$

The second time derivative of Eq. (71a) is expressed in terms of nodal accelerations as:

$$\frac{\partial^2}{\partial t^2} \begin{pmatrix} z_C(S^{(e)},t) \\ {\scriptstyle 2\times 1} \\ \psi(S^{(e)},t) \\ {\scriptstyle 1\times 1} \end{pmatrix} = \left[\underset{3\times 11}{\overline{\overline{N}}}(S^{(e)},L_0^{(e)}) \right] \frac{d^2}{dt^2} \left(\underset{11\times 1}{\hat{d}^{(e)}(t)} \right). \tag{72}$$

4.7.2 FE Representation of Beam Strain Variables

The beam strain variables are $\hat{\gamma}_1(S^{(e)},t)$ and $\hat{\gamma}_2(S^{(e)},t)$ in Eq. (36) and $\kappa_3(S^{(e)},t)$. These strains are conjugate to the beam stress variables: $N_1(S^{(e)},t)$, $N_2(S^{(e)},t)$, and $M_3(S^{(e)},t)$, respectively.

Using the FE representation of the curve of centroids in element (*e*), Eq. (68a), its *S*-derivative is also expressed by the nodal z-coordinates:

$$\frac{\partial z_C^{(e)}(S^{(e)},t)}{\partial S} \equiv \left[\underset{2\times 8}{\overline{N_z}'}(S^{(e)},L_0^{(e)})\right]\left(\underset{8\times 1}{\hat{d}_z^{(e)}(t)}\right), \tag{73a}$$

where $\left[\overline{N_z}'\right]$ denotes the *S*-derivative of the sub matrices of z-shape functions as:

$$\left[\underset{2\times 8}{\overline{N_z}'}(S^{(e)},L_0^{(e)})\right] \equiv \begin{bmatrix} \underset{1\times 4}{\tilde{N}'(S^{(e)},L_0^{(e)})} & \underset{1\times 4}{0} \\ \underset{1\times 4}{0} & \underset{1\times 4}{\tilde{N}'(S^{(e)},L_0^{(e)})} \end{bmatrix}, \tag{73b}$$

$$\underset{1\times 4}{\tilde{N}'(S^{(e)},L_0^{(e)})} \equiv \left[\frac{\partial \tilde{N}_1(S^{(e)},L_0^{(e)})}{\partial S} \quad \frac{\partial \tilde{N}_2(S^{(e)},L_0^{(e)})}{\partial S} \quad \frac{\partial \tilde{N}_3(S^{(e)},L_0^{(e)})}{\partial S} \quad \frac{\partial \tilde{N}_4(S^{(e)},L_0^{(e)})}{\partial S}\right]. \tag{73c}$$

Now, the components of the tangent vector in Eq. (6c) are expressed by nodal displacements using Eqs. (70a) for $R(\psi)$ and (73a, b):

$$\hat{\gamma}(S^{(e)},t) = R^T(\psi(S^{(e)},t))\left[\underset{2\times 8}{\overline{N_z}'}(S^{(e)},L_0^{(e)})\right]\left(\underset{8\times 1}{\hat{d}_z^{(e)}(t)}\right), \tag{74a}$$

and in expanded form, the axial and shear strain components become

$$\begin{pmatrix} \hat{\gamma}_1(S^{(e)},t) \\ \hat{\gamma}_2(S^{(e)},t) \end{pmatrix} = \begin{bmatrix} \cos\psi(S^{(e)},t) & \sin\psi(S^{(e)},t) \\ -\sin\psi(S^{(e)},t) & \cos\psi(S^{(e)},t) \end{bmatrix}$$

$$\times \begin{bmatrix} \underset{1\times 4}{\tilde{N}'(S^{(e)},L_0^{(e)})} & \underset{1\times 4}{0} \\ \underset{1\times 4}{0} & \underset{1\times 4}{\tilde{N}'(S^{(e)},L_0^{(e)})} \end{bmatrix} \begin{pmatrix} \hat{d}_{1z}^{(e)}(t) \\ \hat{d}_{2z}^{(e)}(t) \end{pmatrix}. \tag{74b}$$

Next, the curvature is expressed by the nodal angular displacements by taking the S-derivative of Eq. (70a)

$$\kappa_3(S^{(e)},t) \equiv \frac{\partial \psi(S^{(e)},t)}{\partial S} = \left[\underset{1\times 3}{\overline{N_\psi}'}(S^{(e)},L_0^{(e)})\right]\left(\Psi^{(e)}(t)\right), \tag{75a}$$

where the prime applied to the matrix of ψ-shape functions implies the S-derivative of each shape function:

$$\left[\underset{1\times 3}{\overline{N_{\psi}}}'(S^{(e)},L_0^{(e)})\right]\equiv\left[\frac{\partial\breve{N}^{\hat{1}}(S^{(e)},L_0^{(e)})}{\partial S}\quad\frac{\partial\breve{N}^{\hat{2}}(S^{(e)},L_0^{(e)})}{\partial S}\quad\frac{\partial\breve{N}^{\hat{3}}(S^{(e)},L_0^{(e)})}{\partial S}\right]. \qquad (75b)$$

As a result, the beam strains are expressed by nodal displacements through the $[B^{(e)}]$-matrix, combining Eqs. (74a) and (75a):

$$\begin{pmatrix}\hat{\gamma}_1(S^{(e)},t)\\ \hat{\gamma}_2(S^{(e)},t)\\ \kappa_3(S^{(e)},t)\end{pmatrix}=\left[B^{(e)}(S^{(e)},t)\right]\left(\hat{d}^{(e)}(t)\right), \qquad (76a)$$

where the $[B^{(e)}]$-matrix relates the beam strains to nodal displacements of element (e):

$$\left[B^{(e)}(S^{(e)},t)\right]=\begin{bmatrix}\cos\psi(S^{(e)},t)\underset{1\times 4}{\tilde{N}'}(S^{(e)},L_0^{(e)}) & \sin\psi(S^{(e)},t)\underset{1\times 4}{\tilde{N}'}(S^{(e)},L_0^{(e)}) & \underset{1\times 3}{0}\\ -\sin\psi(S^{(e)},t)\underset{1\times 4}{\tilde{N}'}(S^{(e)},L_0^{(e)}) & \cos\psi(S^{(e)},t)\underset{1\times 4}{\tilde{N}'}(S^{(e)},L_0^{(e)}) & \underset{1\times 3}{0}\\ \underset{1\times 4}{0} & \underset{1\times 4}{0} & \underset{1\times 3}{\overline{N_{\psi}}'}(S^{(e)},L_0^{(e)})\end{bmatrix}. \qquad (76b)$$

4.7.3 FE Representation of Virtual Displacements

Next, the virtual displacements $\delta z_C(S,t)$ and $\delta\psi(S,t)$ are expressed by nodal virtual displacements. Since the shape functions are fixed, the variation of Eq. (71a) only applies to nodal displacements.

$$\begin{pmatrix}\underset{2\times 1}{\delta z_C(S^{(e)},t)}\\ \underset{1\times 1}{\delta\psi(S^{(e)},t)}\end{pmatrix}=\left[\underset{3\times 11}{\overline{\overline{N}}}(S^{(e)},L_0^{(e)})\right]\left(\underset{11\times 1}{\delta\hat{d}^{(e)}(t)}\right), \qquad (77a)$$

where the elemental virtual nodal-displacement (column) matrices are defined as:

$$\underset{11\times 1}{\left(\delta\hat{d}^{(e)}(t)\right)} \equiv \begin{pmatrix} \underset{8\times 1}{\delta\hat{d}_z^{(e)}(t)} \\ \underset{3\times 1}{\delta\Psi^{(e)}(t)} \end{pmatrix} \equiv \begin{pmatrix} \underset{4\times 1}{\delta\hat{d}_{1z}^{(e)}(t)} \\ \underset{4\times 1}{\delta\hat{d}_{2z}^{(e)}(t)} \\ \underset{3\times 1}{\delta\Psi^{(e)}(t)} \end{pmatrix}, \tag{77b}$$

$$\underset{8\times 1}{\left(\delta\hat{d}_z^{(e)}(t)\right)} \equiv \begin{pmatrix} \underset{4\times 1}{\delta\hat{d}_{1z}^{(e)}(t)} \\ \underset{4\times 1}{\delta\hat{d}_{2z}^{(e)}(t)} \end{pmatrix}, \tag{77c}$$

$$\underset{4\times 1}{\left(\delta\hat{d}_{1z}^{(e)}(t)\right)} \equiv \begin{pmatrix} \delta z_{1C}^{\hat{1}}(t) \\ \delta z'^{\hat{1}}_{1C}(t) \\ \delta z_{1C}^{\hat{2}}(t) \\ \delta z'^{\hat{2}}_{1C}(t) \end{pmatrix}, \tag{77d}$$

$$\underset{4\times 1}{\left(\delta\hat{d}_{2z}^{(e)}(t)\right)} \equiv \begin{pmatrix} \delta z_{2C}^{\hat{1}}(t) \\ \delta z'^{\hat{1}}_{2C}(t) \\ \delta z_{2C}^{\hat{2}}(t) \\ \delta z'^{\hat{2}}_{2C}(t) \end{pmatrix}. \tag{77e}$$

4.7.4 FE Representation of Virtual Beam-Strains

The objective here is to compute $\delta\hat{\gamma}$ and $\delta\kappa_3$ in a representative element (e), and express them in terms of the nodal virtual displacements $(\delta\hat{d}^{(e)}(t))$ through the $[B_T^{(e)}]$-matrix:

$$\begin{pmatrix} \delta\hat{\gamma}_1(S^{(e)},t) \\ \delta\hat{\gamma}_2(S^{(e)},t) \\ \delta\kappa_3(S^{(e)},t) \end{pmatrix} = \underset{3\times 11}{\left[\ B_T^{(e)}(S^{(e)},L_0^{(e)})\ \right]} \begin{pmatrix} \delta\hat{d}_{1z}^{(e)}(t) \\ \delta\hat{d}_{2z}^{(e)}(t) \\ \delta\Psi^{(e)}(t) \end{pmatrix}. \tag{78a}$$

The variation of Eq. (74a) using Eq. (45b) for $\delta\hat{\gamma}$, and the variation of Eq. (27a) for $\delta\kappa_3$ yield

$$\left[\underset{3\times 11}{B_T^{(e)}}(S^{(e)},L_0^{(e)})\right]=\begin{bmatrix} \cos\psi\ \underset{1\times 4}{\tilde{N}'}(S^{(e)},L_0^{(e)}) & \sin\psi\ \underset{1\times 4}{\tilde{N}'}(S^{(e)},L_0^{(e)}) & \hat{\gamma}_2\ \underset{1\times 3}{\overline{N_\psi}}(S^{(e)},L_0^{(e)}) \\ -\sin\psi\ \underset{1\times 4}{\tilde{N}'}(S^{(e)},L_0^{(e)}) & \cos\psi\ \underset{1\times 4}{\tilde{N}'}(S^{(e)},L_0^{(e)}) & -\hat{\gamma}_1\ \underset{1\times 3}{\overline{N_\psi}}(S^{(e)},L_0^{(e)}) \\ \underset{1\times 4}{0} & \underset{1\times 4}{0} & \underset{1\times 3}{\overline{N_\psi}'}(S^{(e)},L_0^{(e)}) \end{bmatrix}, \quad (78b)$$

where $\hat{\gamma}_1$, $\hat{\gamma}_1$, and ψ are functions of $S^{(e)}$ and *t*.

It is noted that $[B_T^{(e)}]$ differs from $[B^{(e)}]$ in Eq. (76b) in the (1,3) and (2, 3) elements. Next, a nonlinear system of beam equations of motion is obtained from the principle of virtual work, incorporating the FE representation of displacements and strain variables.

4.8 Nonlinear FE Equations of Motion

A curve of centroids has been divided into N_{el} three-node beam elements. The spatial integrations in the principle of virtual work are all performed element-wise by using four-point Gauss quadrature. As a result, integrands are only evaluated at the Gauss integration points in each element [30-32].

$$\sum_{e=1}^{N_{el}}\int_0^{L_0^{(e)}}\left(\delta\hat{\gamma}_1(S^{(e)},t)\quad \delta\hat{\gamma}_2(S^{(e)},t)\quad \delta\kappa_3(S^{(e)},t)\right)\begin{pmatrix} N_1(S^{(e)},t)\\ N_2(S^{(e)},t)\\ M_3(S^{(e)},t)\end{pmatrix}dS^{(e)}$$

$$=\sum_{e=1}^{N_{el}}\int_0^{L_0^{(e)}}\left(\left(\delta z_C(S^{(e)},t)\right)^T\quad \delta\psi(S^{(e)},t)\right)\begin{pmatrix}\hat{n}^I(S^{(e)},t)\\ \hat{m}_3(S^{(e)},t)\end{pmatrix}dS^{(e)}$$

$$-\sum_{e=1}^{N_{el}}\int_0^{L_0^{(e)}}\left(\left(\delta z_C(S^{(e)},t)\right)^T\quad \delta\psi(S^{(e)},t)\right)\begin{pmatrix}\mathsf{m}_{\mathsf{A}(0)}\dfrac{\partial^2 z_C(S^{(e)},t)}{\partial t^2}\\ J_{3C(0)}\dfrac{\partial^2\psi(S^{(e)},t)}{\partial t^2}\end{pmatrix}dS^{(e)}$$

$$+\left\{\left(\delta z_C(S,t)\right)^T\ \hat{n}_E^I(S,t)+\delta\psi(S,t)\,\hat{m}_E(S,t)\right|_{S=0}^{L_0}. \quad (79)$$

The first integral in Eq. (79) expresses the virtual strain energy of element (e) and defines the *elemental internal force* $(\hat{P}^{(e)}(t))$ as follows:

$$\left(\delta \hat{d}^{(e)}(t)\right)^T \left(\hat{P}^{(e)}(t)\right) \equiv \int_0^{L_0^{(e)}} \left(\delta\hat{\gamma}_1(S^{(e)},t) \quad \delta\hat{\gamma}_2(S^{(e)},t) \quad \delta\kappa_3(S^{(e)},t)\right) \begin{pmatrix} N_1(S^{(e)},t) \\ N_2(S^{(e)},t) \\ M_3(S^{(e)},t) \end{pmatrix} dS^{(e)}. \quad (80a)$$

The substitution of Eq. (78a) into the above defines the internal force of element (e):

$$\underset{1\times 1}{\left(\hat{P}^{(e)}(t)\right)} \equiv \int_0^{L_0^{(e)}} \underset{3\times 1}{\left[B_T^{(e)}(t)\right]^T} \begin{pmatrix} N_1(S^{(e)},t) \\ N_2(S^{(e)},t) \\ M_3(S^{(e)},t) \end{pmatrix} dS^{(e)}. \quad (80b)$$

The second integral in Eq. (79) expresses the virtual work done by the distributed loads and defines the *external nodal force due to distributed loads* (including body forces), $(\hat{F}_B^{(e)}(t))$:

$$\left(\delta \hat{d}^{(e)}(t)\right)^T \left(\hat{F}_B^{(e)}(t)\right) \equiv \int_0^{L_0^{(e)}} \left(\left(\delta z_C(S^{(e)},t)\right)^T \quad \delta\psi(S^{(e)},t)\right) \begin{pmatrix} \hat{n}^I(S^{(e)},t) \\ \hat{m}_3(S^{(e)},t) \end{pmatrix} dS^{(e)}. \quad (81a)$$

The substitution of Eq. (77a) into Eq. (81a) defines $(\hat{F}_B^{(e)}(t))$ as:

$$\underset{1\times 1}{\left(\hat{F}_B^{(e)}(t)\right)} = \int_0^{L_0^{(e)}} \underset{3\times 1}{\left[\overline{\overline{N}}(S^{(e)},L_0^{(e)})\right]^T} \begin{pmatrix} \underset{2\times 1}{\hat{n}^I(S^{(e)},t)} \\ \underset{1\times 1}{\hat{m}_3(S^{(e)},t)} \end{pmatrix} dS^{(e)}. \quad (81b)$$

The third integral represents the virtual work by inertial forces and defines the element mass matrix $[\hat{M}^{(e)}]$ as:

$$\left(\delta\hat{d}^{(e)}(t)\right)^T\left[\hat{M}^{(e)}\right]\frac{d^2}{dt^2}\left(\hat{d}^{(e)}(t)\right)\equiv\int_0^{L_0^{(e)}}\left(\left(\delta z_C(S^{(e)},t)\right)^T\quad\delta\psi(S^{(e)},t)\right)\begin{pmatrix}\mathsf{m}_{A(0)}\dfrac{\partial^2 z_C(S^{(e)},t)}{\partial t^2}\\ J_{3C(0)}\dfrac{\partial^2\psi(S^{(e)},t)}{\partial t^2}\end{pmatrix}dS^{(e)}\ .(82)$$

Using Eqs. (77a), (72), and (71b), the mass matrix is defined as:

$$\underset{11\times11}{\left[\hat{M}^{(e)}\right]}\equiv\int_0^{L_0^{(e)}}\begin{bmatrix}\overline{\overline{N}}_z(S^{(e)},L_0^{(e)}) & 0\\ 0 & \overline{\overline{N}}_\psi(S^{(e)},L_0^{(e)})\end{bmatrix}^T\begin{bmatrix}\mathsf{m}_{A(0)}\overline{\overline{N}}_z(S^{(e)},L_0^{(e)}) & 0\\ 0 & J_{3C(0)}\overline{\overline{N}}_\psi(S^{(e)},L_0^{(e)})\end{bmatrix}dS^{(e)}$$

.(83)

The mass matrix is evaluated analytically yielding constant components, as shown in the Appendix.

The global (arbitrary) virtual-displacements $(\delta d(t))$ are assembled from elemental virtual displacements $\left(\delta\hat{d}^{(e)}(t)\right)$ utilizing the element connectivity data (defined during mesh generation). In this assembly, vanishing virtual displacements are excluded, observing that virtual nodal displacements vanish when their nodal values are prescribed. Corresponding to $(\delta d(t))$, the global, unknown nodal-displacements are expressed as $(d(t))$, assembled from $\left(\hat{d}^{(e)}(t)\right)$, see for example, [30,31].

The last term in Eq. (79) defines the nodal force $(F_E(t))$ due to external forces acting on the boundaries of the beam at *S=0* and L_0:

$$\left(\delta d(t)\right)^T\left(F_E(t)\right)\equiv\left\{\left(\delta z_C(S,t)\right)^T\hat{n}^I(S,t)+\delta\psi(S,t)\,\hat{m}_E(S,t)\right\}\Big|_{S=0}^{L_0}\ . \qquad (84)$$

Equation (79) is rewritten using Eqs. (80a), (81a), (82a), and (84) and assembled for the global degrees-of-freedom. A system of nonlinear FE equations of motion after spatial discretization is obtained:

$$(\delta d(t))^T \left\{ [M] \frac{d^2}{dt^2} (d(t)) + (P(t)) - (F_B(t)) - (F_E(t)) \right\} = 0, \tag{85}$$

where $[M]$ denotes the global mass matrix, $(P(t))$ expresses the internal force, $(F_B(t))$ represents the nodal force due to the distributed loads, $\hat{n}(S,t)$, and $(F_E(t))$ is the nodal force by the boundary forces and couples, defined in Eq. (84).

The FE equations of motion at each time *t* are now written as:

$$[M] \frac{d^2}{dt^2} (d(t)) + (P(t)) - (F(t)) = (0), \tag{86a}$$

where the two force vectors are combined to define the global force vector:

$$(F(t)) \equiv (F_B(t)) + (F_E(t)). \tag{86b}$$

Next, the FE equations of motion are discretized in time.

4.9 The Newmark Time Integration

The FE equations of motion are evaluated at discrete time steps: 0, t_1, t_2, $\cdots$, t_n, t_{n+1}, $\cdots$ with time increment of $\Delta t_n = t_{n+1} - t_n \, (> 0)$. External loads are prescribed at those discrete time steps.

At $t = t_n$, the displacement column matrix, the velocity matrix, and the acceleration matrix are defined as:

$$(d_n) \equiv (d(t_n)), \; (v_n) \equiv \left(\frac{d}{dt} d(t_n) \right), \; (a_n) \equiv \left(\frac{d^2}{dt^2} d(t_n) \right). \tag{87a, b, c}$$

At $t = 0$, for a set of prescribed initial displacements (d_0) and initial velocities (v_0), the acceleration (a_0) is obtained from the equation of motion, Eq. (86a).

At $t = t_n$, the residual force (E_n) is computed using the current set of values of (d_n), (v_n), and (a_n) in Eq. (86a) as:

$$(\mathsf{E}_n) \equiv (F_n) - (P_n) - [M](a_n), \tag{88}$$

where both (F_n) and (P_n) are nonlinear functions of (d_n).

In order to explain an iteration loop, which is performed at the next time step: $t = t_{n+1} = t_n + \Delta t$, let (d_n), (v_n), and (a_n) be a set of values, which satisfy a convergence criterion of the residual force (E_n) after some iterations. A convergence criterion requires that the max-norm of the residual force be $\|(\mathsf{E}_n)\|_\infty < \varepsilon_1$ for a specified tolerance ε_1.

At $t = t_{n+1} = t_n + \Delta t$, let $(d_{n+1}^{(i)})$, $(v_{n+1}^{(i)})$, and $(a_{n+1}^{(i)})$ be nodal displacements, velocities, and accelerations after i^{th} iteration, where the iteration number $i = 0, 1, 2, \cdots$ is shown by a superscript in a pair of parentheses. The FE equations to be solved at $t = t_{n+1}$ in the i$^{\text{th}}$ iteration with $i > 0$ become

$$(\mathsf{E}_{n+1}^{(i)}) = (F_{n+1}^{(i)}) - (P_{n+1}^{(i)}) - [M](a_{n+1}^{(i)}), \tag{89}$$

where the residual $(\mathsf{E}_{n+1}^{(i)})$ satisfies the convergence criterion, $\|(\mathsf{E}_{n+1}^{(i)})\|_\infty < \varepsilon_1$. In Eq. (89), both $(F_{n+1}^{(i)})$ and $(P_{n+1}^{(i)})$ are nonlinear functions of $(d_{n+1}^{(i)})$.

The Newmark time integration method expresses $(d_{n+1}^{(i)})$ and $(v_{n+1}^{(i)})$ using $(a_{n+1}^{(i)})$ as well as the converged values in the previous time step: (d_n), (v_n), and (a_n), utilizing two parameters β and γ (The values of $\beta = 1/4$ and $\gamma = 1/2$ are popularly utilized, see for example [33])

The displacements and velocities are expressed by $(a_{n+1}^{(i)})$ as:

$$\left(d_{n+1}^{(i)}\right)=\left(d_{n+1}^{(0)}\right)+\beta\,\Delta t^2\left(a_{n+1}^{(i)}\right), \tag{90a}$$

$$\left(v_{n+1}^{(i)}\right)=\left(v_{n+1}^{(0)}\right)+\gamma\,\Delta t\left(a_{n+1}^{(i)}\right), \tag{90b}$$

where $(d_{n+1}^{(0)})$ and $(v_{n+1}^{(0)})$ are referred to as the *predictors* and computed by using the known values at t_n as:

$$\left(d_{n+1}^{(0)}\right)=\left(d_n\right)+\Delta t\left(v_n\right)+\frac{\Delta t^2}{2}(1-2\beta)\left(a_n\right). \tag{90c}$$

where the predictor (is computed by using the known values at t_n :

$$\left(v_{n+1}^{(0)}\right)=\left(v_n\right)+(1-\gamma)\Delta t\left(a_n\right). \tag{90d}$$

From Eq. (90a), $(a_{n+1}^{(i)})$ is expressed by $(d_{n+1}^{(i)})$ as:

$$\left(a_{n+1}^{(i)}\right)=\frac{1}{\beta\,\Delta t^2}\left\{\left(d_{n+1}^{(i)}\right)-\left(d_{n+1}^{(0)}\right)\right\}. \tag{91}$$

Using the Newmark method, the residual force in Eq. (89) is rewritten using Eq. (91) as:

$$\left(\mathsf{E}_{n+1}^{(i)}\right)=\left(F_{n+1}^{(i)}\right)-\left(P_{n+1}^{(i)}\right)-\frac{1}{\beta\,\Delta t^2}[M]\left\{\left(d_{n+1}^{(i)}\right)-\left(d_{n+1}^{(0)}\right)\right\}. \tag{92}$$

The convergence at $t=t_{n+1}$ is achieved if the following two inequalities are satisfied for small tolerances of ε_1 and ε_2 :

$$\left\|\left(\mathsf{E}_{n+1}^{(i)}\right)\right\|_\infty<\varepsilon_1 \text{ and } \left\|\left(d_{n+1}^{(i)}\right)-\left(d_{n+1}^{(i-1)}\right)\right\|_\infty<\varepsilon_2\,. \tag{93}$$

(It is aimed at achieving the convergence in less than five iterations by using a small Δt .)

Equation (92) only furnishes a means to compute the magnitude of the residual force, $\left\|\left(\mathsf{E}_{n+1}^{(i)}\right)\right\|_{\infty}$. To reduce $\left\|\left(\mathsf{E}_{n+1}^{(i)}\right)\right\|_{\infty}$ in a systematic manner, the Newton-Raphson method is employed. This iterative scheme for nonlinear FEA is expertly presented by Belytschko, Liu, and Moran [33].

4.9.1 Iterative Solution Scheme Using the Newton-Raphson Method

Let the elemental nodal displacements be expressed as:

$$\left(\hat{d}_{n+1}^{(e)\,(i+1)}\right)=\left(\hat{d}_{n+1}^{(e)\,(i)}\right)+\left(\Delta\hat{d}_{n+1}^{(e)\,(i+1)}\right). \tag{94a}$$

The corresponding global nodal-displacements at the $(i+1)^{st}$ iteration are

$$\left(d_{n+1}^{(i+1)}\right)=\left(d_{n+1}^{(i)}\right)+\left(\Delta d_{n+1}^{(i+1)}\right). \tag{94b}$$

Similarly, the beam stresses in the $(i+1)^{st}$ iteration are expressed as

$$\begin{pmatrix} N_1^{(e)\,(i+1)} \\ N_2^{(e)\,(i+1)} \\ M_3^{(e)\,(i+1)} \end{pmatrix}(S^{(e)},t_{n+1})=\begin{pmatrix} N_1^{(e)\,(i)} \\ N_2^{(e)\,(i)} \\ M_3^{(e)\,(i)} \end{pmatrix}(S^{(e)},t_{n+1})+\begin{pmatrix} \Delta N_1^{(e)\,(i+1)} \\ \Delta N_2^{(e)\,(i+1)} \\ \Delta M_3^{(e)\,(i+1)} \end{pmatrix}(S^{(e)},t_{n+1}). \tag{95}$$

The beam strains in the $(i+1)^{st}$ iteration are

$$\begin{pmatrix} \hat{\gamma}_1^{(e)\,(i+1)} \\ \hat{\gamma}_2^{(e)\,(i+1)} \\ \kappa_3^{(e)\,(i+1)} \end{pmatrix}(S^{(e)},t_{n+1})=\begin{pmatrix} \hat{\gamma}_1^{(e)\,(i)} \\ \hat{\gamma}_2^{(e)\,(i)} \\ \kappa_3^{(e)\,(i)} \end{pmatrix}(S^{(e)},t_{n+1})+\begin{pmatrix} \Delta\hat{\gamma}_1^{(e)\,(i+1)} \\ \Delta\hat{\gamma}_2^{(e)\,(i+1)} \\ \Delta\kappa_3^{(e)\,(i+1)} \end{pmatrix}(S^{(e)},t_{n+1}). \tag{96a}$$

The incremental strains on the right-hand-side of Eq. (96b) are expressed by the incremental displacements $\left(\Delta\hat{d}_{n+1}^{(e)\,(i+1)}\right)$ by writing the beam strains in Eq. (76a) for the i^{th} iteration using $\left(\hat{d}_{n+1}^{(e)\,(i)}\right)$ and the $(i+1)^{st}$ iteration using Eq. (96a). A straight forward calculation using $\psi^{(i+1)}=\psi^{(i)}+\Delta\psi^{(i+1)}$ for $\left|\Delta\psi^{(i+1)}\right|<<1$, the incremental relation is expressed

using the same $[B_{T\,n+1}^{(e)\,(i)}]$-matrix, which relates the virtual strain and the virtual displacement relation in Eq. (78b):

$$\begin{pmatrix} \Delta\hat{\gamma}_1^{(e)\,(i+1)} \\ \Delta\hat{\gamma}_2^{(e)\,(i+1)} \\ \Delta\kappa_3^{(e)\,(i+1)} \end{pmatrix}(S^{(e)}, t_{n+1}) = \underset{3\times 11}{\left[\ B_{T\,n+1}^{(e)\,(i)}(S^{(e)}, L_0^{(e)})\ \right]}\left(\Delta\hat{d}_{n+1}^{(e)\,(i+1)}\right). \tag{96b}$$

The rate-constitutive relation in Eq. (55), is implemented by specifying $\Delta\kappa_3^{\#}(S^{(e)}, t_{n+1}) \equiv \kappa_3^{\#}(S^{(e)}, t_{n+1}) - \kappa_3^{\#}(S^{(e)}, t_n)$ at the 0th iteration of $t = t_{n+1}$ to compute $\left(\mathsf{E}_{n+1}^{(0)}\right)$. As a result, the rate form translates to the incremental beam stress and incremental beam strain relation for the iteration i>0 :

$$\begin{pmatrix} \Delta N_1^{(e)\,(i+1)} \\ \Delta N_2^{(e)\,(i+1)} \\ \Delta M_3^{(e)\,(i+1)} \end{pmatrix}(S^{(e)}, t_{n+1}) = \begin{bmatrix} EA & 0 & 0 \\ 0 & GA_s & 0 \\ 0 & 0 & EI_2 \end{bmatrix}^{(e)} \begin{pmatrix} \Delta\hat{\gamma}_1^{(e)\,(i+1)} \\ \Delta\hat{\gamma}_2^{(e)\,(i+1)} \\ \Delta\kappa_3^{(e)\,(i+1)} \end{pmatrix}(S^{(e)}, t_{n+1}) \text{ for } i > 0. \tag{97}$$

The principle of virtual work, Eq. (79), is written for the $(i+1)^{st}$ iteration observing that the variations are only allowed for the incremental displacements:

$$\sum_{e=1}^{N_{el}} \left(\delta\,\Delta\hat{d}_{n+1}^{(e)(i+1)}\right)^T \int_0^{L_0^{(e)}} \left[\ B_{T\,n+1}^{(e)\,(i+1)}\right]^T \begin{pmatrix} N_1^{(e)\,(i)}(S^{(e)}, t_{n+1}) + \Delta N_1^{(e)\,(i+1)}(S^{(e)}, t_{n+1}) \\ N_2^{(e)\,(i)}(S^{(e)}, t_{n+1}) + \Delta N_2^{(e)\,(i+1)}(S^{(e)}, t_{n+1}) \\ M_3^{(e)\,(i)}(S^{(e)}, t_{n+1}) + \Delta M_3^{(e)\,(i+1)}(S^{(e)}, t_{n+1}) \end{pmatrix} dS^{(e)}$$

$$= \sum_{e=1}^{N_{el}} \left(\delta\,\Delta\hat{d}_{n+1}^{(e)\,(i+1)}\right)^T \int_0^{L_0^{(e)}} \left[\overline{\overline{N}}(S^{(e)}, L_0^{(e)})\right]^T \begin{pmatrix} \hat{n}^I(S^{(e)}, t_{n+1}) \\ \hat{m}_3(S^{(e)}, t_{n+1}) \end{pmatrix} dS^{(e)}$$

$$- \left(\delta\Delta d_{n+1}^{(i+1)}\right)^T \frac{1}{\beta\,\Delta t^2}[M]\left\{\left(\Delta d_{n+1}^{(i+1)}\right) + \left(d_{n+1}^{(i)}\right) - \left(d_{n+1}^{(0)}\right)\right\} + \left(\delta d_{n+1}^{(i+1)}\right)^T \left(F_E^{(i+1)}(t_{n+1})\right). \tag{98}$$

For the time integration, the Newmark method is employed, and at each time step, the Newton method is utilized to iterate and reduce the residual forces.

4.10 Application: Nonlinear Simulation of an Inchworm

To solve the nonlinear equations of motion, Eqs. (41) and (43), active C^1-beam elements were developed and implemented in a nonlinear finite element (FE) code utilizing the beam principle of virtual work. (The FE implementation of active C^1-beam elements will be deferred to a subsequent publication.)

In this section, a linear locomotion of an inchworm-inspired robot, built by Wang et al. [34], is simulated. An inchworm has three pairs of true (front) legs in the thorax and two pairs of (hind) prolegs. The locomotion of the inchworm is actuated by the contraction of longitudinal muscle fibers in the soft abdomen. Wang et al. mimicked the inchworm actuation by embedding shape-memory-alloy (SMA) wires axially in a soft polydimethylsiloxane (PDMS) layer [34].

An inchworm moves by periodically repeating the following two motions: (i) pulling its hind prolegs forward while anchoring the front legs, and (ii) switching the holding legs to the hind prolegs and advancing its front legs. Wang et al. implemented this switching of legs by using transverse SMAs imbedded only in the front and hind leg sections with polyimide (PI) films bonded at both sides. The transverse SMA wires warp the section in either convex shape for anchoring and concave shape for sliding. The anchoring is achieved in the convex warping of the leg sections by the contacting PI films at both edges. In the concave warping, a smooth PDMS layer enables sliding. As a result, their robot geometry is not a slender beam, but a thin plate.

To simulate a linear locomotion of a plate-shaped inchworm robot, built by Wang et al. [34], the robot is modeled as a simply supported beam of span L. For slow SMA wire actuations, the quasi-static boundary-value problem is defined by the equilibrium equations

obtained from Eqs. (41) and (43) by neglecting the inertia terms. The beam subjected to the distributed loads due to the gravitational field, $-m_A g \mathbf{e}_1^I$ and zero distributed couple:

$$\begin{pmatrix} \hat{n}_1^I \\ \hat{n}_2^I \end{pmatrix}(S,t) = \begin{pmatrix} 0 \\ -m_A g \end{pmatrix}, \qquad \hat{m}_3(S,t) = 0 . \tag{99a, b}$$

The head and tail nodes of the beam are subjected to the *simply-supported sliding boundary conditions*. The kinematic boundary conditions are:

$$y_C(t) = 0 \ \text{ at } S = 0 \ (\text{tail node}) \ \text{ and } \ S = L \ (\text{head node}), \tag{100a}$$

while the kinetic boundary conditions are

$$N_3(t) = M_2(t) = 0 \ \text{ at } S = 0 \ (\text{tail node}) \ \text{ and } \ S = L \ (\text{head node}). \tag{100b}$$

The quasi-static nonlinear FE analyses was performed using a book-keeping time with the locomotion period of 2π . A periodic actuation by the longitudinal SMA wires of the beam for linear locomotion is described by the sinusoidal actuation function:

$$\kappa^{\#}(t) = -\kappa_0^{\#}\{1+\cos(t-\pi)\}/2, \tag{101}$$

where $\kappa_0^{\#}$ the maximum absolute amplitude of the actuation curvature.

The switching of the anchored-legs is implemented by defining: (i) loading phase $\dot{\kappa}^{\#}(t) < 0$, (ii) neutral phase $\dot{\kappa}^{\#}(t) = 0$ and (iii) unloading phase $\dot{\kappa}^{\#}(t) > 0$. In loading, the x_C -velocity of the head node is fixed, while in unloading the x_C -velocity of the tail node is fixed.

$$\dot{x}_C(t) = 0 \ \text{ at } S = L \ (\text{head node}) \ \text{ if } \dot{\kappa}^{\#}(t) < 0 \ (\text{loading phase}), \tag{102a}$$

$$\dot{x}_C(t) = 0 \ \text{ at } S = 0 \ (\text{tail node}) \ \text{ if } \dot{\kappa}^{\#}(t) > 0 \ (\text{unloading phase}). \tag{102b}$$

The neutral phase rarely happens numerically. Therefore, it was included in the loading phase by modifying the loading condition as $\dot{\kappa}^{\#}(t) \le 0$. Figure 7 visually shows the switching that occurs to move the inchworm forward.

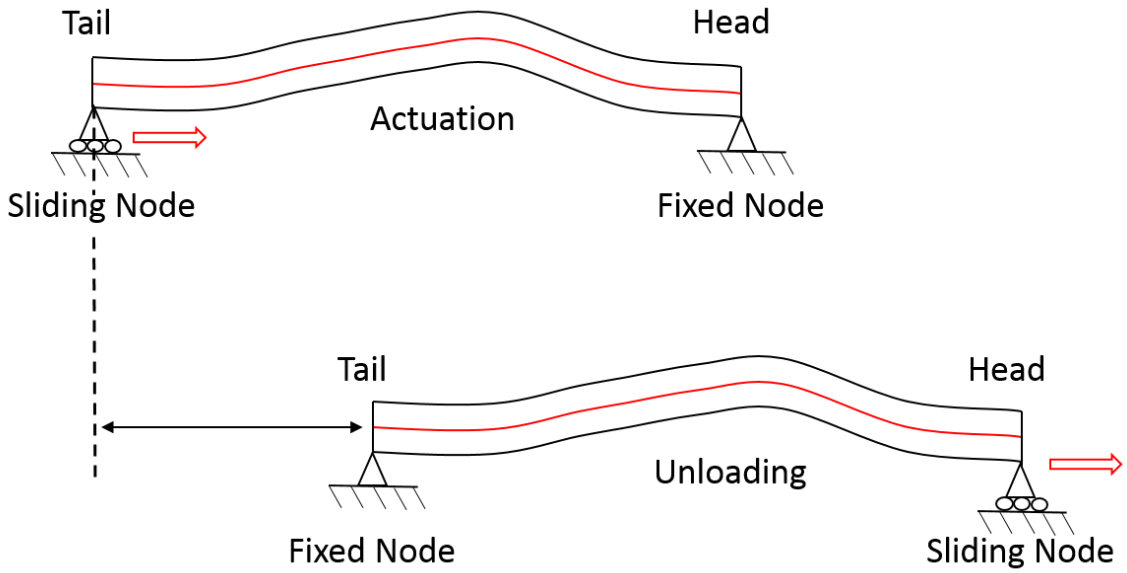

Figure 4-7: Switching of the fixed and sliding nodes during actuation and unloading phases

Figure 8 shows the curled configurations of the beam by fixing the head node: $x_C(t) = L$ at $S = L$, as the absolute values of the uniform activation curvatures increase. By simply fixing the head node, the activation function, Eq. (101), enables the curling and uncurling of the beam periodically without moving forward, as illustrated in Fig. 8.

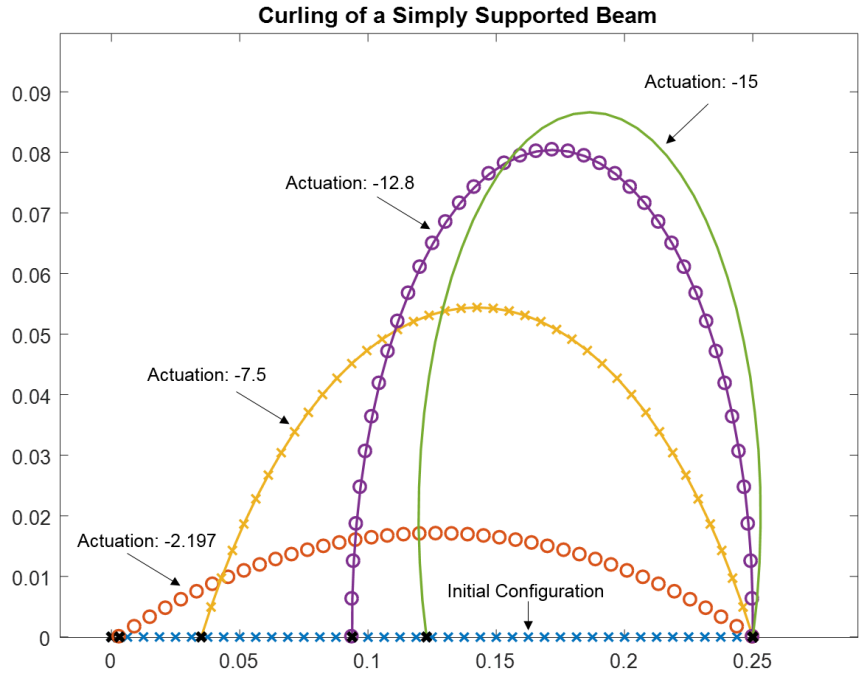

Figure 4-8: Constant actuation of a simply supported beam, demonstrating the curling motion of the inchworm robot

In the above computation, a uniform beam of a rectangular cross section with width b=0.02m and height h=0.01m is considered utilizing the mechanical properties of E=2.4GPa, G=0.96GPa, m_A=0.278 kg/m, J_{3C}=0.232x10^{-5} kgm^2. As a shear correction factor, 5/6 was used A_s=5bh/6. To achieve convergence at each load increment in less than five iterations, the increment of the actuation curvature was limited to be $\left|\Delta\kappa^{\#}\right| = 2h/L^2$, which induce h/4 of the mid-span according to the analytical solution of the active linear Timoshenko beam.

To simulate the robot built by Wang et al. and to demonstrate the switching of the anchored legs to achieve forward motion, a uniform actuation curvature field was adopted as shown in Fig. 9(a-g) [34]. In the figure, two additional elements, shown in black, were added to simulate the prolegs and true legs of the inchworm. In addition to the continuous

model, a 2-link discrete mechanical model is also shown in green. Note that as the number of links increases, the discrete solution looks similar to that obtained by the continuous model.

However, to achieve a more realistic locomotion of an inchworm, it is necessary to employ an activation curvature field that changes with the arc-parameter S. Therefore, the presented active beam model furnishes a useful tool for finding the actuation fields to mimic the motion of slender creatures by embedding necessary actuation devices or mechanisms.

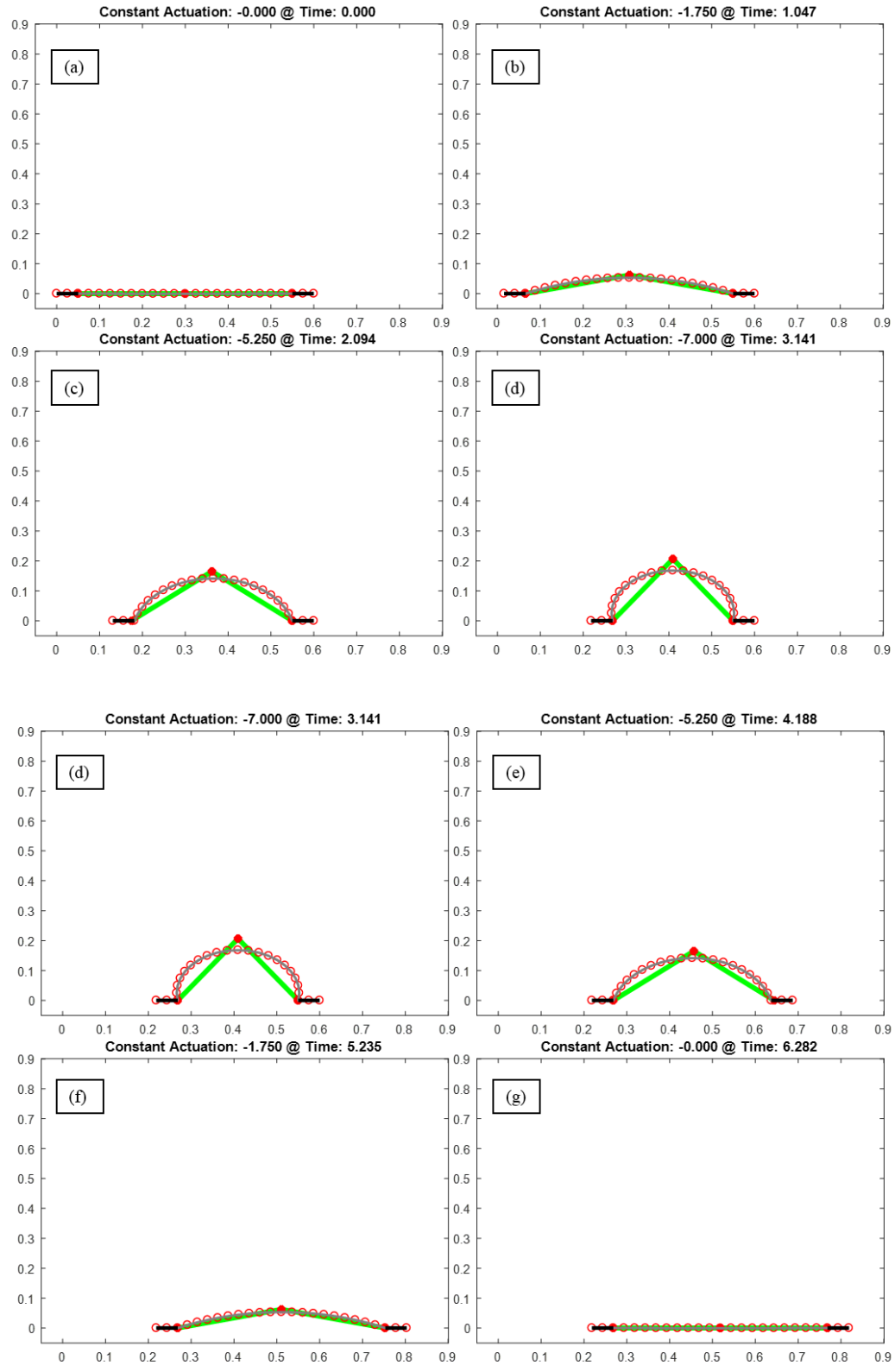

Figure 4-9: (a-d) Actuation and (d-g) unloading of a simulated inchworm

4.10.1 Alternative Actuation of Inchworm

To more closely resemble the "looping" inchworm curvature field, a different actuation expression is needed. In the previous section, every point along the beam was actuated by the same amount at every time step, producing a round symmetrical curve. In reality, the inchworm locomotion rarely resembles that of Fig 9. Instead, the curvature field is asymmetrical, indicating an actuation dependence not only on time t, but on the arc parameter S as well. Therefore, the actuation expression in Eq. (101) is rewritten as Eq. (103a) below:

$$\kappa^{\#}(S,t) = -\frac{1}{2}\kappa_0^{\#}(S)\{1+\cos(t-\pi)\} \tag{103a}$$

where $\kappa_0^{\#}(S)$ is now a function of the arc parameter S. Noting that the actuation needs to be increased as we go from the tail node to the head node, $\kappa_0^{\#}(S)$ will be expressed as a linear function, as shown in Eq. (103b):

$$\kappa_0^{\#}(S) = \kappa_0^{\#}\left\{c_1 + c_2 * \left(\frac{S}{L}\right)\right\} \tag{103b}$$

where b and m are constants, $\kappa_0^{\#}$ is the maximum absolute amplitude of the actuation curvature, and L is the length of the beam. For this simulation, the mechanical and geometrical properties used in the prior section will once again be used, along with the following values for the constants: $c_1 = 0.2$, $c_2 = 0.8$, and maximum actuation $\kappa_0^{\#} = 13$. Figure 10 demonstrates the resulting locomotion when using the spatially linearly varying actuation expressed in Eqs. (103a-b). As can be seen, the curvature now more closely resembles the asymmetrical curve seen in inchworms. Other forms of actuation can be prescribed, including an alternative linear form of actuation where the slope, and not the y-intercept, changes as the maximum actuation is varied. The model can thus provide the

user with valuable information. For a specified material and geometry, the user can now obtain the maximum actuation needed to achieve certain shapes, as well as the need for spatial variance in actuation.

The model can thus provide the user with valuable information. For a specified material and geometry, the user can now obtain the maximum actuation needed to achieve certain shapes. Furthermore, the model can serve as an indicator of the spatial variance in actuation needed which can lead to design changes in the placement of the pneumatic air chambers.

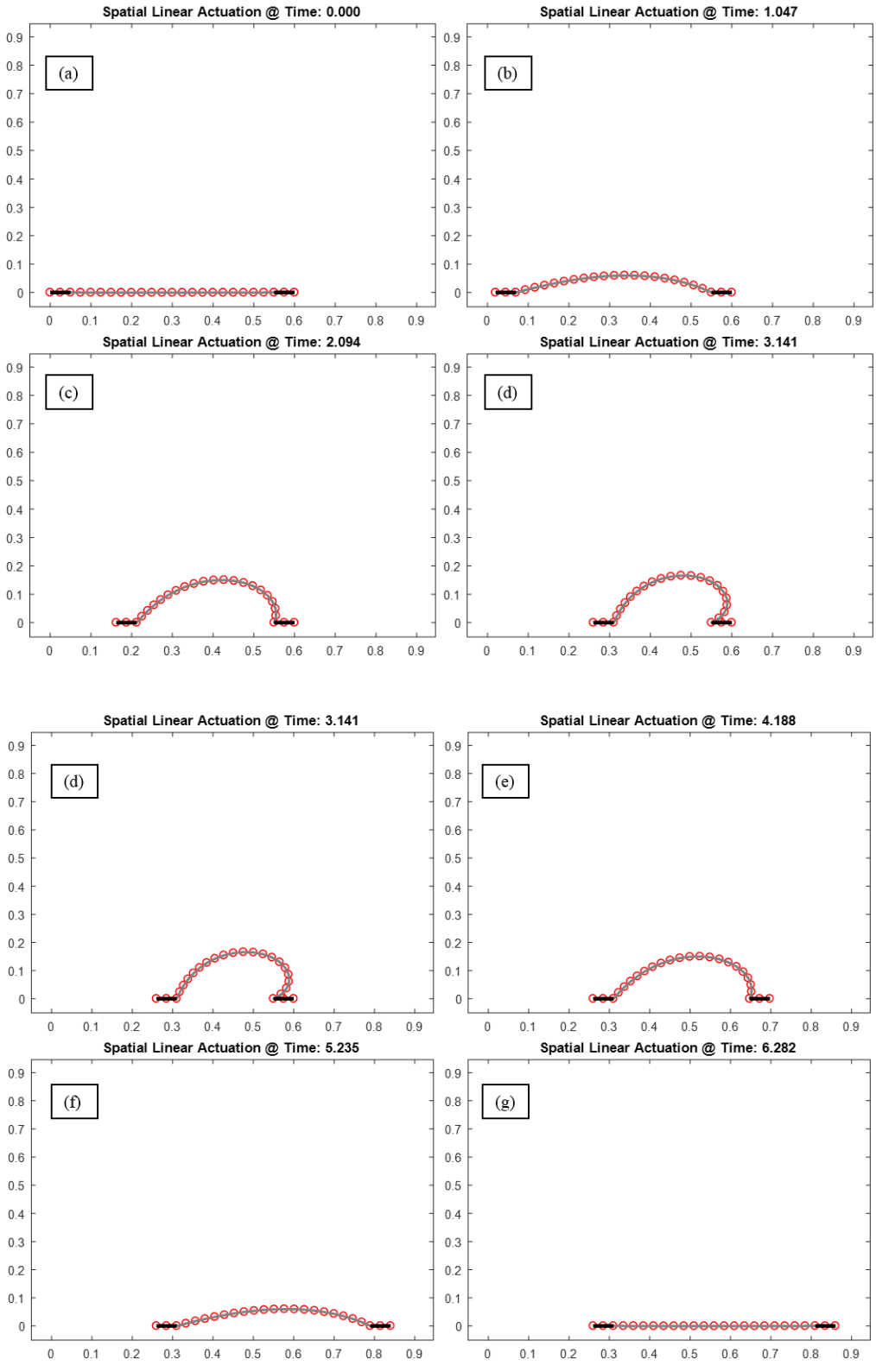

Figure 4-10: (a-d) Actuation and (d-g) unloading of a simulated inchworm with spatial actuation

4.11 Concluding Remarks

Mechanical models applicable to soft or flexible robots have been successfully developed. The first is a discrete model that consists of (n) number of jointed cylindrical segments with torsional springs while the second is a continuous beam model with internal actuation. In addition to the derivation of the models, the incorporation of the interaction forces from various environmental settings has been discussed. Lastly, to demonstrate the continuous beam model, two examples have been solved. The first is a simple solution to an actuated linear cantilever beam under a uniformly distributed load. The second is a simulation of an inchworm obtained by using the nonlinear continuous beam model, where two methods of actuation were discussed to closely mimic the inchworm's locomotion.

Chapter 4, in part, is published as "Development of Active Mechanical Models for Flexible Robots to Duplicate the Motion of Inch Worms and Snakes." Proceedings of the ASME 2016 International Mechanical Engineering Congress & Exposition. Paper: IMECE2016-65550. ASME, New York. This work was coauthored by H. Murakami, and T. Ono. The dissertation author is the first author of this work.

4.12 Appendix

The Element Mass Matrix of the C^1-Beam Element defined in Eq. (35):

$$\left[\underset{11\times 11}{\hat{M}^{(e)}}\right]=\begin{bmatrix} \underset{4\times 4}{\hat{M}_{11}^{(e)}} & \underset{4\times 4}{0} & \underset{4\times 3}{0} \\ \underset{4\times 4}{0} & \underset{4\times 4}{\hat{M}_{22}^{(e)}} & \underset{4\times 3}{0} \\ \underset{3\times 4}{0} & \underset{3\times 4}{0} & \underset{3\times 3}{\hat{M}_{33}^{(e)}} \end{bmatrix}, \tag{104}$$

where

$$\left[M_{11}^{(e)}{}_{4\times4} \right] = \left[M_{22}^{(e)}{}_{4\times4} \right] = \mathsf{m}_{A(0)} L_0^{(e)} \begin{bmatrix} \frac{13}{35} & \frac{11L_0^{(e)}}{210} & \frac{9}{70} & -\frac{13L_0^{(e)}}{420} \\ \frac{11L_0^{(e)}}{210} & \frac{(L_0^{(e)})^2}{105} & \frac{13L_0^{(e)}}{420} & -\frac{(L_0^{(e)})^2}{140} \\ \frac{9}{70} & \frac{13L_0^{(e)}}{420} & \frac{13}{35} & -\frac{11L_0^{(e)}}{210} \\ -\frac{13L_0^{(e)}}{420} & -\frac{(L_0^{(e)})^2}{140} & -\frac{11L_0^{(e)}}{210} & \frac{(L_0^{(e)})^2}{105} \end{bmatrix}, \tag{105}$$

$$\left[\hat{M}_{33}^{(e)} \right] = J_{3C(0)}^{(e)} L_0^{(e)} \begin{bmatrix} \frac{2}{15} & -\frac{1}{30} & \frac{1}{15} \\ -\frac{1}{30} & \frac{2}{15} & \frac{1}{15} \\ \frac{1}{15} & \frac{1}{15} & \frac{8}{15} \end{bmatrix}. \tag{106}$$

4.13 References

[1] Seok, S., Onal, C.D., Cho, K.J., Wood, R.J., Rus, D. and Kim, S., 2013. Meshworm: "A peristaltic soft robot with antagonistic nickel titanium coil actuators". *Mechatronics, IEEE/ASME Transactions on*, *18*(5), pp.1485-1497.

[2] Tolley, M.T., Shepherd, R.F., Mosadegh, B., Galloway, K.C., Wehner, M., Karpelson, M., Wood, R.J. and Whitesides, G.M., 2014. "A resilient, untethered soft robot". *Soft Robotics*, *1*(3), pp.213-223.

[3] Calisti, M., Giorelli, M., Levy, G., Mazzolai, B., Hochner, B., Laschi, C. and Dario, P., 2011. "An octopus-bioinspired solution to movement and manipulation for soft robots". *Bioinspiration & biomimetics*, *6*(3), p.036002.

[4] Hirose, S., 1993, Biologically Inspired Robots: Snake-Like Locomotors and Manipulators, Oxford University Press, New York.

[5] Saito, M., Fukaya, M., and Iwasaki, T., 2002, "Serpentine Locomotion with Robotic Snakes, IEEE Control Systems Magazine, February, 2002, pp. 64-81.

[6] Taylor, G. I., 1952, "Analysis of the Swimming of Long and Narrow Animals," Proceedings of the Royal Society of London, Ser. A, Mathematical and Physical Sciences, Vol. 214, No. 1117, pp. 158-183.

[7] Frankel, T., 2012, *The Geometry of Physics, an Introduction*, third edition, Cambridge University Press, New York.

[8] Murakami, H., 2015, "A Moving Frame Method for Multi-Body Dynamics Using SE(3)," *Proceedings of the ASME 2015 International Mechanical Engineering Congress & Exposition*, Paper IMECE2015-51192, ASME, New York.

[9] Murakami, H., 2016, "Development of an Active Curved Beam Model Using a Moving Frame Method," *Proceedings of the ASME 2016 International Mechanical Engineering Congress & Exposition*, Paper IMECE2016-65550, ASME, New York..

[10] Marsden, J. E., and Hughes, T. J. R., 1983, *Mathematical Foundations of Elasticity*, Prentice-Hall, Englewood Cliffs, New Jersey.

[11] Reissner, E., 1972, "On One-Dimensional Finite-Strain Beam Theory: The Plane Problem," Journal of Applied Mathematics and Physics (ZAMP), Vol. 23, ppl 795-804.

[12] Simo, J. C., and Vu-Quoc, L., 1986, "On the Dynamics of Flexible Beams Under Large Overall Motions-The Plane Case: Part I," ASME *Journal of Applied Mechanics*, Vol. 53, pp. 849-854.

[13] Simo, J. C., and Vu-Quoc, L., 1986, "On the Dynamics of Flexible Beams Under Large Overall Motions-The Plane Case: Part II," ASME *Journal of Applied Mechanics*, Vol. 53, pp. 855-863.

[14] Lighthill, M. J., 1960, "Note on the Swimming of Slender Fish," *Journal of Fluid Mechanics*, Vol. 9, pp. 305-317.

[15] Onal, C.D. and Rus, D., 2013. "Autonomous Undulatory Serpentine Locomotion Utilizing Body Dynamics of a Fluidic Soft Robot". *Bioinspiration & biomimetics*,*8*(2), p.026003.

[16] Bekker, M. G., 1956, *Theory of Land Locomotion*, University of Michigan Press, Ann Arbor,

[17] Wong, J. Y., 2001, *Theory of Ground Vehicles*, Third edition, John Wiley & Sons, New York.

[18] Watanabe, K., Murakami, H., Kitano, M., and Katahira, T., 1993, "Experimental Characterization of Dynamic Soil-Track Interaction on Dry Sand," *Journal of Terramechanics*, Vol. 30 (2), pp. 111-131.

[19] Janosi, Z., and Hanamoto, B., 1961, "The analytical Determination of Drawbar Pull as a Function of Slip for Tracked Vehicles in Deformable Soils," *Proceedings of the First International Conference on Mechanics of Soil-Vehicle Systems*, Torino, Italy, p. 707.

[20] Hetenyi, M., 1946, *Beams on Elastic Foundation: Theory and Applications in the Field of Civil and Mechanical Engineering*, University of Michigan Press, Ann Arbor, MI.

[21] Murakami, H., and Impelluso, T. J., 1998, "Large-Deformation Analyses of Spatial Beams by Using Frenet's Moving Frame," *Proceedings of the 12th Engineering Mechanics Conference*, H. Murakami and J. E. Luco eds., La Jolla, California, May 17-20, ASME, Reston, VA.

[22] Reddy, J. N., 1993, *An Introduction to the Finite Element Method*, 2nd edition, McGraw-Hill, New York.

[23] Murakami, H., Reissner, E., and Yamakawa, J., 1996, "Anisotropic Beam Theories with Shear Deformation," *Journal of Applied Mechanics*, Vol. 63 (3), pp. 660-668.

[24] Wang, W., Lee, J.Y., Rodrigue, H., Song, S.H., Chu, W.S. and Ahn, S.H., 2014. "Locomotion of inchworm-inspired robot made of smart soft composite (SSC)". *Bioinspiration & biomimetics, 9(4), p.046006.*

[25] Murakami, Hidenori, Oscar Rios, and Thomas Joseph Impelluso. "A Theoretical and Numerical Study of the Dzhanibekov and Tennis Racket Phenomena." *Journal of Applied Mechanics* 83.11 (2016): 111006.

[26] Simo, J. C., and Vu-Quoc, L., 1986, "On the Dynamics of Flexible Beams Under Large Overall Motions---The Plane Case: Part I," ASME Journal of Applied Mechanics, Vol. 53 (December), pp. 849-854.

[27] Simo, J. C., and Vu-Quoc, L., 1986, "On the Dynamics of Flexible Beams Under Large Overall Motions---The Plane Case: Part II," ASME Journal of Applied Mechanics, Vol. 53 (December), pp. 855-863.

[28] Rios O., Ono T. & Murakami H. 2016. "Development of Active Mechanical Models for Flexible Robots to Duplicate the Motion of Inch Worms and Snakes." Proceedings of the ASME 2016 International Mechanical Engineering Congress & Exposition. Paper: IMECE2016-65550. ASME, New York.

[29]Murakami, H., 2017, "Development of an Active Beam Model---Part II: Kinetics and Internal Activation," *ASME Journal of Applied Mechanics*, Vol. 84 (June), paper 061003 (17 pages);

[30] Reddy, J. N., 1993, *An Introduction to the Finite Element Method*, 2nd edition, McGraw-Hill, New York.

[31] Hughes, T. J. R., 1987, *The Finite Element Method, Linear Static and Dynamics Finite Element Analysis*, Prentice Hall, Englewood Cliffs. NJ.

[32] Bathe, K.J., 2008. *Finite element method*. John Wiley & Sons, Inc.

[33] Belytschko, T., Liu, W. K., and Moran, B., 2000, Nonlinear Finite Elements for Continua and Structures, John Wiley & Sons, New York.***

[34] Wang, W., Lee, J.Y., Rodrigue, H., Song, S.H., Chu, W.S. and Ahn, S.H., 2014. "Locomotion of inchworm-inspired robot made of smart soft composite (SSC)". *Bioinspiration & biomimetics*, *9(4), p.046006.*

CHAPTER 5: CONCLUSIONS

The moving frame method had been applied and used to analyze a single rigid body, a multi rigid body system, and flexible bodies. As was shown, the moving frame method provides a compact and systematic method for deriving the equations of motion

For both the Dzhanibekov and tennis racket experiments experiencing torque free rotation, when the initial angular velocity is applied to the axis of maximum or minimum moment of inertia, the axis of rotation remains the same. This is easily interpreted as the result of the conservation of angular momentum. However, when the initial rotation is applied to the principal axis of the intermediate moment of inertia value, the body exhibits rotations about the other axes. This unstable rotation could be easily misinterpreted as evidence for violating of the conservation the angular momentum in torque free motion.

In Chapter 2, we theoretically and numerically demonstrated (the latter with 3D animations), that the rotations are periodic with the principal axis of the intermediate moment of inertia. Our computational approach employs numerical integration of Euler's torque-free equation and a *recovery equation for rotation matrix* to easily present 3D animations.

In Chapter 3, gyroscopic multibody systems were analyzed, including a gyroscopic ocean wave energy converter and a marine vessel installed with dual gyroscopic roll stabilizers. The mathematical model of the gyroscopic ocean wave energy converter has been derived using the moving frame method, allowing for a systematic approach in deriving the kinematics of the system. The equation of motion derived was then used to obtain an expression for the average power output. To maximize the power output of the

GOWEC, it was found that the gimbal motion, $\varphi^{(2)}(t)$, has to be matched with that of the incoming wave. The maximum power output was shown to greatly depend on the frequency of oscillation and amplitude of the incoming wave. It was also shown that the power can greatly decrease with minute changes in wave direction or frequency. Lastly, an estimate of the electrical power output using off-the-shelf gyroscopic stabilizers produced by Seakeeper was reported.

As a natural extension of the GOWEC, the effect of the gyroscopic roll stabilizer and its parameters on the ship has been analyzed. Through the use of the moving frame method, a general mathematical model of a marine vessel installed with a dual gyroscope configuration has been obtained. In addition, both continuous and sinusoidal methods of excitation have been discussed and shown to produce similar output results on the ship. Furthermore, the systems parameters have been characterized and their effect on the output angular velocity and displacement have been analyzed.

In Chapter 4, mechanical models applicable to soft or flexible robots were successfully developed. The first is a discrete model that consists of (n) number of jointed cylindrical segments with torsional springs while the second is a continuous beam model with internal actuation. In addition to the derivation of the models, the incorporation of the interaction forces from various environmental settings has been discussed. Lastly, to demonstrate the continuous beam model, two examples have been solved. The first is a simple solution to an actuated linear cantilever beam under a uniformly distributed load. The second is a simulation of an inchworm obtained by using the nonlinear continuous beam model, where two methods of actuation were discussed to closely mimic the inchworm's locomotion. To obtain inchworm simulation, a nonlinear finite element code

was developed to solve the nonlinear finite element equations of motion that were derived using active C^1 beam elements.